

AIX-MARSEILLE UNIVERSITY
DOCTORAL SCHOOL: Physics and Material Science
PARTENAIRES DE RECHERCHE
Laboratoire MADIREL

Submitted with the view of obtaining the degree of doctor

Discipline: Material Science
Specialty: Characterisation of porous materials

Paul A. Iacomi

Titre de la thèse: sous-titre de la thèse

Defended on JJ/MM/AAAA in front of the following jury:

Prénom NOM	Affiliation	Rapporteur
Prénom NOM	Affiliation	Rapporteur
Prénom NOM	Affiliation	Examinateur
Prénom NOM	Affiliation	Examinateur
Prénom NOM	Affiliation	Examinateur
Prénom NOM	Affiliation	Directeur de thèse

National thesis number: 2017AIXM0001/001ED62



This work falls under the conditions of the Creative Commons Attribution License -
No commercial use - No modification 4.0 International.

Abstract

Abstract is here.

Acknowledgements

Acknowledgements go here

Contents

Abstract	iii
Acknowledgements	iv
1. Building a framework for adsorption data processing	1
1.1. Introduction	1
1.2. pyGAPS overview	2
1.2.1. Intended use cases	2
1.2.2. Core structure	2
1.2.3. Creation of an Isotherm	3
1.2.4. Workflow	4
1.2.5. Units	5
1.3. Isotherm characterisation and fitting	5
1.3.1. Mathematical descriptions of isotherms	5
1.3.2. Specific surface area and pore volume calculations	13
1.3.3. Assessing porosity	20
1.3.4. Predicting multicomponent adsorption	27
1.4. Case studies	29
1.5. Conclusion	29
Bibliography	30
2. Extending bulk analysis of porous compounds through calorimetry	34
2.1. Introduction	34
2.2. Literature	34
2.3. Method	35
2.4. Results and discussion	35
2.4.1. Routine characterization of a MOF sample	35
2.4.2. Analysis of a carbon sample for gas separation applications	37
2.5. Conclusion	37
Bibliography	38
3. Exploring the impact of synthesis and defects on adsorption measurements	39
3.1. Introduction	39
3.2. The defective nature of MOFs	41
3.2.1. Types of crystal defects and their analogues in MOFs	41
3.2.2. Consequences of defects	43

Contents

3.2.3. Defect engineering of MOFs	44
3.2.4. The propensity of UiO-66(Zr) for defect generation	44
3.3. Materials and methods	46
3.3.1. Materials	46
3.3.2. Methods for quantifying defects	48
3.4. Results and discussion	49
3.4.1. Crystallinity of leached samples	49
3.4.2. NMR	49
3.4.3. Thermogravimetry results	49
3.4.4. Nitrogen sorption at 77K	52
3.4.5. Characterisation of trends	52
3.4.6. Carbon dioxide isotherms	58
3.5. Conclusion	59
Bibliography	60
4. Exploring the impact of material form on adsorption measurements	68
4.1. Introduction	68
4.2. Shaping in context	69
4.3. Materials, shaping and characterisation methods	71
4.3.1. Materials	71
4.3.2. Shaping Procedure	72
4.3.3. Characterisation of powders and pellets	72
4.3.4. Sample activation for adsorption	73
4.4. Results and discussion	73
4.4.1. Thermal stability	73
4.4.2. Adsorption isotherms at 77K and room temperature	73
4.4.3. Room temperature gas adsorption and microcalorimetry	76
4.4.4. Vapour adsorption	82
4.5. Conclusion	89
Bibliography	90
5. Exploring novel behaviours	94
5.1. Introduction	94
5.2. Literature	94
5.3. Method	94
5.4. Results and discussion	94
5.5. Conclusion	94
Bibliography	95
A. Common characterisation techniques	96
A.1. Thermogravimetry	96
A.2. Bulk density determination	96
A.3. Skeletal density determination	97
A.4. Nitrogen physisorption at 77 K	97

Contents

A.5. Vapour physisorption at 298 K	97
A.6. Gravimetric isotherms	98
A.7. High throughput isotherm measuremnt	98
A.8. Powder X-ray diffraction	98
A.9. Nuclear magnetic resonance	98
Bibliography	98
B. Synthesis method of referenced materials	99
B.1. Takeda 5A reference carbon	99
B.2. MCM-41 controlled pore glass	99
B.3. Zr fumarate MOF	99
B.4. UiO-66(Zr) for defect study	99
B.5. UiO-66(Zr) for shaping study	100
B.6. MIL-100(Fe) for shaping study	100
B.7. MIL-127(Fe) for shaping study	100
Bibliography	101
C. Appendix for chapter 4	102
C.1. Calorimetry dataset UiO-66(Zr)	102
C.2. Calorimetry MIL-100(Fe)	103
C.3. Calorimetry MIL-127(Fe)	106
Bibliography	106
D. Appendix for chapter 3	108
D.1. Acid and solvent properties	108
D.2. Powder diffraction patterns	109
D.3. TGA curves	109
D.3.1. DMF leached samples	109
D.3.2. Water leached samples	110
D.3.3. Methanol leached samples	111
D.3.4. DMSO leached samples	112
D.3.5. High resolution curves	113
D.4. Nitrogen sorption isotherms	114
D.4.1. DMF leached samples	114
D.4.2. H ₂ O leached samples	115
D.4.3. MeOH leached samples	116
D.4.4. DMSO leached samples	117
D.5. Characterisation	118
Bibliography	119

1. Building a framework for adsorption data processing

1.1. Introduction

Historically, the processing of isotherms was done by hand, with large worksheets being used for the calculations. As an example, we point out that one of the initial limitations of the BJH method was that each point had to be determined with an approximation of critical pore radius, due to the tedious work involved in the calculation.⁽¹⁾

The advent of computers meant that the calculations could be performed quickly and reliably and led to the introduction of more complex methods for isotherm processing, such as the DFT method for pore size distribution.^(2,3) Commercial adsorption equipment which offers the users a complete software solution for any isotherm calculations is now commonplace and makes obtaining reports of desired properties for measured materials a matter of minutes.

Given the current ubiquitousness of adsorption as a characterisation method, particularly for investigating surfaces and porous compounds, there is a large pool of data published in the scientific community. Key performance indicators such as specific surface area, working capacity and pore volume are commonly reported in scientific literature and used as benchmarking tools for comparing performance.

Recent efforts have also focused on building a database of adsorption isotherms⁽⁴⁾, to offer a searchable pool of standardised behaviours on different materials. This serves as both a useful reference for comparing synthesised compounds, as well as a method for quickly finding suitable materials which have the desired properties for a particular application.

In this chapter an open-source software package is presented, which is released under an MIT licence and written in Python, intended to be used for manipulation, storage, visualisation and processing of adsorption isotherms. Developed internally at the MADIREL Laboratory in Marseilles, the software is aimed to give users a powerful yet easy to use package that can perform the kind of processing usually offered by commercial software.

1.2. pyGAPS overview

1.2.1. Intended use cases

The software was imagined for use in two types of scenario. First, as a command line interface, in environments such as IPython and Jupyter. The typical user working in these environments is likely to be processing a small batch of results at one time, and is interested in obtaining the results in graphical form. For this type of application, the framework should provide an unobtrusive way of importing the user data, as well as present an API which does not require extensive knowledge of processing methods. Finally, a powerful graphing environment is required which will allow the user to visualise their original dataset and results.

The second envisaged application is related to bulk data processing. Requirements here shift towards parameter control, scripting and extensibility. The framework API should offer the option to change implicit parameters, select calculation limits and return the results in a numerical form for further processing. This type of application is also likely to require storage of isotherms in a database or under other types of data files.

1.2.2. Core structure

In order to offer a clear structuring of functionality, pyGAPS introduces several classes which abstract data and functionality for facile interaction. The classes are intuitively named: Isotherm, Sample and Adsorbent.

The Isotherm class

The Isotherm class is a representation of an adsorption isotherm i.e. a function of the amount adsorbed, or loading, with pressure at a fixed temperature. The class also contains other information relating to the isotherm, such as the material name and batch it describes, the adsorbate used and other user-defined properties.

Because the aforementioned relationship can be either a physical measurement defined by individual pressure-loading pairs or a model, describing the relationship as a function rather than discrete data, the Isotherm class is used as a parent class for two subclasses: PointIsotherm, describing datapoints and ModelIsotherm containing a model such as Henry, Langmuir etc., which encapsulate the respective functionality. The two classes are interchangeable as they share most methods and properties. Once an instance of an Isotherm class is created, it can then be used for the processing, conversion and graphing capabilities of pyGAPS.

The Sample class

The isotherm classes contain the name and batch of the sample they are measured on in a string format. The user might want to specify other information about the material, such as the date of synthesis or the material's density, as well as store this information

1. Building a framework for adsorption data processing

in the database. For this case, pyGAPS provides the `Sample` class. The framework uses the string values in the isotherm to connect an `Isotherm` instance to a specific `Sample`.

The Adsorbate class

Finally, in order for many of the calculations included in pyGAPS to be performed, properties of the adsorbate used are needed e.g. liquid density, vapour pressure etc. The `Adsorbate` class is provided for this purpose, which is connected to an `Isotherm` class similarly to a `Sample`. The physical properties are either calculated in the background through an equation of state, either the open source CoolProp library⁽⁵⁾ or the NIST-made REFPROP.⁽⁶⁾ The properties can also be retrieved from the internal database or specified by the user.

1.2.3. Creation of an Isotherm

An `Isotherm` can be created either from the command line directly or through an import from a supported format. For the direct creation, the code takes two kinds of inputs: the data itself, in the form of a `pandas.DataFrame`, and the isotherm parameters describing it. Only four parameters are strictly required: the material name, the material batch, the adsorbate used and the experimental temperature. Other parameters can be passed as well and will be stored in the isotherm class.

Listing 1.1: Creating the `DataFrame`

```
1 isotherm_data = pandas.DataFrame({  
2     'pressure' : [1, 2, 3, 4, 5, 3, 2],  
3     'loading' : [1, 2, 3, 4, 5, 3, 2],  
4     'enthalpy' : [15, 15, 15, 15, 15, 15, 15],  
5     'xrd_peak_1' : [0, 0, 1, 2, 2, 1, 0],  
6 })
```

The `DataFrame` must contain a column containing the pressure points and one containing the corresponding loading points of the isotherm. Other columns can also be passed, when secondary data such as enthalpy of adsorption is present at each measurement point. These columns will be saved in the case of the `PointIsotherm` class and can be plotted afterwards.

If no unit data is specified in the constructor, the framework will assume that the isotherm is in units of mmol g⁻¹ loading as a function of bar. Both the units and the basis can be specified, as it is explained in a latter section.

Finally, the data is saved in the newly created class or used to generate parameters for a model such as BET, Langmuir, etc., in the case of a `PointIsotherm` and `ModelIsotherm` respectively. It should be noted that the creation of `Sample` and `Adsorbate` instances is similar.

Alternatively, the isotherm can be imported from a file containing a format that is recognised by pyGAPS. Parsing from suitably structured JSON, CSV and Excel files is supported.

1. Building a framework for adsorption data processing

Listing 1.2: Creating the PointIsotherm

```
1 point_isotherm = pygaps.PointIsotherm(
2
3     # First the pandas.DataFrame with the points
4     # and the keys to what the columns represent.
5
6     isotherm_data,
7
8     loading_key='loading',           # The loading column
9     pressure_key='pressure',        # The pressure column
10    other_keys=['enthalpy',
11                  'xrd_peak_1'],      # The columns containing other data
12
13    # Some of the unit parameters can be
14    # specified if desired.
15
16    pressure_mode='absolute',       # absolute pressure
17    pressure_unit='bar',            # with units of bar
18    adsorbent_basis='mass',         # adsorbent mass basis
19    adsorbent_unit='kg',            # with units of kg
20    loading_basis='mass',           # loading mass basis
21    loading_unit='g',              # with units of g
22
23    # Finally the isotherm description
24    # parameters are passed.
25
26    'sample_name' : 'carbon',       # Required
27    'sample_batch' : 'X1',           # Required
28    'adsorbate' : 'nitrogen',       # Required
29    't_exp' : 77,                  # Required
30    't_act' : 150,                 # Recognised / named
31    'user' : 'Username',           # Recognised / named
32    'DOI' : '10.000/mydoi',        # Unknown / user specific
33 )
```

1.2.4. Workflow

Once an isotherm object is created, it will be used for all further processing. The class contains methods which can be used to inspect the data visually, or retrieve parts of the isotherm such as the adsorption or desorption branches with user-chosen limits or units. Singular values of pressure or loading can be calculated, either through interpolation in the case of a `PointIsotherm` or by evaluation of the internal model in the `ModelIsotherm`. For an isotherm with datapoints, these can also be converted into different units or modes.

Characterisation functions take a single isotherm object as their first parameter. This is the case for the BET area, Langmuir area, t-plot, α_s plot, and pore size distribution methods. These characterisation functions attempt to automate as much of the process as possible. For example, the BET area limits are automatically calculated using the

1. Building a framework for adsorption data processing

Rouquerol⁽⁷⁾ method, with all the checks implemented into the code. In another example the straight line sections of the t-plot are determined automatically through a calculation of the second derivative of the transformed isotherm. For detailed control, there is an option to specify options for each individual method, such as manual BET limits, different thickness functions for the t-plot or Kelvin-based mesoporous pore distribution methods, custom parameters for the Horvath-Kawazoe microporous pore distribution, custom DFT or NLDFT kernels and more. The results are returned in a dictionary or can be directly graphed if the `verbose` parameter is passed.

1.2.5. Units

When computers work with physical data, units are often a matter that introduces confusion. Here we explain how `pyGAPS` handles units and other physical world concepts such as relative pressure and mass or volume basis.

The following dimensions can be specified for an Isotherm: the measurement *pressure*, the quantity of guest adsorbed or *loading* and the amount of adsorbent material the loading is reported on, or *adsorbent*.

Pressure can be reported either in an absolute value, in several common units such as bar, torr, Pa, or as *relative pressure*, the pressure divided by the saturation vapour pressure of the adsorbate at the respective measurement temperature. Conversions between the two modes are automatic and handled internally.

Both the *loading* and *adsorbent* can be reported in three different bases: a molar basis, a mass basis or a volume basis. Within each basis different units are recognised and can be easily converted. The conversions between bases can also easily performed if the required conversion factors (i.e. molar mass and density) are available. For *loading*, these factors are automatically calculated internally, while for the *adsorbent* they should be provided by the user in the respective `Sample` class.

1.3. Isotherm characterisation and fitting

1.3.1. Mathematical descriptions of isotherms

A lot of effort was put into attempting to describe the phenomenon of adsorption using a simple model. Through a mathematical understanding, the underlying mechanisms of adsorption can be understood. Unfortunately, the plethora of isotherm features and shapes can only be truly recreated by molecular simulation, which requires an exact knowledge of the adsorbent structure and its interaction with the adsorbed gas. Nevertheless, great strides have been taken to obtain several models which can be useful when fitted to measured isotherms for obtaining simple parameters which are representative of physical factors such as guest-host interaction, surface area, pore size, total pore volume and others. More importantly, it allows us to numerically compare measured isotherms.

A page of figures for different models with several values of their parameter can be seen in Figure 1.1.

1. Building a framework for adsorption data processing

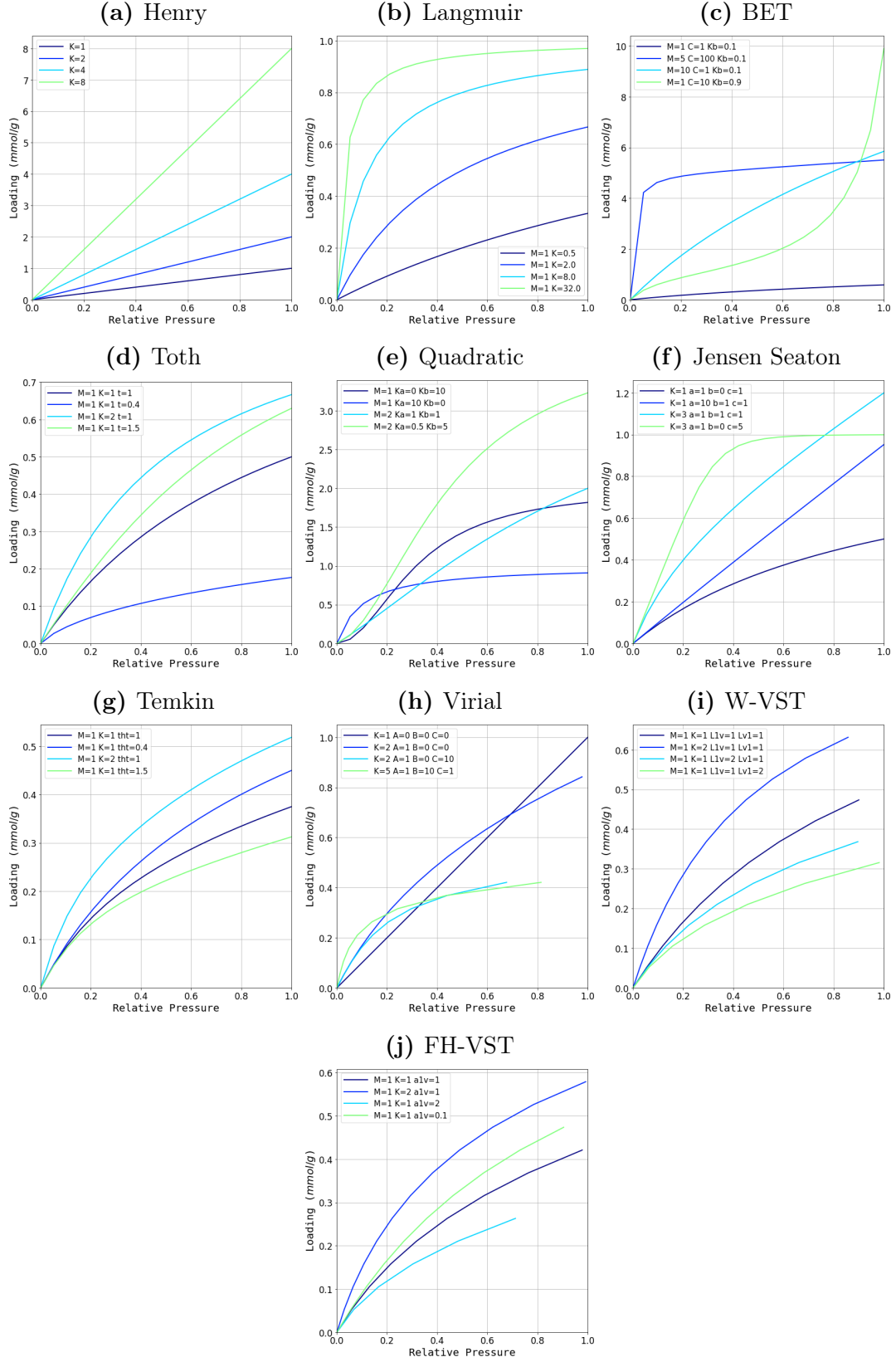


Figure 1.1.: Examples of models

1. Building a framework for adsorption data processing

The Henry model

The simplest method of describing adsorption on a surface is Henry's law. It assumes only interactions with the adsorbate surface and is described by a linear dependence of adsorbed amount with increasing pressure.

$$n_a(p) = K_H p \quad (1.1)$$

It is derived from the Gibbs equation, by substituting a two dimensional analogue to the ideal gas law. From a physical standpoint, Henry's law is unrealistic as adsorption sites will saturate at higher pressures. However, the constant K_H , or Henry's constant, can be thought of as a measure of the strength of the interaction of the probe gas with the surface. At very low concentrations of gas there is a theoretical requirement for the applicability of Henry's law. Therefore, most models reduce to Equation 1.1 as $\lim_{p \rightarrow 0} n(p)$.

Langmuir and multi-site Langmuir model

The Langmuir theory⁽⁸⁾, proposed at the start of the 20th century, states that adsorption takes place on specific sites on a surface, until all sites are occupied. It is derived from a kinetic model of gas adsorption and is based on several assumptions:

- All sites are equivalent and have the same chance of being occupied.
- Each adsorbate molecule can occupy one adsorption site.
- There are no interactions between adsorbed molecules.
- The rates of adsorption and desorption are proportional to the number of sites currently free and currently occupied, respectively.
- Adsorption is complete when all sites are filled.

Using these assumptions we can define rates for both adsorption and desorption. The adsorption rate (Equation 1.2) will be proportional to the number of sites available on the surface, as well as the number of molecules in the gas, which is given by pressure. The desorption rate, on the other hand, will be proportional to the number of occupied sites and the energy of adsorption (Equation 1.3). It is also useful to define $\theta = n_a/n_a^m$ as the surface coverage, the number of sites occupied divided by the total sites. At equilibrium, the rate of adsorption and the rate of desorption are equal, therefore the two equations can be combined. The equation can then be arranged to obtain an expression for the loading called the Langmuir model (Equation 1.6).

1. Building a framework for adsorption data processing

$$v_a = k_a p(1 - \theta) \quad (1.2)$$

$$v_d = k_d \theta \exp\left(-\frac{E}{RT}\right) \quad (1.3)$$

$$v_a = v_d \quad (1.4)$$

$$k_a p(1 - \theta) = k_d \theta \exp\left(-\frac{E}{RT}\right) \quad (1.5)$$

$$n_a(p) = n_a^m \frac{K_p}{1 + K_p} \quad (1.6)$$

The Langmuir constant K is the product of the individual desorption and adsorption constants k_a and k_d and exponentially related to the energy of adsorption $\exp(-E/RT)$.

A common extension to the Langmuir model is to consider the experimental isotherm to be the sum of several Langmuir-type isotherms, each with specific maximum coverage and affinities. The underlying assumption is that the adsorbent has several distinct types of homogeneous adsorption sites and a Langmuir equation is used for each. This is particularly applicable in cases where the structure of the adsorbent suggests that different types of sites are present, such as in crystalline materials of variable chemistry like zeolites and MOFs. The resulting isotherm equation is:

$$n_a(p) = \sum_i n_{a,i}^m \frac{K_i p}{1 + K_i p} \quad (1.7)$$

In practice, only up to three adsorption sites are usually considered.

BET model

The BET model⁽⁹⁾ assumes that adsorption takes place on the surface of the material in incremental layers according to several assumptions:

- The adsorption sites are equivalent, and therefore the surface is heterogeneous.
- There are no lateral interactions between adsorbed molecules.
- The adsorption takes place in layers, with adsorbed molecules acting as sites for the next layer.

A particular surface percentage θ_x is occupied with x layers. For each layer at equilibrium, the adsorption and desorption rates must be equal. We can then apply the Langmuir theory for each layer as presented in Table Table 1.1. We can assume that the adsorption energy of a molecule on the second and higher layers is just the condensation energy of the adsorbent $E_{i>1} = E_L$. Since we are assuming that all layers beside the first have the same properties, we can also define $g = k_{d_2} k_{a_2} = k_{d_3} k_{a_3} = \dots$.

The coverage for each layer θ can now be expressed in terms of θ_0 .

1. Building a framework for adsorption data processing

Table 1.1.: Derivation of the BET method applied for, each adsorbed layer

All layers	Re-arranged
$k_{a_1}p\theta_0 = k_{d_1}\theta_1 \exp\left(-\frac{E_1}{RT}\right)$	$p\theta_0 = \frac{k_{d_1}}{k_{a_1}}\theta_1 \exp\left(-\frac{E_1}{RT}\right)$
$k_{a_2}p\theta_1 = k_{d_2}\theta_2 \exp\left(-\frac{E_2}{RT}\right)$	$p\theta_1 = g\theta_2 \exp\left(-\frac{E_L}{RT}\right)$
$k_{a_2}p\theta_2 = k_{d_3}\theta_3 \exp\left(-\frac{E_3}{RT}\right)$	$p\theta_2 = g\theta_3 \exp\left(-\frac{E_L}{RT}\right)$
\vdots	\vdots
$k_{a_i}p\theta_{i-1} = k_{d_i}\theta_i \exp\left(-\frac{E_i}{RT}\right)$	$p\theta_{i-1} = g\theta_i \exp\left(-\frac{E_L}{RT}\right)$

$$\theta_i = \left[p \frac{k_{a_1}}{k_{d_1}} \exp\left(-\frac{E_1}{RT}\right) \right] x^{i-1} \theta_0 \quad (1.8)$$

where

$$x = \frac{p}{g} \exp\left(-\frac{E_L}{RT}\right) \quad (1.9)$$

A constant C may be defined such that:

$$C = \frac{k_{a_1}}{k_{d_1}} g \exp\left(\frac{E_1 - E_L}{RT}\right) \quad (1.10)$$

$$\theta_i = C x^i \theta_0 \quad (1.11)$$

For all the layers, the equations can be summed:

$$\frac{n}{n_m} = \sum_{i=1}^{\infty} i \theta^i = C \sum_{i=1}^{\infty} i x^i \theta_0 \quad (1.12)$$

and since

$$\theta_0 = 1 - \sum_{i=1}^{\infty} \theta_i \sum_{i=1}^{\infty} i x^i = \frac{x}{(1-x)^2} \quad (1.13)$$

Then we obtain the BET equation:

$$n_a(p) = n_a^m \frac{C(p/p_0)}{(1-p/p_0)[1-(p/p_0) + C(p/p_0)]} \quad (1.14)$$

1. Building a framework for adsorption data processing

The BET constant C is a measure of the interaction with the adsorption surface and can be seen to influence the “knee” a BET-type isotherm has at low pressure, before the statistical monolayer formation.

Toth model

The Toth model is an empirical modification to the Langmuir equation (Equation 1.6) which introduces a power parameter for the denominator leading to the following formula:

$$n_a(p) = n_a^m \frac{Kp}{[1 + (Kp)^t]^{1/t}} \quad (1.15)$$

The parameter t is a measure of the system heterogeneity. Thanks to this additional parameter, the Toth equation can accurately describe a large number of adsorbent/adsorbate systems and, due to its correct behaviour in both the low and high pressure limits, is recommended as the fitting isotherms of many adsorbents such as hydrocarbons, carbon oxides, hydrogen sulphide and alcohols on activated carbons and zeolites.

Temkin model

The Temkin adsorption isotherm⁽¹⁰⁾, like the Langmuir model, considers a surface with n_a^m identical adsorption sites, but takes into account adsorbate- adsorbate interactions by assuming that the heat of adsorption is a linear function of the coverage. This expression for the Temkin isotherm is derived using a mean-field argument and uses an asymptotic approximation to obtain an explicit equation for the loading.⁽¹¹⁾

$$n_a(p) = n_a^m \frac{Kp}{1 + Kp} + n_a^m \theta \left(\frac{Kp}{1 + Kp} \right)^2 \left(\frac{Kp}{1 + Kp} - 1 \right) \quad (1.16)$$

Here, n_a^m and K have the same physical meaning as in the Langmuir model. The additional parameter θ describes the strength of the adsorbate-adsorbate interactions ($\theta < 0$ for attractions).

Jensen-Seaton model

When modelling adsorption in micropores, a requirement was highlighted by Jensen and Seaton in 1996⁽¹²⁾ that at sufficiently high pressures the adsorption isotherm should not reach a horizontal plateau corresponding to saturation but that this asymptote should continue to rise due to the compression of the adsorbate in the pores. They developed a semi-empirical equation to describe this phenomenon based on a function that interpolates between two asymptotes: the Henry’s law asymptote at low pressure and an asymptote reflecting the compressibility of the adsorbate at high pressure.

$$n(p) = K_{HP} \left(1 + \frac{K_{HP}}{[a(1+bp)]^c} \right)^{(-1/c)} \quad (1.17)$$

1. Building a framework for adsorption data processing

Here K_H is the Henry constant, b is the compressibility of the adsorbed phase and c an empirical constant.

The equation can be used to model both absolute and excess adsorption as the pore volume can be incorporated into the definition of b , although this can lead to negative adsorption slopes for the compressibility asymptote. This equation has been found to provide a better fit for experimental data from microporous solids than the Langmuir or Toth equation, in particular for adsorbent/adsorbate systems with high Henry's constants where the amount adsorbed increases rapidly at relatively low pressures and then slows down dramatically.

Quadratic model

The quadratic adsorption isotherm⁽¹³⁾ exhibits an inflection point. The loading is convex at low pressures but changes concavity as it saturates, yielding an S-shape. The S-shape can be explained by adsorbate-adsorbate attractive forces; the initial convexity is due to a cooperative effect of adsorbate-adsorbate attractions aiding in the recruitment of additional adsorbate molecules.

$$n(p) = n_a^m \frac{(K_a + 2K_bp)p}{1 + K_{ap} + K_{bp}^2} \quad (1.18)$$

The parameter K_a can be interpreted as the Langmuir constant; the strength of the adsorbate-adsorbate attractive forces is embedded in K_b .

Virial model

A virial isotherm model attempts to fit the measured data to a factorized exponent relationship between loading and pressure.⁽¹⁴⁾

$$p = n \exp(K_1 n^0 + K_2 n^1 + K_3 n^2 + K_4 n^3 + \dots + K_i n^{i-1}) \quad (1.19)$$

It has been applied with success to describe the behaviour of standard as well as supercritical isotherms. The factors are usually empirical, although some relationship with physical properties can be determined: the first constant is related to the Henry constant at zero loading, while the second constant is a measure of the interaction strength with the surface.

$$K_1 = -\ln K_{H,0} \quad (1.20)$$

In practice, besides the first constant, only 2-3 factors are used.

1. Building a framework for adsorption data processing

Vacancy solution theory models

As a part of the Vacancy Solution Theory (VST) family of models, it is based on concept of a “vacancy” species, denoted v , and assumes that the system consists of a mixture of these vacancies and the adsorbate.

The VST model is defined as follows:

- A vacancy is an imaginary entity defined as a vacuum space which acts as the solvent in both the gas and adsorbed phases.
- The properties of the adsorbed phase are defined as excess properties in relation to a dividing surface.
- The entire system including the adsorbent are in thermal equilibrium however only the gas and adsorbed phases are in thermodynamic equilibrium.
- The equilibrium of the system is maintained by the spreading pressure which arises from a potential field at the surface

It is possible to derive expressions for the vacancy chemical potential in both the adsorbed phase and the gas phase, which when equated give the following equation of state for the adsorbed phase:

$$\pi = -\frac{R_g T}{\sigma_v} \ln y_v x_v \quad (1.21)$$

where y_v is the activity coefficient and x_v is the mole fraction of the vacancy in the adsorbed phase. This can then be introduced into the Gibbs equation to give a general isotherm equation for the Vacancy Solution Theory where K_H is the Henry's constant and $f(\theta)$ is a function that describes the non-ideality of the system based on activity coefficients:

$$p = \frac{n_{ads}}{K_H} \frac{\theta}{1-\theta} f(\theta) \quad (1.22)$$

The general VST equation requires an expression for the activity coefficients. The Wilson⁽¹⁵⁾ equation can be used, which expresses the activity coefficient in terms of the mole fractions of the two species (adsorbate and vacancy) and two constants Λ_{1v} and Λ_{v1} . The equation becomes:

$$p = \left(\frac{n_{ads}}{K_H} \frac{\theta}{1-\theta} \right) \left(\Lambda_{1v} \frac{1 - (1 - \Lambda_{v1})\theta}{\Lambda_{1v} + (1 - \Lambda_{v1})\theta} \right) \exp \left(- \frac{\Lambda_{v1}(1 - \Lambda_{v1})\theta}{1 - (1 - \Lambda_{v1})\theta} - \frac{(1 - \Lambda_{1v})\theta}{\Lambda_{1v} + (1 - \Lambda_{1v})\theta} \right) \quad (1.23)$$

1. Building a framework for adsorption data processing

Cochran⁽¹⁶⁾ developed a simpler, three parameter equation based on the Flory–Huggins equation for the activity coefficient. The equation for then becomes:

$$p = \left(\frac{n_{ads}}{K_H} \frac{\theta}{1-\theta} \right) \exp \frac{\alpha_{1v}^2 \theta}{1+\alpha_{1v}\theta} \quad \text{where} \quad \alpha_{1v} = \frac{\alpha_1}{\alpha_v} - 1 \quad (1.24)$$

Here α_1 and α_v are the molar areas of the adsorbate and the vacancy respectively.

1.3.2. Specific surface area and pore volume calculations

As adsorption takes place on the surface, isotherms measured on porous materials are uniquely suited for the determination of the accessible area of the void space present inside the material structure or external area of fine powders. pyGAPS comes with several common methods used to determine surface area, some with theoretical basis like the IUPAC-recommended BET method and some empirical, such as the t-plot method.

BET surface area

The BET method⁽⁹⁾ for determining surface area is the recommended IUPAC method⁽¹⁷⁾ to calculate the surface area of a porous material. It is generally applied on isotherms obtained through N₂ adsorption at 77 K, although other adsorbates (Ar at 77 K or 87 K, Kr at 77 K, CO₂ at 293 K) have been used. In principle, any probe with an adsorption behaviour which can be described through the BET equation in the low pressure regime can be used.

As previously mentioned, the method assumes that adsorption takes place in incremental layers according to the BET model (section 1.3.1). Even if the adsorbent is porous, the initial amount adsorbed (usually between 0.05–0.4 p/p_0) can be described through the equation written in its linear form:

$$\frac{p/p_0}{n_{ads}(1-p/p_0)} = \frac{1}{n_m C} + \frac{C-1}{n_m C} (p/p_0) \quad (1.25)$$

If we plot the isotherm points as $(p/p_0)/n_{ads}(1-p/p_0)$ versus p/p_0 , a linear region can usually be found. The slope and intercept of this line can then be used to calculate n_m , the amount adsorbed at the statistical monolayer, as well as C , the BET constant.

$$n_m = \frac{1}{s+i} \quad C = \frac{s}{i} + 1 \quad (1.26)$$

From the BET monolayer capacity, the specific surface area can be calculated if the area taken up by one of the adsorbate molecules on the surface is known. The calculation uses the following equation together with Avogadro's number:

$$a_{BET} = n_m A_N \sigma \quad (1.27)$$

1. Building a framework for adsorption data processing

While commonly used for surface area determination, the BET area should be used with care, as the assumptions made in its calculation may not hold. To augment the validity of the BET method, Rouquerol⁽⁷⁾ proposed several checks to ensure that the selected BET region is valid:

- The BET (C) obtained should be positive;
- In the corresponding Rouquerol plot where $n_{ads}(1 - p/p_0)$ is plotted with respect to p/p_0 , the points chosen for BET analysis should be strictly increasing;
- The loading at the statistical monolayer should be situated within the limits of the BET region.

All these checks are implemented in pyGAPS. Regardless, the BET surface area should still be interpreted carefully. Since adsorption takes place on the pore surface, microporous materials which have pores of similar or smaller size as the probe molecule used will not give a realistic surface area since in the micropore range it is difficult to separate pore condensation behaviour from multilayer adsorption. Furthermore, the cross-sectional area of the molecule on the surface cannot be guaranteed. For example, nitrogen has been known to adopt a different conformation on the surface of some materials due to inter-molecular forces, which effectively lowers its cross-sectional area.⁽⁷⁾

In pyGAPS, starting from an isotherm object, it is easy to calculate the BET area by using the code in Listing 1.3. The framework automatically applies the Rouquerol rules to find the optimum pressure range and returns the results as a dictionary. The `verbose=True` option prints a short text with all the calculation variables as well as graphing the BET and Rouquerol plots (Figure 1.2). The user can override automatic pressure range selection by using the range parameter (`limits=(0.05, 0.3)`).

Listing 1.3: Calculating a BET area

```
1 area_dict = pygaps.area_BET(isotherm, verbose=True)
```

```
BET surface area: a = 1277 m2/g
Minimum pressure point chosen is 0.005 and maximum is 0.034
The slope of the BET fit:      s = 76.344
The intercept of the BET fit: i = 0.052
BET constant:                 C = 1463
Amount for a monolayer:       n = 0.01309 mol/g
```

Langmuir surface area

The Langmuir equation (Equation 1.6) can be also be expressed in a linear form by rearranging it as:

$$\frac{p}{n} = \frac{1}{Kn_m} + \frac{p}{n_m} \quad (1.28)$$

1. Building a framework for adsorption data processing

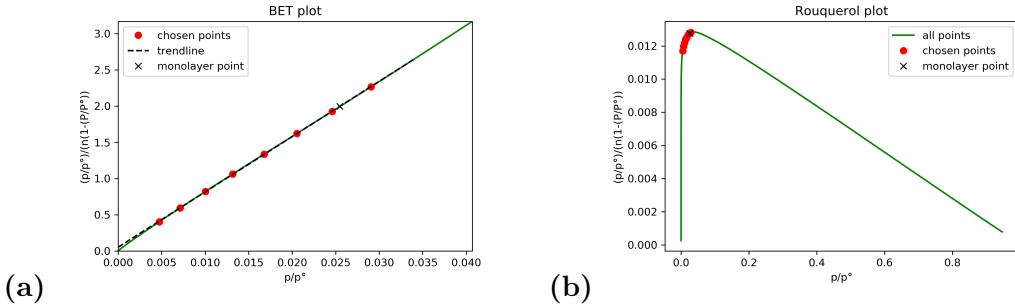


Figure 1.2.: Output from the BET area function (a) the BET plot showing the selected points for fitting the equation, as well as the location of the statistical monolayer and (b) the Rouquerol plot for this calculation.

Assuming the data can be fitted with a Langmuir model, by plotting p/n against pressure, a straight line will be obtained. The slope and intercept of this line can then be used to calculate n_m , the amount adsorbed at the monolayer, as well as K , the Langmuir constant.

$$n_m = \frac{1}{s} \quad K = \frac{1}{i * n_m} \quad (1.29)$$

The surface area can then be calculated by using the monolayer capacity in a manner analogous to the BET surface area method.

$$a_{Langmuir} = n_m A_N \sigma \quad (1.30)$$

The Langmuir method for determining surface area assumes that adsorption takes place until all active sites on the material surface are occupied, or until monolayer formation in the case of complete surface coverage. As most adsorption processes (except chemisorption) don't follow this behaviour, it is important to regard the Langmuir surface area as an estimate.

As with the BET area, the Langmuir area is calculated by using the code in Listing 1.4. The framework will alert the user if the correlation is not linear in the selected range. Here the `verbose=True` option prints a short text with all the calculation variables and the graphs the Langmuir plot as seen in Figure 1.3a. If desired the user can override automatic pressure range selection as seen in the second example in Listing 1.4.

Listing 1.4: Calculating a Langmuir area

```
1 area_dict = pygaps.area_langmuir(isotherm, verbose=True)
```

| WARINING The correlation is not linear!

```
1 area_dict = pygaps.area_langmuir(isotherm,
2                               limits=(0.05, 0.3),
3                               verbose=True)
```

1. Building a framework for adsorption data processing

```

Langmuir surface area: a = 415 m2/g
Minimum pressure point chosen is 0.0 and maximum is 0.194
The slope of the Langmuir line: s = 234.968
The intercept of the Langmuir line: i = 1.607
The Langmuir constant is: K = 146
Amount for a monolayer: n = 0.00426 mol/g

```

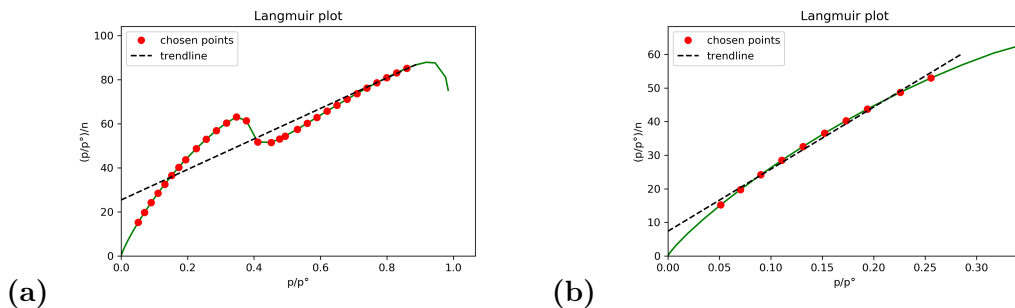


Figure 1.3.: Output from the Langmuir area function (a) the Langmuir plot showing the automatic fitting attempt which generates a warning and (b) a manually selected pressure range for the Langmuir plot.

Ideal isotherms or thickness functions

The initial part of an isotherm (the Henry regime) can be seen to be very dependent on the interactions between the adsorbate and the surface. However, the subsequent layers are less influenced by the material and can often be assumed, like in the BET model, to have an energy of adsorption identical to the enthalpy of liquefaction of the bulk liquid and therefore, their formation depends essentially only on the partial pressure.

With this assumption, several studies have been focused on obtaining an “ideal” isotherm of adsorption on a non-porous material which can then, if the cross-sectional area of the molecule is known, be transformed in a function capable of predicting the multilayer thickness as a function of pressure. This kind of empirical function, also referred to as a *thickness function* or *t-curve*, can then be used as an alternative method for surface area determination, as explained in the next section. These curves are also used in the classical methods for calculating mesoporous size distributions. It is important to clarify that the function is only applicable for a single adsorbent and a single temperature.

Several common thickness functions have been implemented in pyGAPS, applicable for nitrogen at 77K such as the Halsey⁽¹⁸⁾ (Equation 1.31) and the Harkins and Jura⁽¹⁹⁾ (Equation 1.32) curve.

check
equations

1. Building a framework for adsorption data processing

$$t_{Halsey} = 0.354 \left(\frac{-5}{\log(p/p_0)} \right)^{1/3} \quad (1.31)$$

$$t_{Harkins\&Jura} = \left(\frac{0.1399}{0.034 - \log_{10}(p/p_0)} \right)^{1/2} \quad (1.32)$$

These t-curves are selected by name as parameters in the functions that use them. The user can also define their own t-curve as a function and pass it as a parameter. An example is shown in Listing 1.5 in the t-plot section.

t-plot Method

The t-plot method is an empirical method, developed as a tool to determine the surface area of porous materials, which can also be used for other calculations, such as external pore area and micropore volume calculations.⁽²⁰⁾ A plot is constructed, where the isotherm loading data is plotted versus the ideal thickness of the adsorbate layer, obtained through the a t-curve (section 1.3.2). It stands to reason that, in the case when the experimentally measured loading follows the model, a straight line will be obtained with its intercept through the origin. However, since in most cases there are differences between adsorption in the pores and ideal surface adsorption, the t-plot will deviate and form features which can be analysed to describe the material characteristics.

- A sharp vertical deviation will indicate condensation in a type of mesopore structure.
- A gradual slope will indicate adsorption on a specific surface.

The slope of the linear section can be used to calculate the area where adsorption is taking place. If the linear region occurs at low loadings, it will represent the total surface area of the material. If at the end of the curve, it will instead represent adsorption on the external surface area of the sample. The formula to calculate the area is presented in Equation 1.33, where ρ_l is the liquid density of the adsorbate at experimental conditions.

$$a_{surface} = \frac{sM_m}{\rho_l} \quad (1.33)$$

If the region selected is after a vertical deviation, the intercept of the line will no longer pass through the origin. This intercept can be used to calculate the volume of the filled pore through the following equation:

$$V_{ads} = \frac{iM_m}{\rho_l} \quad (1.34)$$

Since the t-plot method is comparing the experimental isotherm with an ideal model, care must be taken to ensure that the t-curve is an accurate representation of the thickness of the adsorbate multilayers on the surface of the adsorbent. Since there is no such

1. Building a framework for adsorption data processing

thing as a universal thickness curve, care must be taken when selecting a thickness model to ensure that it is applicable to both the material and the adsorbate. Also, features on the t-plot found at loadings lower than the monolayer thickness do not have any physical meaning.

In pyGAPS, when the function is called without any parameters except an isotherm, the framework will attempt to find plateaus in the data and automatically fit them with a straight line, returning a dictionary with the slope, intercept and calculated pore volume and specific area for each linear region found. As an example, the first function in Listing 1.5 will generate the graph in Figure 1.4a. The isotherm in this example is measured on a sample of MCM-41.

Listing 1.5: Generating a t-plot

```

1 # using automatic region detection
2 pygaps.t_plot(isotherm, verbose=True)
3
4 # specifying a manual region
5 pygaps.t_plot(isotherm, limits=(0.3,0.44), verbose=True)
6
7 # using the Halsey thickness curve
8 pygaps.t_plot(isotherm, thickness_model='Halsey', verbose=True)
9
10 # defining a custom t-curve to use in the t-plot
11 def carbon_model(relative_p):
12     return 0.88*(relative_p**2) + 6.45*relative_p + 2.98
13
14 pygaps.t_plot(isotherm, thickness_model=carbon_model, verbose=True)

```

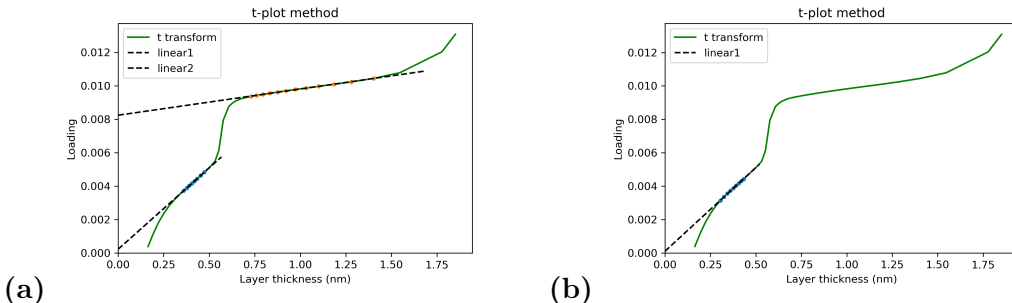


Figure 1.4.: Output from the t-plot method function (a) an automatically obtained t-plot with the calculated fit regions and (b) a manually selected range for the t-plot.

The first linear region in Figure 1.4a can be attributed to adsorption on the mesopore surface, while the second one represents adsorption on the available surface after mesopore filling. Therefore, the surface area values calculated for the first and second region correspond to the area of the mesopores and the external particle area, respectively. As

1. Building a framework for adsorption data processing

only one pore filling event occurs, the pore volume calculated for the second region gives us the mesopore volume. We can obtain a more accurate result for the surface area by fitting the first linear region to a zero intercept through manual region selection, as shown in the second example in Listing 1.5.

Finally, the framework allows for the thickness model to be substituted with an user-provided function which will be used for the t-plot, as mentioned before in section 1.3.2. Usage of a carbon black-type thickness curve is presented in the last example in Listing 1.5.

α_s Method

In order to extend the t-plot analysis with other adsorbents and non-standard thickness curves, the α_s method was devised.⁽²¹⁾ Instead of attempting to find an ideal isotherm that describes the thickness of the adsorbed layer, a reference isotherm is used. This isotherm is measured on a non-porous version of the same material, assumed to have identical surface characteristics. The dimensionless α_s values are obtained from this isotherm by dividing the loading values by the amount adsorbed at a specific relative pressure, usually taken as $p/p_0 = 0.4$ since nitrogen hysteresis loops theoretically close at this point.

$$\alpha_s = \frac{n_a}{n_{0.4}} \quad (1.35)$$

The analysis then proceeds as in the t-plot method, with the same explanation for observed features. The only difference is that the surface area calculation from linear regions observed uses the known specific area of the reference material.

$$A = \frac{sA_{ref}}{(n_{ref})_{0.4}} \quad (1.36)$$

The reference isotherm chosen for the α_s method must be a description of the adsorption on a completely non-porous sample of the same material. It is often impossible to obtain such non-porous versions, therefore care must be taken how the reference isotherm is measured.

To generate an α_s -plot in pyGAPS, both an analysis isotherm and a reference isotherm must be supplied as shown in Listing 1.6. In this example, the reference isotherm is measured on non-porous silica. The reference material area can be specified by using the `reference_area` parameter. If not specified, it is automatically calculated by applying the BET method on the reference isotherm.

Listing 1.6: Generating an α_s -plot

```
1 pygaps.alpha_s(isotherm,
2                  reference_isotherm=isotherm_r,
3                  verbose=True)
```

1. Building a framework for adsorption data processing

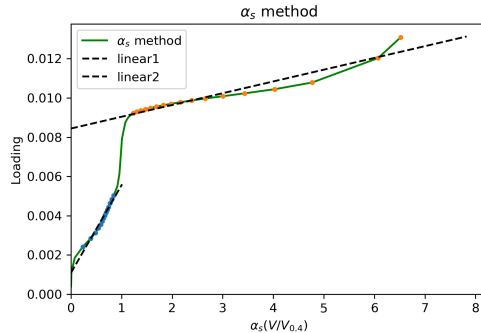


Figure 1.5.: Output from the α_s -plot function showing two automatically fit regions.

1.3.3. Assessing porosity

Characterization of pore sizes and their distribution in porous materials is often the main goal when performing adsorption experiments. It is therefore important that pyGAPS includes several robust methods for determining pore distribution from isotherm data.

When it comes to porous materials, three kinds of pore sizes have been defined, based on their lengthscales: micropores ($<2\text{ nm}$), mesopores (2 nm to 50 nm), and macropores ($>50\text{ nm}$).

Macropores are generally unable to be characterised through adsorption, with methods such as mercury intrusion porosimetry as the standard for pore size distributions at this lengthscale, although other alternatives have been suggested⁽²²⁾ due to the high toxicity of mercury. These methods are therefore outside the scope of this framework.

In the mesopore range, the “classical” methods are usually applied, which are based on the application of Kelvin’s equation pertaining to capillary condensation. This equation calculates the critical pressure at which the fluid completely files a pore of a specific diameter. This equation, applicable to a range of geometries is used in multiple approaches such as the Barrett-Joyner-Halenda (BJH) method or the Dollimore-Heal (DH) method.

For microporous materials, the Kelvin equation, with its assumption of continuous fluid properties and comparable density of the adsorbed state to bulk liquid density breaks down. An atomistic approach is required here, to address the interaction between solid-fluid and fluid-fluid through potential functions. The Horvath-Kawazoe or HK method is often used, and it is implemented in pyGAPS.

Finally, methods based on density functional theory (DFT) and derivations such as non-local DFT (NLDFT) and quenched solid state DFT (QSDFT) should be mentioned, as they can be used for multiscale (micropore and mesopore) characterisation. These methods rely on *in-silico* simulation of isotherms on a range of pore sizes, which can then be collated in a so-called *DFT kernel*, able to be used in decomposition of a experimental isotherm to obtain a pore size distribution. While the generation of DFT kernels is outside the scope of the pyGAPS framework, it is able to use user-provided kernels to fit adsorption isotherms, and comes with a basic kernel for N₂ adsorption at 77 K on carbon slit pores.

It should be noted that all methods here described require knowledge of the pore

1. Building a framework for adsorption data processing

geometry and depend on the material having pores which conform to a well-defined shape. Real adsorbents usually have interconnected networks of irregular pores, which the ideal pores used in these models merely approximate.

Mesoporous size distribution

The Kelvin equation Since the Kelvin equation is the basis of both the BJH and DH methods its theory and its implementation will be described here. The original form of the equation (Equation 1.37) gives the dependence of pressure on the radius of curvature of a meniscus in a pore r by means of surface tension γ , molar liquid volume, here expressed as $v_l = M_m/\rho_l$ and the fluid contact angle with the surface θ . The fluid is often assumed to be fully wetting, with $\theta = 0$ and $\cos \theta = 1$.

$$\ln\left(\frac{p}{p_0}\right) = -\frac{\gamma M_m}{\rho_l RT} \frac{2 \cos \theta}{r} \quad (1.37)$$

To apply the Kelvin equation to different types of pore systems, the generalized form presented in Equation 1.38 is used. It replaces the meniscus radius by a mean radius of curvature r_m .

$$\ln\left(\frac{p}{p_0}\right) = -\frac{\gamma M_m}{\rho_l RT} \frac{2}{r_m} \quad (1.38)$$

The mean radius of curvature is defined through the two principal radii of the curved interface.

$$\frac{1}{r_m} = \frac{1}{2} \left(\frac{1}{r_1} + \frac{1}{r_2} \right) \quad (1.39)$$

The relationship of the kelvin radius r_m to the actual pore radius is more subtle, as it depends on pore geometry and the filling state of the pore.⁽²³⁾ If considering a cylindrical pore open at both ends, the radius reduces to the original Kelvin equation during the desorption phase, and takes other values with different combinations of parameters as can be seen in Table 1.2.

Table 1.2.: Relationship between pore geometry, pore filling and meniscus geometry

Pore geometry	Pore filling	
	Adsorption	Desorption
slit	cylindrical	concave
cylinder	cylindrical	spherical
sphere	spherical	spherical

According to Rouquerol⁽⁷⁾, in adopting this approach, it is assumed that:

1. Building a framework for adsorption data processing

- The Kelvin equation is applicable over the pore range (mesopores). Therefore in pores which are below a certain size (around 2.5 nm), the granularity of the liquid-vapour interface becomes too large for classical bulk methods to be applied.
- The meniscus curvature is controlled by the pore size and shape. Ideal shapes for the curvature are assumed.
- Pores are rigid and of well defined shape. Their geometry considered to be invariant across the entire adsorbate.
- The filling/emptying of each pore does not depend on its location.
- Adsorption on the pore walls is not different from surface adsorption.

The Barrett, Joyner and Halenda (BJH) method The BJH method for calculating pore size distribution is based on a classical description of the adsorbate behaviour in the adsorbent pores.⁽¹⁾ Under this method, the adsorbate is adsorbing on the pore walls in a predictable way, and decreasing the apparent pore volume until condensation takes place, filling the entire pore. The critical radius is a sum of two radii, the adsorbed layer thickness, which can be modelled by a thickness model (such as Halsey, Harkins & Jura or similar as presented in section 1.3.2) and a critical radius model for condensation/evaporation, based on a form of the Kelvin equation.

$$r_p = t + r_k \quad (1.40)$$

The original model uses the desorption curve as a basis for calculating pore size distribution. Between two points of the curve, the volume desorbed can be described as the volume contribution from pore evaporation and the volume from layer thickness decrease as per Equation 1.40. The computation is done cumulatively, starting from the filled pores and calculating for each point the volume adsorbed in a pore from the following equation:

$$V_p = \left(\frac{\bar{r}_p}{\bar{r}_k + \Delta t_n} \right)^2 \left(\Delta V_n - \Delta t_n \sum_{i=1}^{n-1} \Delta A_p + \Delta t_n \bar{t}_n \sum_{i=1}^{n-1} \frac{\Delta A_p}{\bar{r}_p} \right) \quad (1.41)$$

where

$$A = 2\Delta V_p / r_p \quad (1.42)$$

here

- ΔA_p is the area of the pores
- ΔV_p is the adsorbed volume change between two points

1. Building a framework for adsorption data processing

- \bar{r}_p is the average pore radius calculated as a sum of the kelvin radius and layer thickness of the pores at pressure p between two measurement points
- \bar{r}_k is the average kelvin radius between two measurement points
- \bar{t}_n is the average layer thickness between two measurement points
- Δt_n is the average change in layer thickness between two measurement points

Then, by plotting $\Delta V/(2 * \Delta r_p)$ versus the width of the pores calculated for each point, the pore size distribution can be obtained.

In order to calculate the

Listing 1.7: PSD using the BJH method

```

1 result_dict = pygaps.mesopore_size_distribution(
2     charact_iso,
3     psd_model='BJH',
4     verbose=True
5 )

```

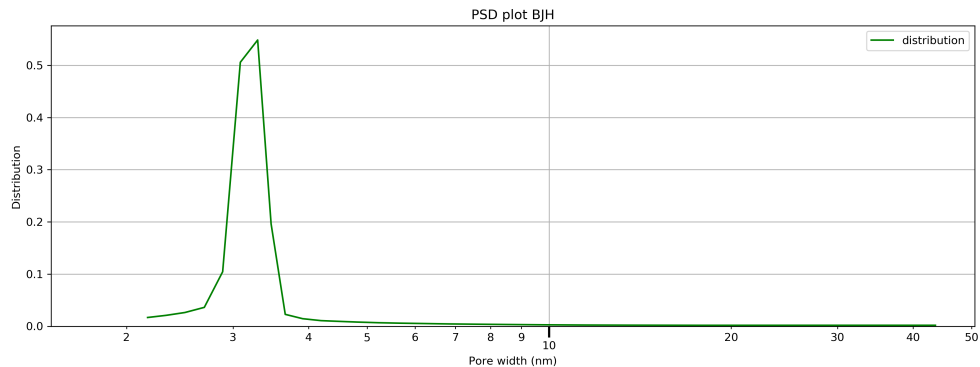


Figure 1.6.: BJH pore size distribution

The Dollimore-Heal (DH) method The DH or Dollimore-Heal method⁽²⁴⁾ of calculating pore size distribution is an extension of the BJH method which takes into account the geometry of the pores by introducing a length component.

Like the BJH method, it is based on a classical description of the adsorbate behaviour in the adsorbent pores.

$$V_p = \left(\frac{\bar{r}_p}{\bar{r}_k + \Delta t_n} \right)^2 \left(\Delta V_n - \Delta t_n \sum_{i=1}^{n-1} \Delta A_p + 2\pi \Delta t_n \bar{t}_n \sum_{i=1}^{n-1} L_p \right) \quad (1.43)$$

$$A = 2\Delta V_p / r_p \quad (1.44)$$

$$L = \Delta A_p / 2\pi r_p \quad (1.45)$$

Where:

1. Building a framework for adsorption data processing

- ΔA_p is the area of the pores
- ΔV_p is the adsorbed volume change between two points
- \bar{r}_p is the average pore radius calculated as a sum of the kelvin radius and layer thickness of the pores at pressure p between two measurement points
- \bar{r}_k is the average kelvin radius between two measurement points
- \bar{t}_n is the average layer thickness between two measurement points
- Δt_n is the average change in layer thickness between two measurement points

Then, by plotting $\Delta V/(2 * \Delta r_p)$ versus the width of the pores calculated for each point, the pore size distribution can be obtained.

Microporous size distribution

When it comes to micropores (width <2 nm), classical fluid methods stop being viable. Adsorption of molecules in these pores of comparable scale is highly dependent on the surface properties and on guest-host interaction and leads to adsorbate densities often very different than those in the bulk liquid state. In order to model adsorption in such pores, a good description of both solid-fluid and fluid-fluid potential functions is required.

The Horvath-Kawazoe (HK) method The H-K method attempts to describe the adsorption within pores by calculation of the average potential energy for a pore.⁽²⁵⁾ The method starts by assuming the relationship between the gas phase as being:

$$R_g T \ln\left(\frac{p}{p_0}\right) = U_0 + P_a \quad (1.46)$$

Here U_0 is the potential function describing the surface to adsorbent interactions and P_a is the potential function describing the adsorbate-adsorbate interactions. This equation is derived from the equation of the free energy of adsorption at constant temperature where the term $T \Delta S^{tr}(w/w_\infty)$ is assumed to be negligible.

If it is assumed that a Lennard-Jones potential function can describe the interactions between adsorbate and surface molecules, then the two contributions to the total potential can be replaced by the extended function in Equation 1.47.

$$\begin{aligned} RT \ln(p/p_0) &= N_A \frac{n_a A_a + n_A A_A}{2\sigma^4(l-d)} \\ &\times \int_{d/2}^{1-d/2} \left[-\left(\frac{\sigma}{r}\right)^4 + \left(\frac{\sigma}{r}\right)^{10} - \left(\frac{\sigma}{l-r}\right)^4 + \left(\frac{\sigma}{l-r}\right)^{10} \right] dx \quad (1.47) \end{aligned}$$

where l is the width of the pore, d defined as $d = d_a + d_A$ is the sum of the diameters of the adsorbate and adsorbent molecules, n_a is number of molecules of adsorbent and A_a

1. Building a framework for adsorption data processing

and A_A the Lennard-Jones potential constant of the fluid molecule and solid molecule respectively which are defined as

$$A_a = \frac{6mc^2\alpha_a\alpha_A}{\alpha_a/\kappa_a + \alpha_A/\kappa_A} \quad (1.48)$$

and

$$A_a = \frac{3mc^2\alpha_A\kappa_A}{2} \quad (1.49)$$

Here m is the mass of an electron, α_a and α_A are the polarizability of the adsorbate and adsorbate molecule and κ_a and κ_A the magnetic susceptibility of the adsorbate molecule and adsorbent molecule, respectively.

The HK method is applicable to slit pores, and it can be modified to be extended to cylindrical and spherical pores. It is worth noting that there are several assumptions which limit its applicability:

- The HK method is reliant on knowledge of the properties of the surface atoms. This assumption is true only if the material surface is homogenous. Furthermore, longer range interactions with multiple surface layers are not considered.
- Each pore is modelled as uniform and of infinite length. Materials with varying pore shapes or highly interconnected networks may not give realistic results.
- Only dispersive forces are accounted for. If the adsorbate-adsorbent interactions have other specific contributions, the Lennard-Jones potential function will not be an accurate description of pore environment.
- It does not have a description of capillary condensation. This means that the pore size distribution can only be considered accurate up to a maximum of 5 nm.

The pyGAPS framework contains the required physical properties for the most commonly used adsorbates in its database, as well as properties from literature for several materials: the original parameters developed by Horvath and Kawazoe for a carbon surface ⁽²⁵⁾ and the oxide surface parameters published by Saito and Foley.⁽²⁶⁾ The user can provide custom dictionary of these parameters when calling the function as can be seen in the second example in Listing 1.8.

Multiscale computational methods

DFT theory emerged as a rigorous description of molecular adsorption in pores.⁽²⁾ It calculates the properties of the fluid directly from the forces acting between constituent molecules through a statistical mechanical approach. Latter developments, like non-local DFT (NLDFT)⁽³⁾, which makes an account for short range molecule correlation and therefore for the changes in the density profile around the pore walls, and quenched solid

1. Building a framework for adsorption data processing

Listing 1.8: Using the HK method for PSD

```

1 # Calling the HK micropore method with the
2 # Saito-Foley oxide surface parameters
3 result_dict = pygaps.micropore_size_distribution(
4     isotherm,
5     psd_model='HK',
6     adsorbent_model='OxideIon(SF)',
7     verbose=True
8 )
9 # Defining a custom adsorbate parameter dictionary
10 # and using it in the HK method
11 adsorbate_params = {
12     'magnetic_susceptibility': 3.6e-35,
13     'molecular_diameter': 0.3,
14     'polarizability': 1.76e-30,
15     'surface_density': 6.71e+18
16 }
17 result_dict = pygaps.micropore_size_distribution(
18     isotherm,
19     psd_model='HK',
20     adsorbent_model='OxideIon(SF)',
21     adsorbate_model=adsorbate_params,
22     verbose=True
23 )

```

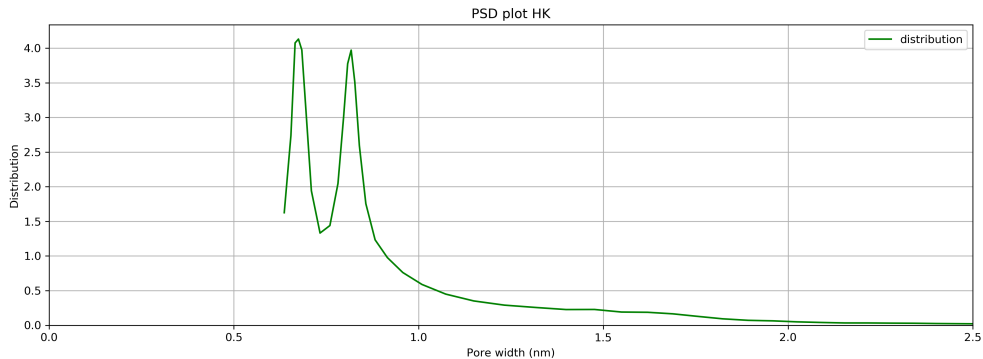


Figure 1.7.: Pore size distribution calculated through the Horvath-Kawazoe method on the UIO-66(Zr) sample

state DFT (QSDFT)⁽²⁷⁾, which allows for heterogeneity of pore walls to be incorporated in the model, have improved the accuracy of the method.

The density functional theory approach can therefore simulate adsorption isotherms on pores of different geometries and sizes. By defining a pore geometry and running the simulation with a range of pore radii, a collection of isotherms is obtained. If an experimental isotherm is through of as a sum of adsorption isotherms in different material pores, then it stands to reason that the preponderence of those pores can be calculated

1. Building a framework for adsorption data processing

through deconvolution.

As the DFT method can model adsorbate condensation behaviour, as well as micropore filling and multilayer adsorption, it can be used for multiscale pore size distribution. The downside is that DFT kernels are temperature, probe, pore-geometry and adsorbent specific and as such are not universally applicable.

The pyGAPS framework can perform isotherm fitting to DFT kernels through the `dft_size_distribution` function. The function takes an `Isotherm` object, then then load the DFT kernel either from disk or from memory and apply a minimization function on the sum of squared differences of the sum of all individual kernel isotherms to generate the contribution of each as per the following equation:

$$f(x) = \sum_{p=p_0}^{p=p_x} \left(n_{p,exp} - \sum_{w=w_0}^{w=w_y} n_{p,kernel} X_w \right)^2 \quad (1.50)$$

The user can specify their own kernel in a CSV format, which will be used for the isotherm fitting. Alternatively, a common DFT kernel is included with the framework, which is applicable on nitrogen adsorption on a carbon slit-like pores in the range of 0.4 nm to 10 nm.

Listing 1.9: DFT size distribution in pyGAPS

```
1 result_dict = pygaps.dft_size_distribution(
2     charact_iso,
3     'internal',
4     verbose=True
5 )
```

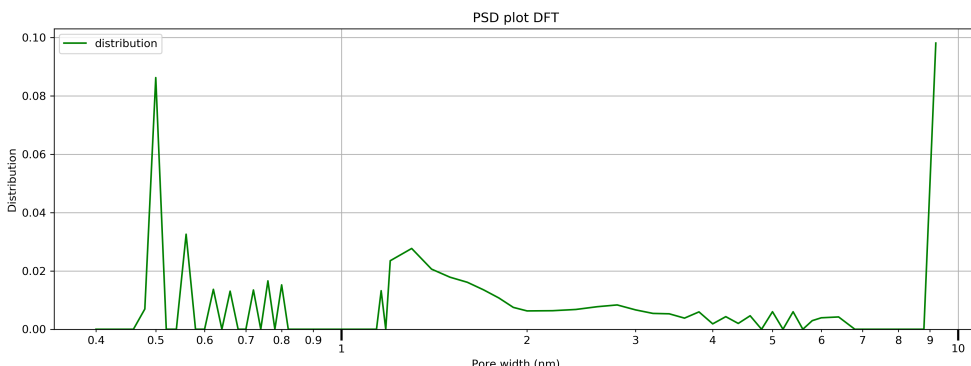


Figure 1.8.: Pore size distribution calculated through the DFT fitting on the Takeda 5A carbon

1.3.4. Predicting multicomponent adsorption

Until now, we have only referred to isotherms pertaining to the adsorption of a single adsorbate. However, besides gas storage, most if not all industrial applications of

1. Building a framework for adsorption data processing

adsorbents involve multiple chemical species undergoing competitive adsorption. Experiments involving several adsorbents are generally difficult and time consuming. There is therefore a requirement to predict such multicomponent systems in order to rapidly screen for potentially interesting separations starting from pure component data.

To this end, the several methods have been devised, with perhaps the most common approach as considering the adsorbed phase as an analogue to a fluid mixture. This method, also known as the ideal adsorbed solution theory (IAST), has been implemented in pyGAPS and will be presented here. Other multicomponent theories such as real adsorbed solution theory (RAST) or the Nitta model exist but usually require more information about specific surface binary activity coefficients to be well suited to a general high throughput approach.

Ideal adsorbed solution theory

The pyGAPS framework includes a modified version of the pyIAST code⁽²⁸⁾ which has been adapted to work with the Isotherm classes. Both model isotherms and real data can be used for IAST, with spreading pressure being calculated through the underlying isotherm model or through interpolation, respectively.

In this case, we fit the experimental data to the available models in pyGAPS which have been presented in subsection 1.3.1, then use the resulting model isotherms for IAST simulations. In order to get a ‘best-fit’ model isotherm, we use the function in Listing 1.10, which fits all available models and selects the one with the lowest residuals between the fitted function and the real data. The isotherms and their best-fitting model is displayed in Figure 1.9a for the CO₂-N₂ pair and in Figure 1.10a for the C₃H₈-C₃H₆ pair.

Listing 1.10: Guessing the best model

```
1 model = pygaps.ModelIsotherm.from_pointisotherm(iso, guess_model=True)

Attempting to model using Henry
Model Henry success, rmse is 7.42
Attempting to model using Jensen-Seaton
Modelling using Jensen-Seaton failed
.....
Best model fit is Quadratic
```

For the carbon dioxide separation, we simulate all equilibrium points for the adsorbed and gaseous phases at different concentrations of the two gases at 1 bar. To do this we use the `pygaps.iast_vle()` function which produces an analogue of a vapour-liquid equilibrium at a specified pressure for a binary mixture. The resulting graph of this function can be seen in Figure 1.10b. As expected, the predicted adsorbed mixture is rich in carbon dioxide. Selectivity can also be calculated in a single point, with the value at 15% CO₂ and 1 bar being 16.5.

For the propane-propylene separation, we simulate the selectivity for propane within a pressure range for a 50% mixture of the two gases. It can be seen that there is little

1. Building a framework for adsorption data processing

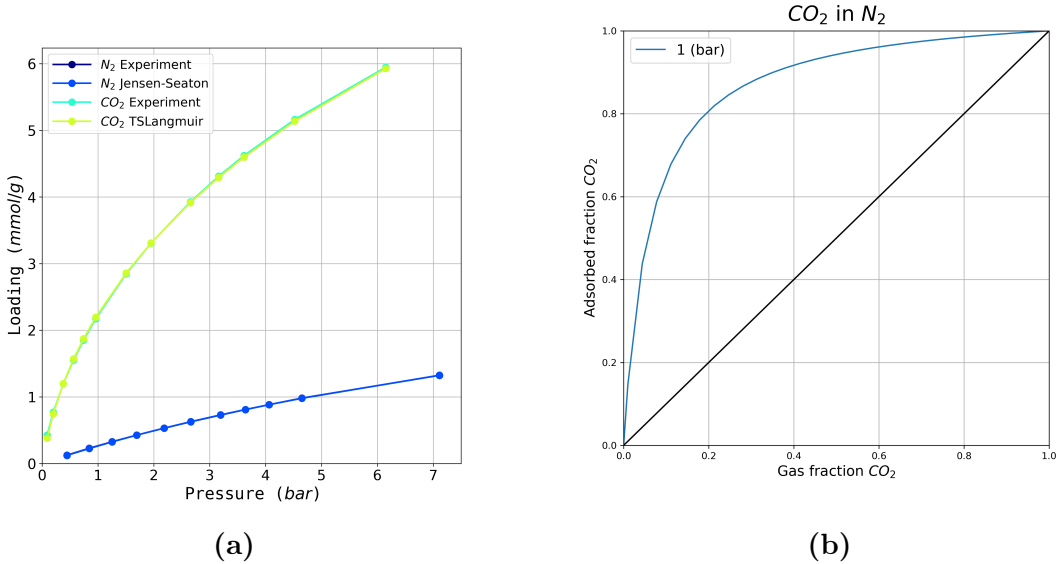


Figure 1.9.: Modelling binary adsorption of CO₂ and N₂: (a) the pure component isotherms and their best fit models and (b) the predicted composition of the gaseous and adsorbed phase for different fractions of CO₂ at 1 bar

or no preference for the unsaturated molecule, though the selectivity increases slightly at pressures above 1 bar.

1.4. Case studies

1.5. Conclusion

BIBLIOGRAPHY

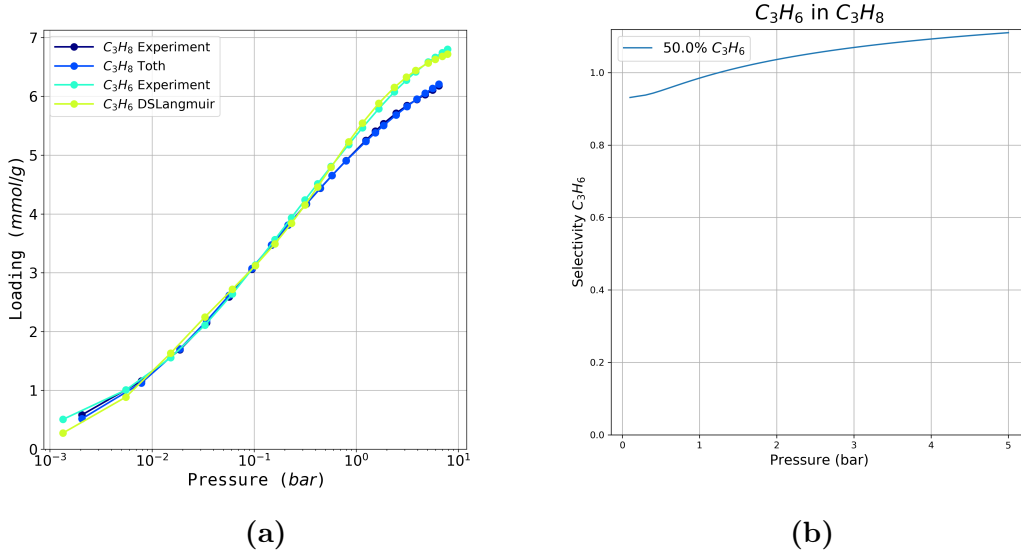


Figure 1.10.: Modelling binary adsorption of a propane-propylene mixture: (a) the pure-component isotherms and their best fit models and (b) the predicted selectivity of propane adsorption of a 50-50% mixture in a range of pressure from 0.1 to 7 bar

Bibliography

- [1] Elliott P. Barrett, Leslie G. Joyner, and Paul P. Halenda. The Determination of Pore Volume and Area Distributions in Porous Substances. I. Computations from Nitrogen Isotherms. *Journal of the American Chemical Society*, 73(1):373–380, January 1951. ISSN 0002-7863. doi: 10.1021/ja01145a126.
- [2] N.A. Seaton, J.P.R.B. Walton, and N. Quirke. A new analysis method for the determination of the pore size distribution of porous carbons from nitrogen adsorption measurements. *Carbon*, 27(6):853–861, 1989. ISSN 00086223. doi: 10.1016/0008-6223(89)90035-3.
- [3] P. Tarazona, U. Marini Bettolo Marconi, and R. Evans. Phase equilibria of fluid interfaces and confined fluids: Non-local versus local density functionals. *Molecular Physics*, 60(3):573–595, February 1987. ISSN 0026-8976, 1362-3028. doi: 10.1080/00268978700100381.
- [4] Dan Siderius, Vincent Shen, and Russell Johnson. NIST / ARPA-E Database of Novel and Emerging Adsorbent Materials, NIST Standard Reference Database 205, 2015.
- [5] Ian H. Bell, Jorrit Wronski, Sylvain Quoilin, and Vincent Lemort. Pure and Pseudo-pure Fluid Thermophysical Property Evaluation and the Open-Source Thermophys-

BIBLIOGRAPHY

- ical Property Library CoolProp. *Industrial & Engineering Chemistry Research*, 53(6):2498–2508, February 2014. ISSN 0888-5885, 1520-5045. doi: 10.1021/ie4033999.
- [6] Eric Lemmon. NIST Reference Fluid Thermodynamic and Transport Properties Database: Version 9.0, NIST Standard Reference Database 23, 1989.
 - [7] Jean Rouquerol, Françoise Rouquerol, Philip L. Llewellyn, Guillaume Maurin, and Kenneth Sing. *Adsorption by Powders and Porous Solids : Principles, Methodology and Applications*. 2013. ISBN 978-0-08-097035-6.
 - [8] Irving Langmuir. The Adsorption of Gases on Plane Surfaces of Glass, Mica and Platinum. *Journal of the American Chemical Society*, 40(9):1361–1403, September 1918. ISSN 0002-7863, 1520-5126. doi: 10.1021/ja02242a004.
 - [9] Stephen Brunauer, P. H. Emmett, and Edward Teller. Adsorption of Gases in Multimolecular Layers. *Journal of the American Chemical Society*, 60(2):309–319, February 1938. ISSN 0002-7863, 1520-5126. doi: 10.1021/ja01269a023.
 - [10] Mikhail Temkin. Kinetics of ammonia synthesis on promoted iron catalyst. *Acta Phys. Chim. USSR*, 12:327–356, 1940.
 - [11] Cory M. Simon, Jihan Kim, Li-Chiang Lin, Richard L. Martin, Maciej Haranczyk, and Berend Smit. Optimizing nanoporous materials for gas storage. *Physical Chemistry Chemical Physics*, 16(12):5499, 2014. ISSN 1463-9076, 1463-9084. doi: 10.1039/c3cp55039g.
 - [12] C. R. C. Jensen and N. A. Seaton. An isotherm equation for adsorption to high pressures in microporous adsorbents. *Langmuir*, 12(11):2866–2867, 1996.
 - [13] Terrell L. Hill. *An Introduction to Statistical Thermodynamics*. Dover Publications, New York, 1986. ISBN 978-0-486-65242-9.
 - [14] Alan L. Myers. Thermodynamics of adsorption in porous materials. *AIChE Journal*, 48(1):145–160, January 2002. ISSN 00011541. doi: 10.1002/aic.690480115.
 - [15] Solot Suwanayuen and Ronald P. Danner. A gas adsorption isotherm equation based on vacancy solution theory. *AIChE Journal*, 26(1):68–76, January 1980. ISSN 00011541. doi: 10.1002/aic.690260112.
 - [16] T. W. Cochran, R. L. Kabel, and R. P. Danner. Vacancy solution theory of adsorption using Flory-Huggins activity coefficient equations. *AIChE Journal*, 31(2):268–277, February 1985. ISSN 0001-1541, 1547-5905. doi: 10.1002/aic.690310214.
 - [17] Matthias Thommes, Katsumi Kaneko, Alexander V. Neimark, James P. Olivier, Francisco Rodriguez-Reinoso, Jean Rouquerol, and Kenneth S W Sing. Physisorption of gases, with special reference to the evaluation of surface area and pore size distribution (IUPAC Technical Report). *Pure and Applied Chemistry*, 87(9-10):1051–1069, 2015. ISSN 13653075. doi: 10.1515/pac-2014-1117.

BIBLIOGRAPHY

- [18] George Halsey. Physical Adsorption on Non-Uniform Surfaces. *The Journal of Chemical Physics*, 16(10):931–937, October 1948. ISSN 0021-9606, 1089-7690. doi: 10.1063/1.1746689.
- [19] William D. Harkins and George Jura. Surfaces of Solids. XIII. A Vapor Adsorption Method for the Determination of the Area of a Solid without the Assumption of a Molecular Area, and the Areas Occupied by Nitrogen and Other Molecules on the Surface of a Solid. *Journal of the American Chemical Society*, 66(8):1366–1373, August 1944. ISSN 0002-7863, 1520-5126. doi: 10.1021/ja01236a048.
- [20] B Lippens. Studies on pore systems in catalysts V. The t method. *Journal of Catalysis*, 4(3):319–323, June 1965. ISSN 00219517. doi: 10.1016/0021-9517(65)90307-6.
- [21] D. Atkinson, A.I. McLeod, and K. S. W. Sing. Adsorptive properties of microporous carbons: Primary and secondary micropore filling. *Journal de Chimie Physique*, 81: 791–794, 1984. ISSN 0021-7689. doi: 10.1051/jcp/1984810791.
- [22] Jean Rouquerol, Gino V. Baron, Renaud Denoyel, Herbert Giesche, Johan Groen, Peter Klobes, Pierre Levitz, Alexander V. Neimark, Sean Rigby, Romas Skudas, Kenneth Sing, Matthias Thommes, and Klaus Unger. The characterization of macroporous solids: An overview of the methodology. *Microporous and Mesoporous Materials*, 154:2–6, May 2012. ISSN 13871811. doi: 10.1016/j.micromeso.2011.09.031.
- [23] Duong D Do. *Adsorption Analysis: Equilibria and Kinetics: (With CD Containing Computer Matlab Programs)*, volume 2 of *Series on Chemical Engineering*. Imperial College Press, September 1998. ISBN 978-1-86094-130-6 978-1-78326-224-3. doi: 10.1142/p111.
- [24] D. Dollimore and G.R R. Heal. Pore-size distribution in typical adsorbent systems. *Journal of Colloid and Interface Science*, 33(4):508–519, August 1970. ISSN 00219797. doi: 10.1016/0021-9797(70)90002-0.
- [25] Geza Horvath and Kunitaro Kawazoe. Method for the calculation of effective pore size distribution in molecular sieve carbon. *Journal of Chemical Engineering of Japan*, 16(6):470–475, 1983. ISSN 1881-1299. doi: 10.1252/jcej.16.470.
- [26] A. Saito and H. C. Foley. Curvature and parametric sensitivity in models for adsorption in micropores. *AICHE Journal*, 37(3):429–436, March 1991. ISSN 0001-1541. doi: 10.1002/aic.690370312.
- [27] Alexander V. Neimark, Yangzheng Lin, Peter I. Ravikovich, and Matthias Thommes. Quenched solid density functional theory and pore size analysis of micro-mesoporous carbons. *Carbon*, 47(7):1617–1628, June 2009. ISSN 00086223. doi: 10.1016/j.carbon.2009.01.050.

BIBLIOGRAPHY

- [28] Cory M. Simon, Berend Smit, and Maciej Haranczyk. PyIAST: Ideal adsorbed solution theory (IAST) Python package. *Computer Physics Communications*, 200: 364–380, 2016. ISSN 00104655. doi: 10.1016/j.cpc.2015.11.016.

2. Extending bulk analysis of porous compounds through calorimetry

2.1. Introduction

2.2. Literature

Isosteric heat

The isosteric heats are calculated from experimental data using the Clausius-Clapeyron equation as the starting point:

$$\left(\frac{\partial \ln P}{\partial T}\right)_{n_a} = -\frac{\Delta H_{ads}}{RT^2} \quad (2.1)$$

Where ΔH_{ads} is the enthalpy of adsorption. In order to approximate the partial differential, two or more isotherms are measured at different temperatures. The assumption made is that the heat of adsorption does not vary in the temperature range chosen. Therefore, the isosteric heat of adsorption can be calculated by using the pressures at which the loading is identical using the following equation for each point:

$$\Delta H_{ads} = -R \frac{\partial \ln P}{\partial 1/T} \quad (2.2)$$

and plotting the values of $\ln P$ against $1/T$ we should obtain a straight line with a slope of $-\Delta H_{ads}/R$.

The isosteric heat is sensitive to the differences in pressure between the two isotherms. If the isotherms measured are too close together, the error margin will increase. The method also assumes that enthalpy of adsorption does not vary with temperature. If the variation is large for the system in question, the isosteric heat calculation will give unrealistic values.

Even with carefully measured experimental data, there are two assumptions used in deriving the Clausius-Clapeyron equation: an ideal bulk gas phase and a negligible adsorbed phase molar volume. These have a significant effect on the calculated isosteric heats of adsorption, especially at high relative pressures and for heavy adsorbates.

2.3. Method

Gas adsorption isotherms and enthalpies were measured experimentally using a Tian-Calvet type microcalorimeter coupled with a home-made manometric gas dosing system.⁽¹⁾ This apparatus allows the simultaneous measurement of the adsorption isotherm and the corresponding differential enthalpies. Gas is introduced into the system using a step-by-step method and each dose is allowed to stabilize in a reference volume before being brought into contact with the adsorbent located in the microcalorimeter. The introduction of the adsorbate to the sample is accompanied by an exothermic thermal signal, measured by the thermopiles of the microcalorimeter. The peak in the calorimetric signal is integrated over time to give the total energy released during this adsorption step. At low coverage the error in the signal can be estimated to around $\pm 0.2 \text{ kJ mol}^{-1}$. Around 0.4 g of sample is used in each experiment. For each injection of gas, equilibrium was assumed to have been reached after 90 minutes. This was confirmed by the return of the calorimetric signal to its baseline ($< 5 \mu\text{W}$). The gases used for the adsorption were obtained from Air Liquide and were of minimum N47 quality (99.997 % purity).

2.4. Results and discussion

2.4.1. Routine characterization of a MOF sample

When a newly synthesised sample is available, an initial characterisation is often performed to compare the material with previous batches. Adsorption of nitrogen at 77 K is commonly used to verify if predictors such as specific surface area and pore size distribution are consistent with other samples or literature values.

The nitrogen isotherm is first imported in pyGAPS. To obtain the BET area, the `pygaps.area_BET()` method is used with the isotherm object as the parameter and the verbose option, with Figure ?? as the output. It can be seen that the framework has automatically selected the points within the applicable BET region using the checks devised by Rouquerol et al.^(?) to assert method validity. The statistical BET monolayer point is within the selected region, which is one of the checks implemented for method validity. The calculated surface area is $1277 \text{ m}^2/\text{g}$, which is similar to literature values.^(?)

The same isotherm is used to calculate the pore size distribution of the UiO-66(Zr) sample. This MOF has octahedral cages surrounded by eight corner tetrahedral cages of 11 and 8 Å respectively. The structure is therefore expected to have only micropores. Two methods are available in pyGAPS for micropore size distributions: a ‘classical’ Horvath-Kawazoe (HK) method^(?), as well as a DFT fitting routine. The HK method is called by using the function in Listing ???. Here, the surface characteristic parameters determined by Saito and Foley^(?) are to be used, with the framework automatically supplying the parameters for the adsorbed gas.

The DFT fitting is done using the internal kernel which is applicable for N_2 on carbon slit pores and included with pyGAPS. Results are shown in Figure ???. We can see

2. Extending bulk analysis of porous compounds through calorimetry

that whilst both methods produce a bimodal size distribution, neither is accurate in describing the crystallographic pore widths. This is to be expected, since neither method is applicable to the UiO-66(Zr) system. However, when comparing two samples of the same MOF, these methods can still highlight differences in the quality of the two batches. For example, it can be seen that the DFT method shows wide peaks at >1 nm which can be an indication of the presence of defects in the UiO-66(Zr) structure. Indeed, TGA analysis of the pristine sample shows a linker ratio (11.8 linkers per cluster) that is lower than it would be in a perfect sample (see figure in supplemental information.)

New materials are often screened for their ability to act as a CO_2 capture material. A good predictor of performance in this application are the enthalpies of adsorption, which are an indication of host-guest interactions. Here, we first measure the differential heats of adsorption directly through the use of adsorption microcalorimetry at 303 K. Then, to determine the isosteric heats of adsorption, two isotherms have been measured at 303 K and 323 K respectively. The complete set of isotherms is loaded into pyGAPS and plotted by the `pygaps.plot_iso()` function as seen in Figure 2.1a. To calculate the isosteric heat of adsorption, the two isotherms measured for this purpose are passed through the `pygaps.isosteric_heat()` function. The results from the calculation are overlaid on top of the measured calorimetric data in Figure 2.1b. The two datasets are overlap for the most part but diverge at low loadings and near complete coverage. At low loading the small changes in pressure amount introduce large errors in the Clausius-Clapeyron equation. This, together with the breakdown of the assumption of equilibrium due to active sites in the MOF lead to the calorimetric measurement providing more valid results. At higher loadings, where the isotherm reaches a plateau and the change in adsorbed amount is small from point to point, errors are introduced in the direct calculation of the heat of adsorption. The two techniques are thus complementary.

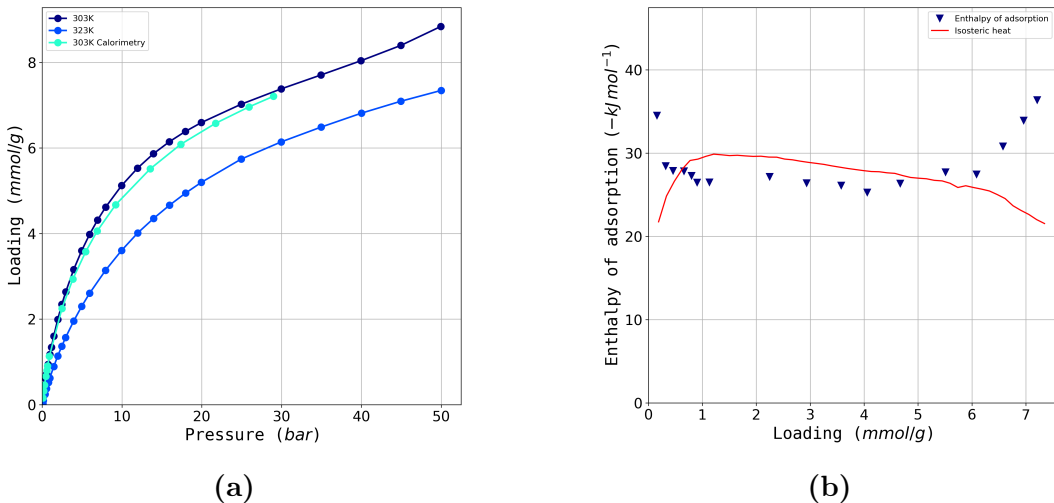


Figure 2.1.: Calculation of enthalpy of adsorption: (a) the dataset of isotherms used and (b) the calculated isosteric heat (red line) together with the measured differential enthalpy of adsorption (blue triangles)

2.4.2. Analysis of a carbon sample for gas separation applications

A sample of reference carbon Takeda 5A is to be investigated for an in-depth characterisation of the adsorption behaviour of pure gases, with a focus on describing the pore environment. Afterwards, the performance of different binary separations is evaluated, such as CO₂/N₂ and propane/propylene.

Pure gas adsorption data has been recorded at 303 K in conjunction with microcalorimetry on N₂, CO, CO₂, CH₄, C₂H₆, C₃H₆ and C₃H₈. The complete dataset is plotted with the pygaps.plot_iso() function and can be seen in Figure 2.2a.

Nitrogen and carbon monoxide are similar in their adsorption behaviour, with a nearly linear isotherm and low capacities. Hydrocarbons are adsorbed with higher loadings, with both propane and propylene reaching a plateau at low pressures. Propylene is seen to have a higher capacity than propane, with packing effects as a likely cause. Carbon dioxide has the highest loading capacity of the entire dataset.

Two parameters can be useful in characterising the local pore environment before guest-guest interactions come into effect: the Henry constant at low loadings as well as the initial enthalpy of adsorption. Both can be calculated with pyGAPS, with several options in regard to the methodology. Here, Henry's constant is calculated using the pygaps.initial_henry_virial() function, which fits a virial model to the isotherm and then takes the limit at loading approaching zero. The initial enthalpy of adsorption is obtained through the pygaps.initial_enthalpy_comp() function. This fits the enthalpy curve to a compound contribution from guest-host interaction, defects, guest-guest attraction and repulsion using a minimization algorithm. The results of the calculations are plotted versus the polarizability of the gas used, which can be obtained from the respective `Adsorbate` class. Figure 2.2b shows that both the parameters fall on a linear trend, which suggests that the interactions between those guests and the pore walls are mostly due to Lennard-Jones interactions. Carbon dioxide has a higher enthalpy of adsorption than the baseline due to the contribution from its quadrupole moment. There is almost a complete overlap between propane and propylene, which leads to the conclusion that the unsaturated double bond does not interact in a specific way with the carbon surface. The difference between the two isotherms is due exclusively to steric and packing effects.

2.5. Conclusion

BIBLIOGRAPHY

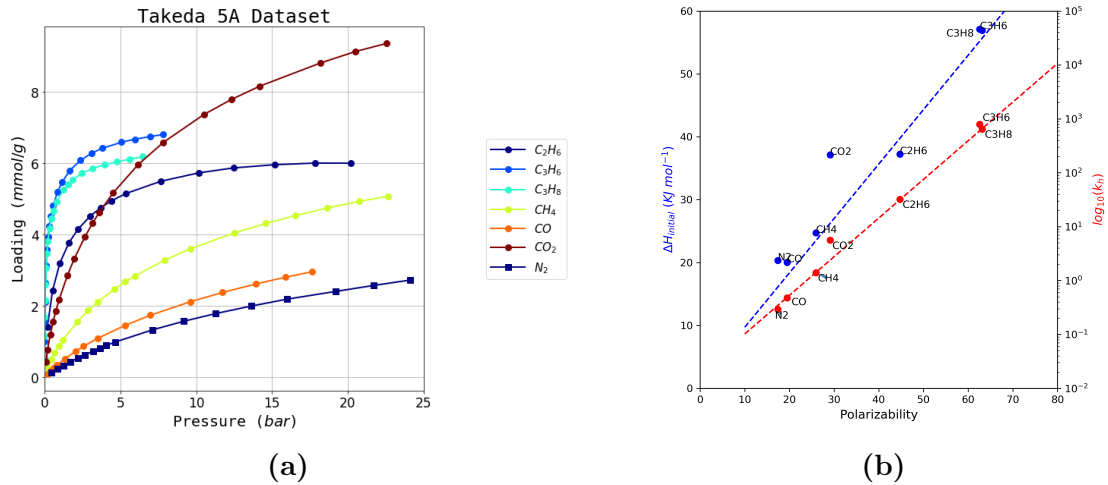


Figure 2.2.: Takeda 5A dataset processing: (a) the experimental dataset all recorded gases and (b) the calculated trends of initial heat of adsorption and Henry's constant

Bibliography

- [1] Philip L. Llewellyn and Guillaume Maurin. Gas adsorption microcalorimetry and modelling to characterise zeolites and related materials. *Comptes Rendus Chimie*, 8 (3-4):283–302, March 2005. ISSN 16310748. doi: 10.1016/j.crci.2004.11.004.

3. Exploring the impact of synthesis and defects on adsorption measurements

3.1. Introduction

Ideality is a rarely encountered phenomenon in nature. In fact, experience has shown that deliberate and concerted efforts must be made in order to obtain states of matter that have all the properties described by an “ideal state”. Often the divergence is small and can be approximated away, as is the case when using the ideal equation of state for noble gasses or ascribing the thermal radiation emitted by an object to a black-body spectrum. It is, however, in non-ideality where the fascinating complexity of the world asserts itself and where advances in our understanding can be made.

When considering crystals, the ideal description of an infinite periodic repetition of building blocks in three dimensional space is not applicable in the real world. From the necessary existence of crystal boundaries to the possible presence of other structural irregularities, these so called crystal “defects” can have varying effects on the bulk properties of the material. Their presence is not necessarily a fault as they often impart the material with beneficial characteristics on multiple length scales. An understanding of the interplay of defects in the lattices of alloys is an art in itself. Crystal grain size and presence of additives such as carbon and nickel can completely change the hardness, ductility, tensile strength and corrosion resistance of steel.⁽¹⁾ Various other forms of disorder can introduce completely new behaviours altogether. The insertion of foreign elements into the crystal structure of semiconductor materials such as silicon can alter its electronic properties and is responsible for the ubiquitousness of computing devices based on the transistor.⁽²⁾ This application of defects can be said to have ushered in the modern digital age, just as the creation of steel led to the industrial revolution. Other such emergent properties exist such as high temperature superconductivity⁽³⁾ or thermoelectric behaviour⁽⁴⁾ which are influenced by defect-related spin effects or defect-mediated charge transfer. As such, the kind of heterogeneity afforded by defects is a key attribute in condensed matter physics and a target for material design. The scientific foray in their control, either through generation or by inhibition can be termed “defect engineering”.

As porous coordination polymers (PCPs) and their subclasses metal organic frameworks (MOFs) and covalent organic frameworks (COFs) became prominent topics of study in the field of porous materials, the presence and desirability of defects in their

3. Exploring the impact of synthesis and defects on adsorption measurements

ordered crystal structures has been put into question. Investigation of the propensity of these compounds to form defects has suggested potential benefits in the fields of catalysis⁽⁵⁾, gas storage and separation⁽⁶⁻⁸⁾, and has even alluded to applications in sensing and optoelectronics.⁽⁹⁾ Furthermore, MOFs such as UiO-66 and similar oxo-Zr coordination compounds have been shown to have intrinsically defective structures, where clustering and correlation of defects is in fact inevitable.⁽¹⁰⁾ The engineering of defects in PCPs is currently the focus of many initiatives as it is seen as a highly desirable method of tuning their properties through judicious design.^(5,11,12)

From the point of view of describing adsorption in such materials, the presence of defects introduces a conundrum. If a MOF can be defective, and is often intrinsically so, a slight change in synthesis conditions can introduce a large variability in its properties, and obtaining a “standard” isotherm may be a challenge. A large scale meta analysis of the correlation between material structure and its adsorption performance cannot be achieved unless the contribution of defects is assessed for each material.

Chapter summary

In this chapter we explore the kind of changes in adsorption behaviour introduced through defect engineering with the high throughput processing tools presented in chapter 1. First, the range of crystal defects that can be found in MOFs is presented. A summary of the known methods for controlling defects in such materials is discussed, as well as the known impact on different properties. Particular focus is placed on the zirconium variant of UiO-66, due to its aforementioned remarkable stability to the presence of defects. An alternative approach to defect generation in this MOF is explored, through induced leaching of linkers in a solvent solution of monotopic acids which have been shown to induce defect formation when present during synthesis. The influence on defect type and preponderence of the acid, its concentration and the solvent itself is investigated, through the changes in adsorption behaviour.

Contributions

This work was done in collaboration with the DEFNET project partner at the Centre for Surface Chemistry and Catalysis in KU Leuven. The study was designed by Paul Iacomi and João Marreiros during the secondment undertaken in COK as part of this project. Two PWI master students, Giel Arnauts and Wouter Arts helped with the synthesis, leaching and characterisation of the first trial batch. João Marreiros conducted the synthesis, leaching, XRD and NMR of further batches in Leuven. Paul Iacomi performed characterisation through TGA and all physisorption measurements in Marseille. Prof. Philip Llewellyn and Prof. Rob Ameloot provided critical input in the direction of the study and the significance of the results.

3.2. The defective nature of MOFs

3.2.1. Types of crystal defects and their analogues in MOFs

From a crystallographic point of view, defects can be described as features which suspend the order of components in an ideally regular lattice. The building blocks in the case of MOFs can be either individual atoms, molecules or other higher order structural building units (SBUs). Any change with leads to local breaking of symmetry with respect to the original structure can be viewed as a defect.

With respect to dimensionality, defects can be described as point defects, line defects (such as edge dislocations), plane defects (such as grain boundaries or stacking faults) and bulk defects (macroscopic voids, phase coexistence). When it comes to point defects, we can broadly refer to several types: **substitutional defects**, where an existing building unit is replaced or transformed into another, **inclusion** or **interstitial defects**, where a foreign component or building block is included in the framework and **vacancy defects** where one of the lattice sites is unoccupied. In the context of MOFs, the same general categories of defects apply. However, due to the higher degrees of freedom available in these compounds, a greater variety of potential crystal defects can exist.

Vacancy defects are encountered through missing linker and missing cluster defects. These analogues of Schottky defects arise from the removal of one or several topological nodes or vertices. In most cases, the charge neutrality of the framework is maintained through coordination of available counterions or solvent molecules, though changes in the oxidation state of the metal atoms may also occur.

Substitution point defects are also highly common in MOFs, as the usual requirement for framework connectivity is the existence of “click groups” on metal nodes and linkers. Any piece which fulfils the connectivity and size requirements may be used, a property which has been exploited in the topological approach to creating new MOFs.^(13–15) It also allows for MOFs in which nodes or vertices are only partly replaced with analogues to be created. This strategy has been successfully employed to create mixed-linker or mixed-metal structures.^(16,17) It should be noted that if the distribution of the substitutions takes a homogenous pattern throughout the lattice, the structure no longer falls under the definition of a defect.

A special case of substitutional defects which are present in MOFs are mixed valence defects. When metals with multiple stable oxidation states, such as Cu (I–II), Fe (II–III) etc. are part of the framework, a change in their oxidation state can occur. This has been shown to be an integral part of copper paddlewheel and iron trimesate containing MOFs⁽¹⁸⁾ and can even be seen with the naked eye, as such defects have been shown to give HKUST-1 its common blue colour.⁽¹⁹⁾

Inclusion-type point defects are loosely applied to MOFs. As the definition describes an interstitial defect to be an atom occupying an usually vacant space, all foreign bodies occupying the available porosity of the MOF, including aforementioned counterions and solvents could be considered as defects in the traditional crystallographic sense. Introduction of nanoparticles such as metals or metal oxides inside the pores is a more

3. Exploring the impact of synthesis and defects on adsorption measurements

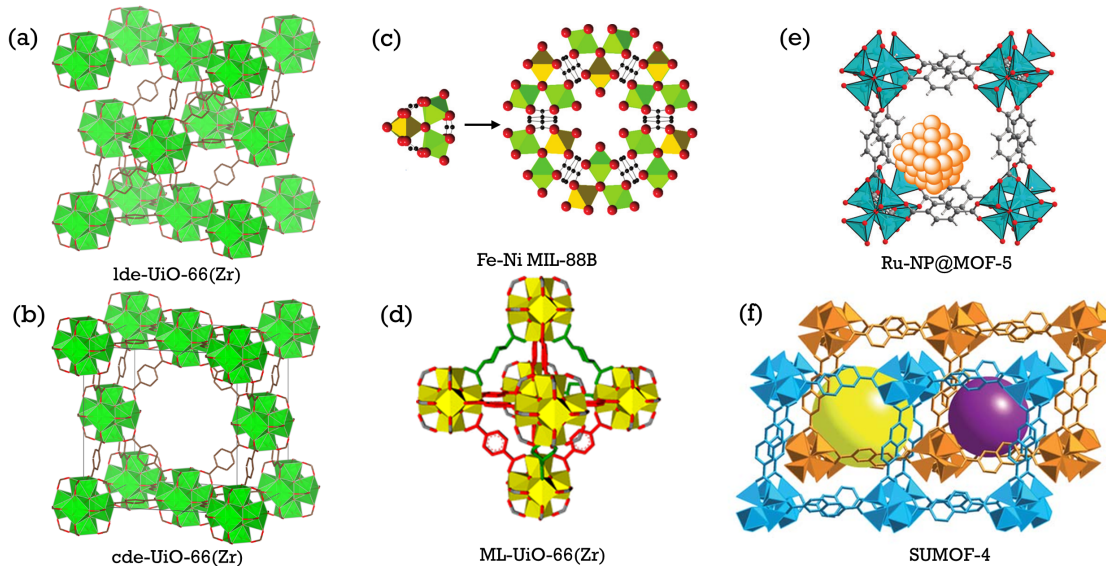


Figure 3.1.: Different types of defects as seen in MOFs: vacancy defects in the form of (a) missing linker and (b) missing cluster substitutional defects such as (c) mixed linker⁽¹⁶⁾ and (d) mixed metal⁽²²⁾ MOFs or defects as created through (e) nanoparticles⁽²¹⁾ or (f) interpenetration⁽²³⁾

traditional view of such defects. It has been shown to have beneficial effects in catalytical applications.^(20,21)

A common feature of structured high porosity compounds is interpenetration. While not a defect in the classical sense, it has important effects on their properties.⁽²⁴⁾ With a large enough pore size, a secondary lattice can form in the pore voids of the primary one. This imposes a limit on the common design strategy of isoreticular synthesis, but can introduce new features such as better adsorption through confinement, increase in active site count and even flexibility.

Finally, the surface of the MOF can also be regarded as a boundary or plane defect. The nature of the surface plays a role in intra-particle interactions, important when considering the agglomeration behaviour or inclusion of crystals in a membrane.⁽²⁵⁾ The surface properties play a crucial role in MOFs which are synthesised as thin films^(26,27), where the nearly 2D materials are better defined by interfacial characteristics than through bulk properties. Crystal size effects on MOF properties such as flexibility can also be through of as a consequence of surface characteristics, more specifically of surface-to-volume ratio. When considering such soft materials^(28,29), it has been shown that the flexible behaviour is highly influenced by entropy barriers introduced by the surface.

3. Exploring the impact of synthesis and defects on adsorption measurements

3.2.2. Consequences of defects

The introduction of defects in the regular crystal lattice of metal organic frameworks can have a dramatic impact on their properties. In general, the following may occur:

- the porosity of the structured is altered, increasing in the case of vacancy defects and decreasing when bulky substitutions or inclusions are made;
- interactions with adsorbed molecules change, through the different pore environment encountered or through the generation of coordinatively unsaturated sites (CUS);
- the stability of the resulting structure is lower than that of the parent MOF, influencing bulk mechanical and thermal properties.
- electronic properties can be changed which may affect the optical electric or magnetic behaviour of the material.

From a purely geometric point of view, the introduction of missing linker or missing cluster defects leads to more voids in the structure, increasing its porosity. It often results in a larger specific surface area and pore volume and thus useful for applications such as gas storage which depend only on the available surface or capacity. Macro-scale void networks can also be desirable, as the better developed pore network has a large impact on the transport properties of the compound, increasing diffusion rates.

The inclusion of defects also changes the landscape of the pore walls leading to different interactions with adsorbed molecules. Charge balancing counterions, molecules capping defect sites, functionalizations of substituted linkers or CUS can change the chemistry of the pore, with specific interactions towards certain adsorbates.⁽³⁰⁾ For example, adsorption of water on oxo-Zr MOFs, has been seen to be dominated by the percentage of defects. The pore filling step can shift from high partial pressure ($0.6\ p/p_0$) to much lower pressures as seen in UiO-66⁽⁷⁾ and MOF-801.⁽⁶⁾ Defect site adsorbed molecules can also lead to cooperative phenomena, such as the beneficial effect of defect-adsorbed water on the catalysis of Fischer esterification.⁽³¹⁾ or the CO₂ capture on amine-grafted metal centers.⁽³²⁾ Another example can be seen in MOFs containing Fe trimers, such as MIL-127(Fe) or MIL-100(Fe) where heating or acid treatment can induce a reduction of one of the iron atoms, generating additional Lewis sites for catalysis⁽¹⁸⁾ or providing CUS for cooperative binding of carbon monoxide through a spin transition mechanism.⁽³³⁾

Of course, defects are also problematic. Most metal organic frameworks synthesised to date suffer from poor stability. Even if the material is crystalline when solvated, the framework may not have enough structural stability to be able to sustain itself when fully evacuated. The activation process itself can lead to framework collapse, due to the forces encountered in guest removal, necessitating complex activation processes, such as supercritical drying or preliminary solvent exchange. After activation, the metal-ligand bond is susceptible to attack by adsorbed species. Here, defects in the framework have been shown to play a major role in its stability (or lack thereof).⁽³⁴⁾ Copper paddlewheel containing structures are particularly vulnerable to such attack.⁽³⁵⁾

3. Exploring the impact of synthesis and defects on adsorption measurements

Finally, several completely different phenomena may emerge through the introduction of defects. Optical properties such as colour centers and induced luminescence⁽¹⁹⁾, changes in thermal conductivity or induced magnetic properties such as ferromagnetism⁽³⁶⁾ have been shown to be a consequence of the presence of defects.

3.2.3. Defect engineering of MOFs

Since defects introduce another degree of freedom for controlling the properties of metal organic frameworks, the study of their formation can lead to new methods of tuning a material towards a desired application. There are two major pathways of introducing defects, through control of the structure during synthesis or through post-synthetic methods.⁽³⁷⁾

For defect generation during synthesis, the so called “solid solution” approach is to mix several types of building blocks together, be it multiple linkers or metallic nodes. Mixing functionalised versions of linkers leads to the creation of partly-substituted MOFs. Mixed valency frameworks can also be synthesised through this method, as can be seen in the replacement of up to 32% of the linker in the framework in the ruthenium HKUST-1 analogue with a defect-generating linker.⁽³⁸⁾ The commonly used method of improving crystallinity and particle size of modulator-assisted synthesis⁽³⁹⁾ has been shown by Shearer et al. to be a reliable method of introducing defects.⁽⁴⁰⁾ The modulators act as capping agents and occupy metal coordination sites.

Post-synthetic methods are also widely employed for defect generation. Through acid treatment of the previously mentioned MIL-100(Fe), cleavage of one of the Fe–O bonds can be induced, with a protonation of the carboxylic linker and the generation of a CUS.⁽⁴¹⁾ Thermal treatment can achieve the same results, with weakly coordinated molecules removed to expose metal CUS or even *in situ* linker decomposition.⁽⁴²⁾ Ligand exchange has also been shown to be achievable post-synthetically,⁽⁴³⁾ through the replacement of existing linkers, capping agents or even induce structural “healing”. Finally, the linkers are still available for organic reactions which can transform a part of them into functionalised versions, as seen in the nitration of the terephthalate linker in MIL-101.⁽⁴⁴⁾

3.2.4. The propensity of UiO-66(Zr) for defect generation

The UiO-66(Zr) MOF and its derivatives are well known due to their thermal and chemical stability.⁽⁴⁵⁾ It is composed of $[Zr_6O_4(OH)_4]^{12+}$ clusters (seen in Figure 3.2a) which are connected with benzene dicarboxilate (BDC) linkers to form a face-centered cubic framework. Due to its exceptional stability among MOFs, it has been the focus of much research, where it has shown promise⁽⁴⁶⁾ in use for gas adsorption and catalytic applications.

The synthesis of many functional derivatives of UiO-66, through the use of different struts of nodes has been a stepping stone towards obtaining mixed-linker and mixed-metal materials, either thorough the solid solution or post-synthesis modification approach.⁽⁴⁷⁾ It has also been used as a support for nanoparticles, such as palladium⁽⁴⁸⁾ or

3. Exploring the impact of synthesis and defects on adsorption measurements

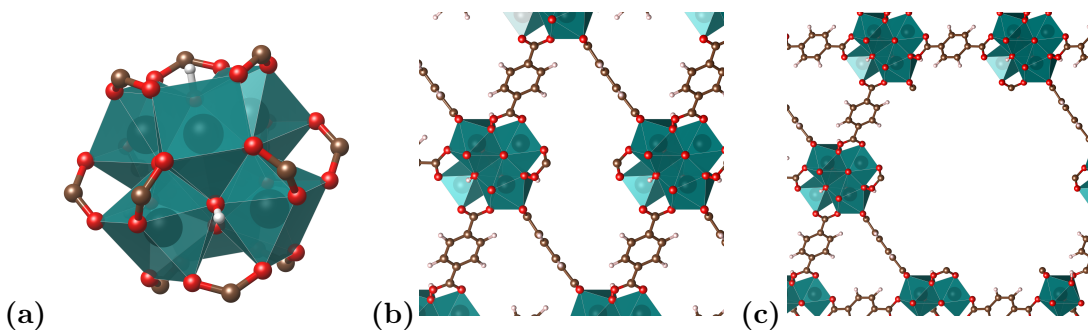


Figure 3.2.: (a) The 12-coordinated Zr cluster in UiO-66(Zr) which connects with benzene dicarboxilate (BDC) linkers. Two prototypical defect types are shown (b) a missing linker defect and (c) a missing cluster defect. Zirconium octahedra are represented in turquoise, oxygen in red, carbon in brown and hydrogen in white.

platinum.⁽⁴⁹⁾

However, UiO-66 is particularly adept in its ability to support vacancy defects. Due to the stability of the metal-oxygen bond, and the high linker to metal ratio, the UiO family of MOFs can tolerate a high defectivity in their structure, which manifests through either missing linker (Figure 3.2b) or missing cluster (Figure 3.2c) defects. Ever since the discovery of a number of defects in the pristine material through neutron powder diffraction methods⁽⁵⁰⁾ and the theoretical basis laid down by Cliffe et al. for the existence of correlated defective nanodomains where the existence of a vacancy induces defect formation in neighbouring sites , this MOF became a prototypical framework for the study of such defects. The modulated synthesis approach, initially used as a means of creating novel topologies and controlling crystal size⁽⁵¹⁾ has been remarkably successful in obtaining defective versions of UiO-66(Zr).⁽⁴⁰⁾ Post-synthetic methods such as ligand exchange⁽⁴³⁾, temperature-induced dehydroxilation of the zirconium cluster⁽⁵²⁾ and thermal removal of one of the linkers in a mixed-linker variant⁽¹⁶⁾ have been similarly adept in obtaining voids in the structure. More recently, the interplay between the defective nature of UiO-66 and the mechanism of post-synthesis linker exchange⁽⁵³⁾ has been put into the limelight.

In these defects, the metal sites are almost always capped, with monoacids such as formate and acetate, water, hydroxyl groups or other counterions being able to assume the role of capping agent. It has been shown by Thornton et al. that the influence of such defects on the adsorption properties depend not only on their position, but also on these capping agents.⁽⁵⁴⁾

Such vacancy defects prove to be useful for generating Lewis sites for catalytic application, as can be seen in the 4-fold increase in conversion in citronellar cyclization or the increase in 4-tert-butylcyclohexanone reduction from 5–7% to almost 90%.⁽⁵⁵⁾ They are also useful for gas separation, as they can increase the interaction towards a component of the mixture, seen for example on the increased efficiency of CO₂ / N₂ separation.⁽⁵⁴⁾

It can therefore be concluded that vacancy defects are a fundamental characteristic

3. Exploring the impact of synthesis and defects on adsorption measurements

of this MOF, with wide-ranging effects in its properties. As such, it is desirable to have methods to generate and control them. In the following pages, we examine a tertiary method for vacancy defect generation: leaching in solvent solution, a method which has been previously shown to be applicable to other MOFs.⁽⁵⁶⁾

3.3. Materials and methods

3.3.1. Materials

The UiO-66(Zr) MOF used in this study was synthesised according to the procedure described in section B.4, which was adapted from Shearer et al.⁽⁵⁷⁾ This particular method was chosen to ensure that a structure with a minimal number of intrinsic defects would be obtained.

The resulting parent MOF was activated for 8 h at 200 °C to ensure that all solvent was removed. 200 mg aliquots of material were prepared and placed in vials, alongside the monotopic acid dissolved in 20 ml of the respective solvent. The quantities of acid correspond to molar quantities of the framework. The samples were then gestated over a 24 h period at 80 °C in a temperature controlled oven. Pressure resistant Schott sealed bottles were used to ensure that solvents with a lower boiling point do not evaporate. After leaching, samples were collected and washed in ethanol for 4 h, a procedure repeated 4 times. Finally, all samples were dried at 120 °C.

To generate a comprehensive map of the influence of different variables on defect concentration, a number of leaching conditions have been selected. The same monotopic acids which have been successfully used as modulators in the synthesis of defective UiO-66 (formic acid (FA), acetic acid (AA), trifluoroacetic acid (TFA) and benzoic acid (BA)) were used in various concentration ranges, from 1 to 100 molar equivalents with respect to the framework. In order to verify the contribution of the solvent N,N'-dimethylformamide (DMF), deionized water, ethanol and dimethyl sulfoxide (DMSO) were used as the leaching medium. Two parent materials have been synthesised, PWI-C which formed the basis of the initial DMF test trial, and JM237 which was made in bulk to be used for subsequent solvent batches. The DMF dataset does not include any trifluoroacetic acid leached samples, as it was only used in the latter sample sets. Furthermore, no benzoic acid samples could be generated when using water as a solvent, due to its poor capability of dissolving the in significant amounts. Finally, at high acid concentrations, several of the samples were completely dissolved at leaching conditions. The mass loss during leaching was found to be between 10 and 60%, depending on the acid and solvent used. When using 10 equivalents of TFA in DMSO, only 18% of the original sample could be recovered. A summary of all generated materials can be found in Table 3.1. Some properties of the acids and solvents used, such as acidity, solubility, etc. are found in Table D.2 and Table D.1 in Appendix D respectively.

3. Exploring the impact of synthesis and defects on adsorption measurements

Table 3.1.: Samples used in the UiO-66(Zr) linker leaching study

Sample name	Solvent	Modulator	Concentration	Observations
PWI-C	None	None	None	Parent material
FA1	DMF	FA	1:1	—
FA5	DMF	FA	1:5	—
FA10	DMF	FA	1:10	—
FA20	DMF	FA	1:20	—
FA100	DMF	FA	1:100	—
AA1	DMF	AA	1:1	—
AA5	DMF	AA	1:5	—
AA10	DMF	AA	1:10	—
AA20	DMF	AA	1:20	—
AA100	DMF	AA	1:100	—
BA1	DMF	BA	1:1	—
BA5	DMF	BA	1:5	—
BA10	DMF	BA	1:10	—
BA20	DMF	BA	1:20	—
BA100	DMF	BA	1:100	Completely dissolved
JM237	None	None	None	Parent material
JM328	H ₂ O	FA	1:10	—
JM329	H ₂ O	FA	1:100	—
JM330	H ₂ O	AA	1:10	—
JM331	H ₂ O	AA	1:100	—
JM332	H ₂ O	BA	1:10	—
JM333	H ₂ O	BA	1:100	—
JM334	H ₂ O	TFA	1:10	—
JM335	H ₂ O	TFA	1:100	—
JM351	MeOH	FA	1:10	—
JM352	MeOH	FA	1:100	—
JM353	MeOH	AA	1:10	—
JM354	MeOH	AA	1:100	—
JM355	MeOH	BA	1:10	—
JM356	MeOH	BA	1:100	—
JM357	MeOH	TFA	1:10	—
JM358	MeOH	TFA	1:100	—
JM359	MeOH	None	0	Control
JM360	DMSO	FA	1:10	—
JM361	DMSO	FA	1:100	—
JM362	DMSO	AA	1:10	—
JM363	DMSO	AA	1:100	—
JM364	DMSO	BA	1:10	—
JM365	DMSO	BA	1:100	—
JM366	DMSO	TFA	1:10	—
JM367	DMSO	TFA	1:100	Completely dissolved
JM368	DMSO	None	0	Control

3. Exploring the impact of synthesis and defects on adsorption measurements

3.3.2. Methods for quantifying defects

Determining the abundance of missing linker and missing cluster defects and characterising their distribution is a major challenge, as the components of the framework do not change, only their local order.

One of the most accessible way of assessing the defectivity of a MOF is thermogravimetry (TGA). Through heating in an oxygen-rich atmosphere, the MOF is normally reduced to its metal oxide and a stoichiometric analysis of the TGA curve can allow for the percentage of missing linkers to be determined. TGA curves for this study were measured under an air atmosphere using the method described in section A.1. A heating rate of $5\text{ }^{\circ}\text{C min}^{-1}$ was used, as it is assumed to be low enough for the sample to be in permanent thermal equilibrium with the furnace. The curves are then normalized with respect to the weight at $600\text{ }^{\circ}\text{C}$, which corresponds to pure ZrO_2 . The maximum possible mass loss of a solvent-free structure is calculated from the ratio of the fully-substituted, but dehydroxilated, metallic cluster $\text{Zr}_6\text{O}_6(\text{C}_6\text{H}_4(\text{COO})_2)_6$. The plateau of the TGA curve between $400\text{ }^{\circ}\text{C}$ to $500\text{ }^{\circ}\text{C}$, in the range where it is assumed that the molecules included in the framework are completely evacuated, is used as a measure of the number of terephthalate linkers which are missing.

If the distribution of defects can introduce changes in the long-range order and topology of their parent framework, such as by the introduction of phase changes, additional peaks can be observed through regular powder diffraction techniques. As Cliffe et al. has shown⁽¹⁰⁾, the UiO-66 defect-free face-centred unit (**fcu**) net can be transformed through missing cluster defects into a (**reo**) net. Short-range correlations of such domains form nanoregions inside the parent structure and generate diffuse scattering peaks observable at low angles in powder X-ray (pXRD) diffraction patterns, corresponding to “forbidden” reflections in a primitive cubic superstructure. As such, these pXRD peaks can be used to verify the existence of missing cluster defects, but only when their abundance allows for nanodomains of (**reo**) nets to be formed. In this study, pXRD measurements were performed as described in section A.8.

In order to check for the inclusion of a modulator in the framework, the MOF can be digested with the help of a hydrofluoric acid and the resulting solution can be analysed through proton nuclear magnetic resonance (^1H NMR) or high performance liquid chromatography (HPLC). In this study, ^1H NMR was used through the procedure detailed in section A.9 to qualitatively and quantitatively assess the presence of the capping agents in the UiO-66(Zr) samples.

Finally, both nitrogen adsorption at 77 K and CO_2 adsorption at 303 K can be used to describe the surface characteristics and porosity of the samples. The methods for obtaining the isotherms are presented in detail in section A.4 and section A.7 for N_2 and CO_2 respectively.

method

3.4. Results and discussion

3.4.1. Crystallinity of leached samples

The crystallinity of the leached samples is verified through XRD. The results in section D.2 confirm that all resulting materials retain the same peaks in their powder diffraction patterns.

A closer look at the low angle scattering (Figure 3.3) reveals the appearance of diffuse peaks, corresponding to forbidden reflections of the (**reo**) phase. They confirm that the leached samples begin to exhibit phase coexistence of the original UiO-66(Zr) unit cell and the missing cluster (**reo**) net. These peaks have the highest intensity in the TFA treated materials, suggesting that it has the highest capability of introducing missing cluster defects.

3.4.2. NMR

Waiting for results from Joao

3.4.3. Thermogravimetry results

A typical TGA curve, as measured on a pristine material is characterised by three main mass losses: a loss at low temperature, usually until 100 °C, which is indicative of adsorbed water from the environment; a secondary mass loss in the 100 °C to 200 °C range, corresponding to the evacuation of residual solvent from the pores and finally, a large step which is a sign of sample degradation as the linker is oxidized.

A selection of TGA curves measured on the leached samples can be seen in Figure 3.4. The complete set of data can be found in Appendix D, section D.3.

There are four types of differences that can arise between curves on different samples:

- the aforementioned change in overall height, which indicates the presence of missing linker defects;
- differences in the solvent removal step, as they have different boiling points and interactions with the framework;
- in case the defects are capped by an agent such as the modulator molecule used, it may introduce a new mass loss step between solvent removal and complete structure breakdown;
- finally, a highly defective structure loses part of its thermal resistance altering both the onset of mass loss and the final decomposition temperature.

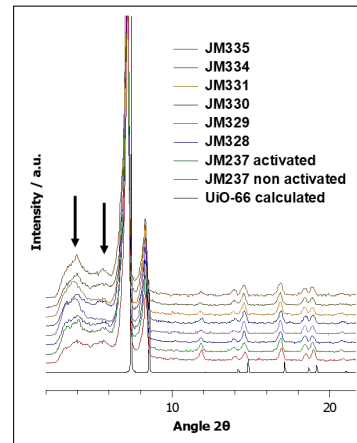


Figure 3.3.: Diffuse scattering peaks in the H₂O leached samples.

3. Exploring the impact of synthesis and defects on adsorption measurements

From the TGA curve of the pristine UiO-66 material, it is immediately obvious that there are some defects already present in the sample. By using the normalized mass at 420 °C a linker-to-cluster ratio of around 11.6:1 can be calculated. This shows that there are still intrinsic defects in the as-synthesised structure. These defects are most likely capped by formate moieties, which have been generated during the solvothermal synthesis in DMF through solvent self-hydrolysis (Equation 3.1), as commercially available solvent has a small percentage of residual water.⁽⁴⁰⁾



It follows that the mass loss step around 250 °C is the evacuation of formate capping agents from the structure, to generate an open metal site. The same step can be found in the samples which have been leached with formic acid.

In leached samples where other acids were used, it is likely that the original formate capping the defects has been replaced with an acid molecule from solution, either because it is thermodynamically favourable, or simply through kinetic means due to the large excess present. As evidenced in Figure 3.4, the mass loss corresponding to the formate is reduced, or no longer seen. Acetic acid (Figure 3.4d) leaves the structure at a higher temperature, as a new peak is present at 390 °C. Strongly bound capping agents at defect sites have been shown to require a higher activation temperature to fully remove.⁽⁵⁸⁾ Benzoic acid (Figure 3.4c) introduces a progressive mass loss near the total decomposition temperature of 550 °C. As it is similar to the BTC linker, its higher stability is not surprising. Finally, the samples leached with TFA have a more complicated curve, with two or even three peaks in the first derivative with respect to temperature. This kind of degradation suggests the existence of different types of capping sites, some more strongly bound than others. A slight difference is also observed in thermal stability, with all TFA samples having a 20 °C to 30 °C increase in decomposition temperature. Since defects normally have a negative impact on the thermal and mechanical resistance of a MOF, high resolution TGA experiments were carried out to eliminate possible influences of heating rate. The resulting curves (Figure D.6) still display the same behaviour. The effect is likely due to the electron-withdrawing effect of the TFA molecule on the Zr node, which induces a stronger Zr-carboxilate bond. A similar paradoxical increase in mechanical stability has been shown by Van de Voorde et al. on TFA modulated defective UiO-66 materials.⁽⁵⁹⁾

The solvent used can be removed in all cases before 200 °C. DMSO has the highest preponderence in the leached samples (Figure 3.4d) and is the most difficult to remove, likely due to its high boiling point.

It is also clearly visible that the leaching procedure has, led to the generation of defects. The curves of the leached samples fall below that of the original material in normalized weight, indicative of a lower linker-to-node ratio. These trends are analysed in subsection 3.4.5.

3. Exploring the impact of synthesis and defects on adsorption measurements

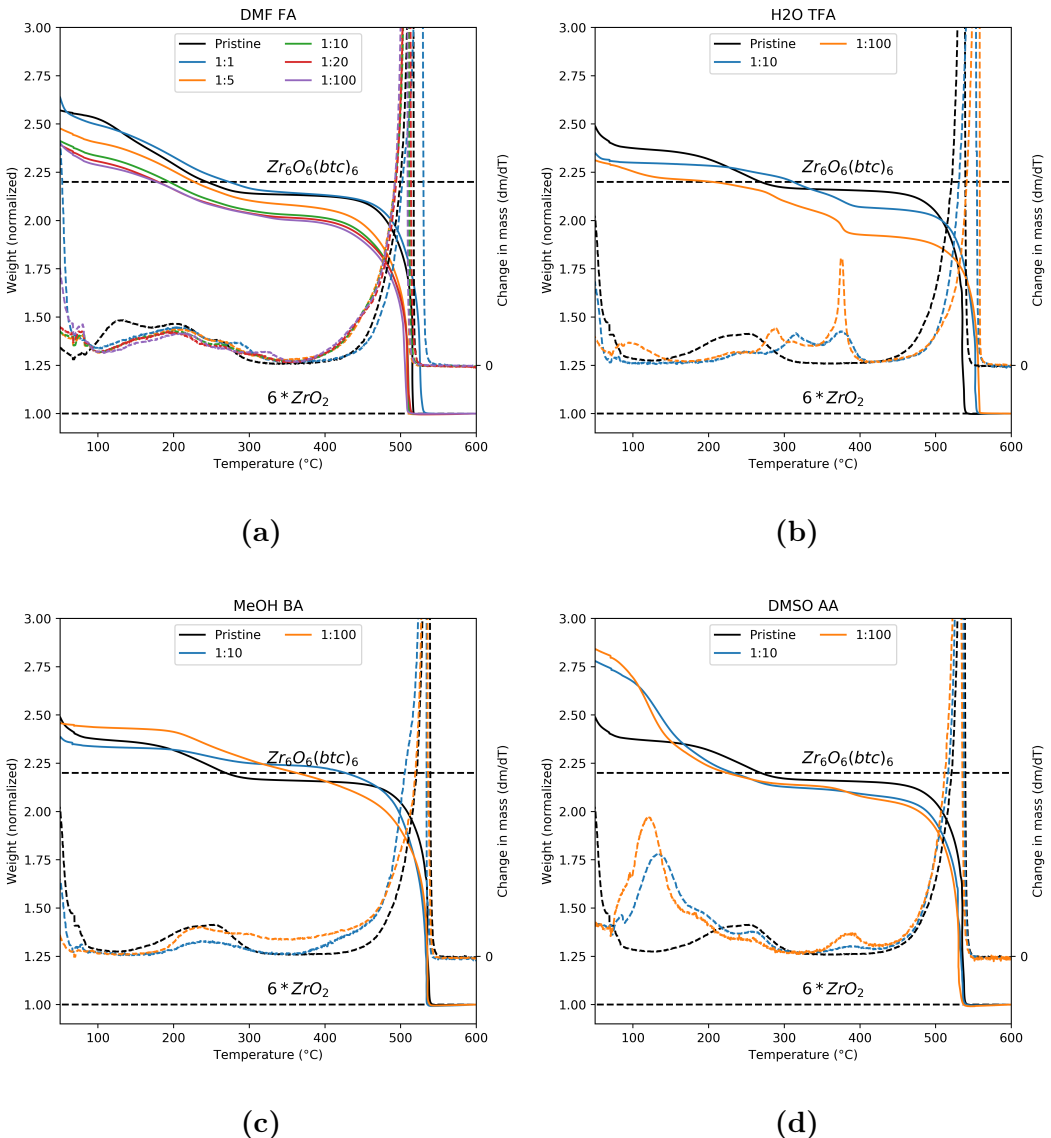


Figure 3.4.: A selection of the TGA curves as measured on the leached samples: (a) formic acid in DMF, (b) trifluoroacetic acid in water, (c) benzoic acid in methanol and (d) acetic acid in DMSO. The curve for the parent material is in black. Dotted lines correspond to the secondary y axis as a semilogarithm of the first derivative of mass loss with respect to temperature.

3. Exploring the impact of synthesis and defects on adsorption measurements

3.4.4. Nitrogen sorption at 77K

Isotherms have been recorded on samples activated at both 200 °C and 320 °C. It is important to note that, as seen from the TGA curves, not all capping agents leave the structure when thermal treating at a lower temperature. The moieties which are still coordinated to the Zr cluster will likely influence the adsorption behaviour. At a high temperature, the dehydroxilation of the metal center also occurs⁽⁵²⁾, which may also affect the interaction with physisorbed probes. Several example isotherms can be found in Figure 3.5, with the complete dataset present in Appendix D, section D.4.

There are a few isotherm features which can be analysed to assess the type of modifications introduced in the structure and their preponderence.

- The slope of the isotherm at low p/p_0 is representative of the first interactions with the pore surface, which can be quantified using the initial Henry constant. It will be influenced by any changes in pore environment such as CUS or functionalised defect sites.
- Missing linker defects will lead to an increase of the apparent surface area and perhaps to a more extensive pore network.
- The pore size distribution and total pore volume give indications on the presence of missing cluster defects and/or of the formation of mesoporous voids within the structure.
- A steep step at high p/p_0 is indicative of intercrystal condensation and suggests particle aggregation due to lower average crystal size.

It is immediately apparent that the leaching process had an influence on the adsorption characteristics of UiO-66. Isotherms of acid treated samples diverge from the parent material, often at different pressures. In general, the total molar capacity at full loading is seen to increase, a telltale sign of an increase in pore volume through defect generation. On the other hand, other particularities exist, such as the benzoic acid samples in methanol and DMSO where the low and high concentration has opposite effect on the total loading. Predictors of defects and trends will be analysed in the following section.

3.4.5. Characterisation of trends

The graphs in Figure 3.6 summarize the trends in missing linker defects as calculated through the TGA plateau at 420 °C. The DMF leached samples, due to the multiple datapoints with different acid concentrations show the clearest influence of this variable on defect generation. Even small amounts of modulator leads to the decrease of the linker-to-node ratio, but the increase in concentration stops having an effect at around 20:1 equivalents. It is likely that the trends are similar with other solvents, even if less datapoints are available.

In the case of benzoic acid the data bears careful interpretation. Thermogravimetric methods may not be suitable for assessing the resulting defects. The comparatively large

3. Exploring the impact of synthesis and defects on adsorption measurements

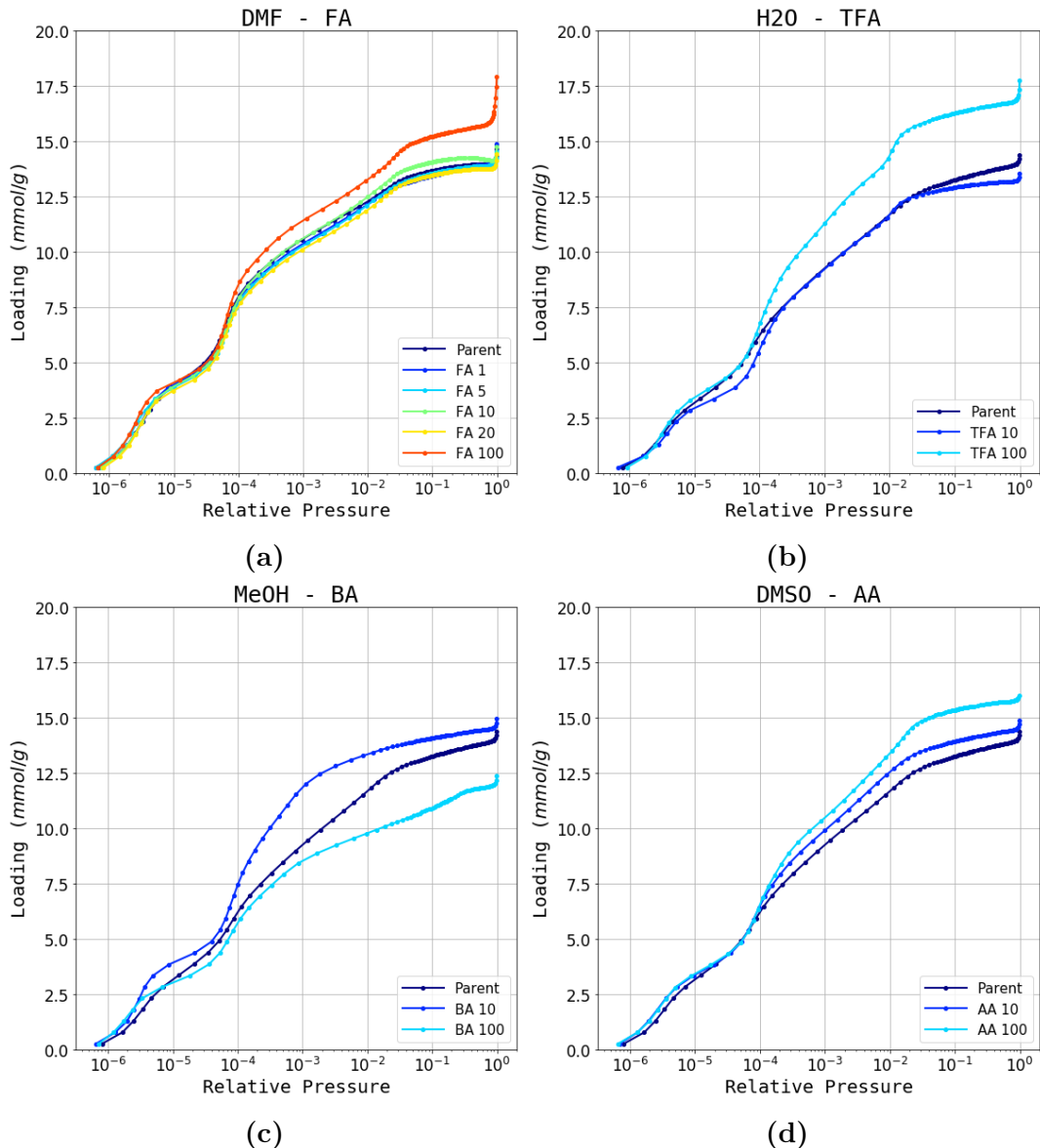


Figure 3.5.: A selection of nitrogen sorption isotherms as measured on the leached samples at 200 °C: (a) formic acid in DMF, (b) trifluoroacetic acid in water, (c) benzoic acid in methanol and (d) acetic acid in DMSO. The curve for the parent material is in dark blue. The x axis is logarithmic for clarity of low pressure points.

3. Exploring the impact of synthesis and defects on adsorption measurements

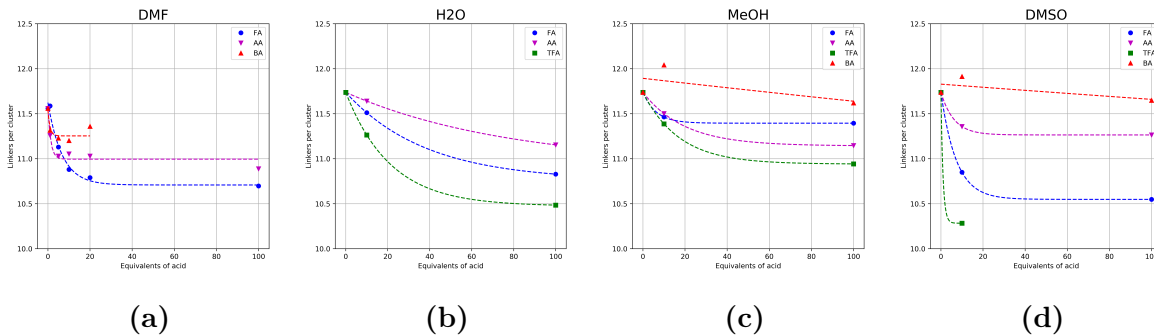


Figure 3.6.: Calculated linker-to-node ratio from the TGA curve normalized mass at 420 °C for (a) DMF (b) H₂O, (c) MeOH and (d) DMSO leached samples. A ratio of 12 to 1 corresponds to a completely defect-free structure. An exponential decay trendline is fitted to each set of points.

molecule, high boiling point and similarity to the terephthalate linker make the removal of benzoic acid capping open metal sites harder, and as such, the plateau is not an accurate indication of defectivity. Indeed, the calculated linker ratio is seen to actually increase in the case of methanol and DMSO. We propose that in benzoic acid leached samples defect generation occurs through the coordination of two benzoic molecules (or one, in the case of a “dangling” linker), as seen in Figure 3.7, with the increased amount of organic material effectively compensating for any defects that could be seen in the TGA curve.

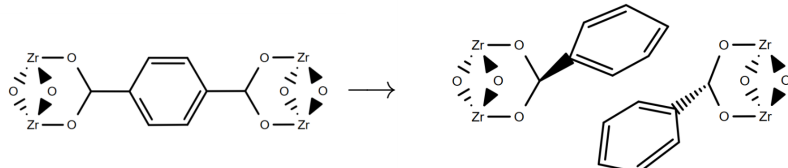


Figure 3.7.: A defect site created through benzoic acid.

For the nitrogen adsorption dataset, the predictors described in the previous section have been calculated using the pyGAPS framework (methods are described in chapter 1). The Henry constant is determined through the initial slope method, with a linear section found below 10^{-4} p/p_0 . Total pore volume is taken as the liquid density of the amount adsorbed at 0.8 p/p_0 , assuming that nitrogen is in a liquid-like state in the MOF pores. The pore size distribution was calculated through the Horvatz-Kawazoe method for micropores, the Dollimore-Heal method for mesopores and DFT kernel fitting for a multiscale distribution. While the applicability of these methods for determination of absolute pore size of the UiO-66 framework may be put into question, they can be readily used to compare between different samples of the same material. In general, the leaching process has a positive effect on surface area and pore volume, both of which increase with a higher concentration of acid used. The strength of the initial interaction

3. Exploring the impact of synthesis and defects on adsorption measurements

of the nitrogen probe with the pore walls is changed as well, with more defective samples likely to have a more pronounced interaction, either through the introduction of CUS or modification of pore environment.

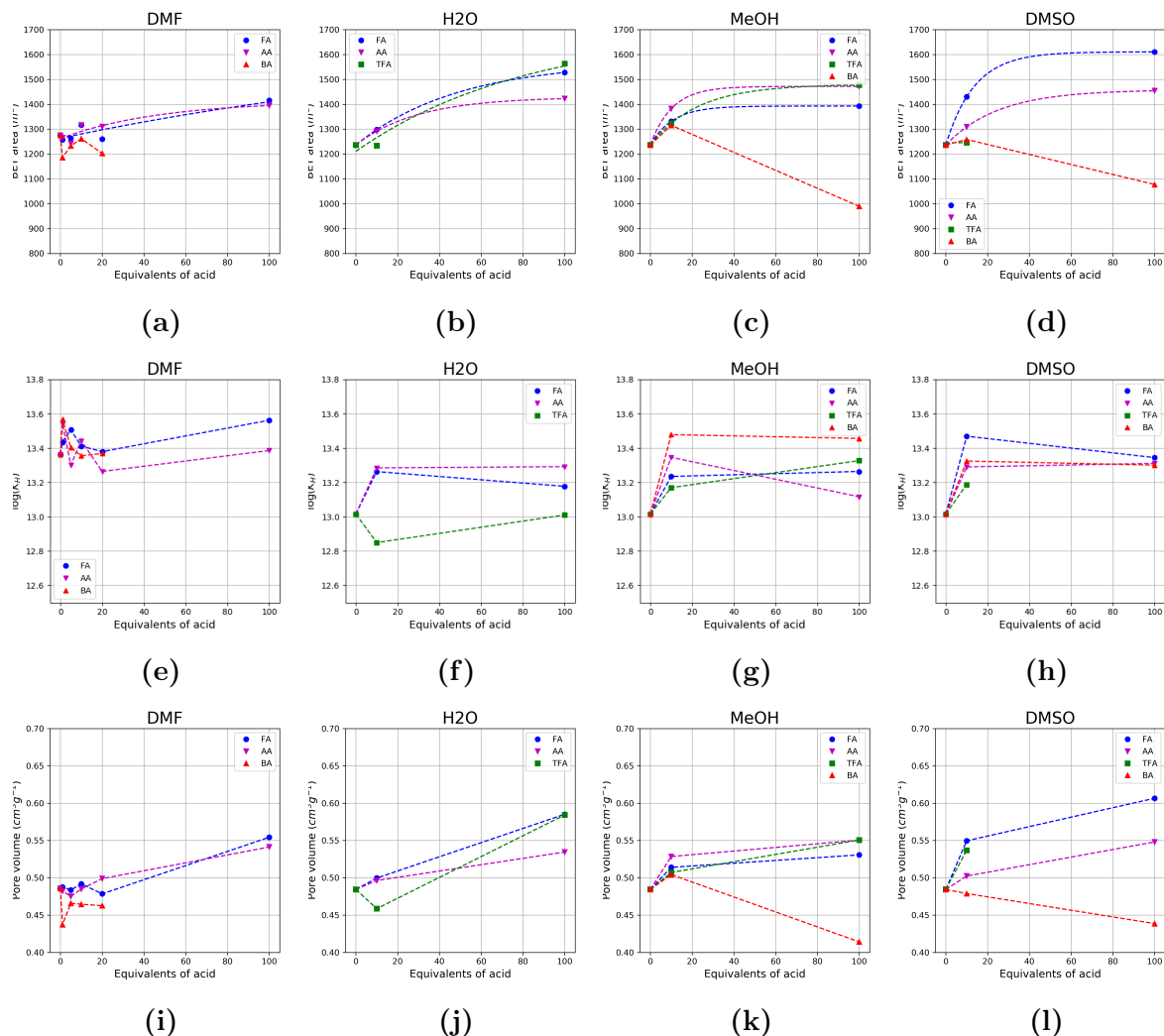


Figure 3.8.: Characterisation of all samples through predictors obtained through processing of the nitrogen physisorption data at 200 °C. The figure shows BET surface area (a-d), the logarithm of the initial Henry constant (e-h), and calculated pore volume (i-l) for DMF, H₂O, MeOH and DMSO leached materials, respectively.

The influence of the acid on the linker-to-node ratio appears to be constant throughout the solvents used, with an overall trend of TFA > FA > AA > BA. The order is similar to the acidic character of the compounds, except for benzoic acid which has a lower pKa (4.2) than acetic acid (4.7). The result is in accordance to the trend published by Shearer et al. when analysing the influence of these acids as used during modulated synthesis on the defectivity of the resulting material.⁽⁴⁰⁾

3. Exploring the impact of synthesis and defects on adsorption measurements

When examining the influence of the solvent, another trend appears to emerge, with samples leached in DMSO having the largest propensity for defect generation, followed by DMF, water and methanol. In fact, a sample with high concentration of TFA cannot be obtained, as the framework simply dissolves in the solution. The contribution of the solvent is not as easy to determine due to the complex interplay of multiple factors. The polarity of the solvent molecule has been linked to the speed of post synthetic ligand exchange from pristine UiO-66(Zr).⁽⁴⁷⁾ The leaching results do not, however, conform to the same trend, as water with a relative polarity of 1.0 introduces more defects than methanol (0.7) while DMF (0.38) is less effective than DMSO (0.44). The solubility of terephthalic acid in the solvent of choice may likely be a limiting factor driving its removal from the framework. Water, which has the lowest solubility for BTC, is one of the better solvents for defect generation, likely due to the high temperature of the reaction. As a strong acid is added, the equilibrium shifts even more towards the left, which may explain the worse performance of low equivalents of TFA in water as seen from adsorption predictors. At high concentrations, it is likely that the rate constant for the protonation of the metal-oxygen bond starts to dominate the leaching process. The viscosity of the solvent may also play a role in the mass transport of compounds through the porous media. However, the liquid with the highest kinematic viscosity, DMSO is actually the top performer during leaching, indicating that mass transfer is not a factor.

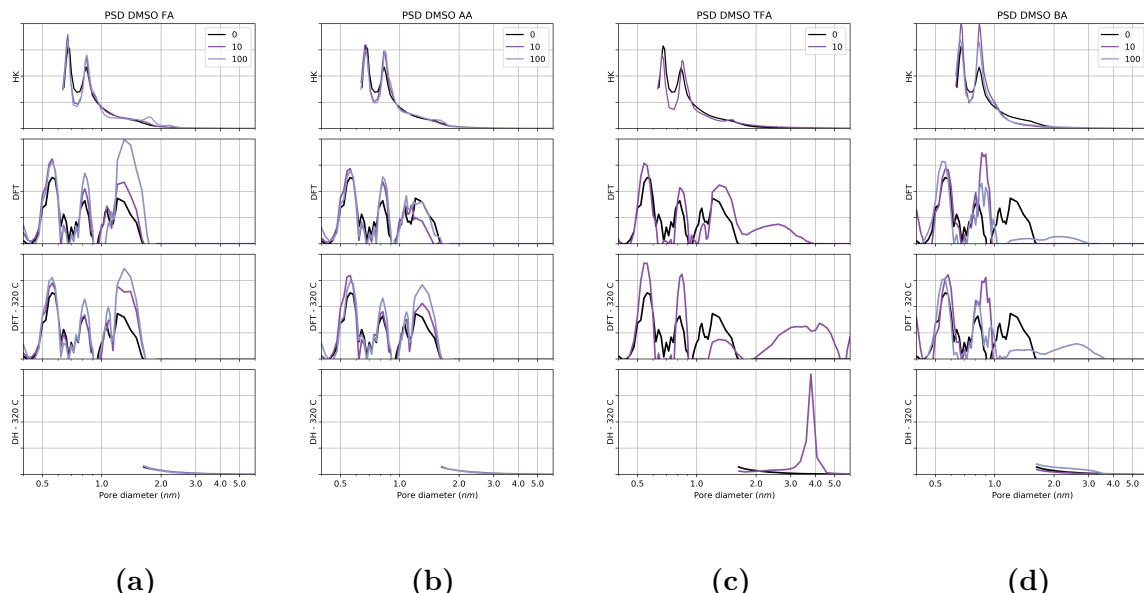


Figure 3.9.: Pore size distribution for the DMSO-leached samples as resulting from the HK (top), DFT (middle) and DH (bottom) methods on (a) formic acid, (b) acetic acid, (c) TFA and (d) BA. The top and bottom two distributions are calculated on the low and high temperature activated material respectively. The parent material is depicted in black.

The calculated pore sizes with both the HK method and the DFT method show

3. Exploring the impact of synthesis and defects on adsorption measurements

two sharp peaks corresponding to the octahedral and tetrahedral pores in the UiO-66 structure. In Figure 3.9, the pore size distribution for the DMSO dataset is depicted, for both low temperature and high temperature activated variants. The appearance of a tertiary pore is visible in the leached samples with formic, acetic and trifluoroacetic acid. This pore size likely corresponds to the increased pore volume introduced by missing linker-type defects. The calculated diameter of this tertiary pore is inversely proportional to the molecular size of the leaching compound used, which is a clear indication of the presence of the acid molecules in the structure as capping agents. On the samples which have been activated at 320 °C, the pore width shifts to a single value as the coordinated acids are evacuated.

The pore size distribution calculated in the benzoic acid leached samples shows the disappearance of peaks larger than around 1 nm, as the compound replaces formate as the capping agent for the initial defects in the structure. Due to the similarity of the terephthalate linker with benzoate, the structure becomes more “ideal” than the pristine material. At high concentrations of benzoic acid, an overall decrease in porosity may be seen, as two benzoate molecules may act as capping agents in adjacent sites (Figure 3.7), effectively lowering the available pore volume. The effect is corroborated by trends in the linker-to-node ratio, surface area and total pore volume in both methanol, DMSO and to a lesser extent DMF.

At very high concentrations of TFA and BA, a fourth pore size begins to be appear in the DFT calculated pore distribution. This is likely evidence that missing cluster defects can be introduced at these concentrations. It should be noted that if such large-scale modifications of the structure are possible, complete structural breakdown is not far away. Indeed, samples with higher concentrations of acid could not be obtained with TFA in DMSO, with sample subjected to these conditions ending up completely dissolved. The appearance of this type of porosity in the samples treated with benzoic acid is counterintuitive, as the TGA linker ratio does not allude to any changes in coordination. In this case, it could be that missing cluster defects are still generated forming a **reo-benz** phase⁽⁶⁰⁾ while the excess of “dangling” benzoate moieties in the framework account for the decrease in surface area and capacity.

No hysteresis curve is observable on any samples activated at 200 °C. When activating at higher temperature, a hysteresis curve appears in the high concentration leached TFA samples (Figure 3.10), which corresponds to a pore size of around 4 nm in both DFT and DH calculated pore distribution. The shape of the hysteresis loop is also reminiscent of condensation in ink bottle-like pores, suggesting the existence of voids within the crystal matrix which are not directly accessible. This further confirms how effective highly acidic solutions can be at defect generation.

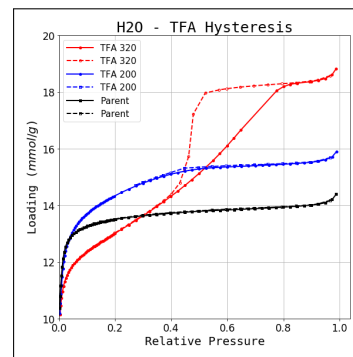


Figure 3.10.: Hysteresis loop in high temperature activated TFA treated UiO-66(Zr)

3. Exploring the impact of synthesis and defects on adsorption measurements

3.4.6. Carbon dioxide isotherms

The adsorption of carbon dioxide has been shown to be a good predictor for the presence of defects from comprehensive simulations by Thornton et al.. In their work⁽⁵⁴⁾ they have shown that in formate-capped defects, a shift of the CO₂ isotherm towards higher loading is seen at pressures over 5 bar, accompanied by a lower capacity at low pressures.

Carbon dioxide isotherms on the DMF sample set are shown in Figure 3.11. It can be seen that only the formic acid-treated samples show higher capacity throughout the measured pressure range. It is likely that the activation which was performed at 200 °C was insufficient for complete removal of the coordinated acids.

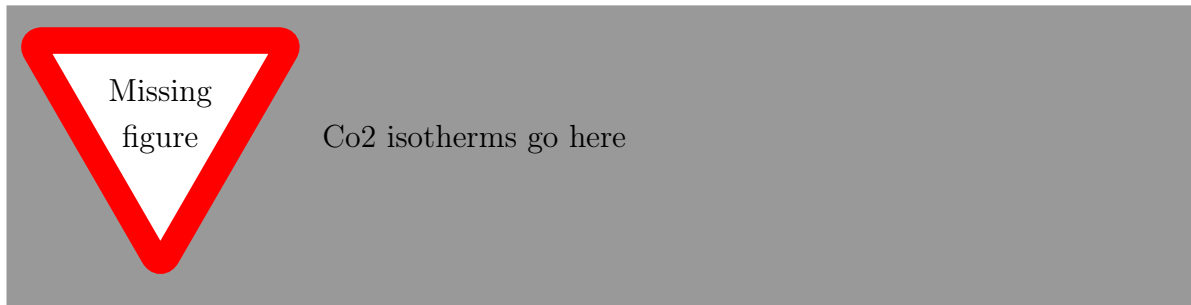


Figure 3.11.: CO₂ adsorption isotherms at 303 K

3.5. Conclusion

In summary, a new method of generating missing linker and missing cluster type defects in a UiO-66(Zr) framework has been presented. This type of post-synthetic modification is an alternative to modulated synthesis, and can be useful when crystal growth is not desirable. It also introduces new possibilities of framework functionalisation, through sequential rounds of leaching and defect healing. It does, however, come at a cost, as it also partially dissolves the material.

A few trends emerge in regards to the capacity of different solvents and acids to induce defect formation.

- The impact of the monotopic acid is mainly due to its acidity, with pK_a being a good predictor of the resulting defectivity.
- DMSO and water stand out as the most effective solvents for defect generation.
- In general, the leached samples have a larger surface area and pore volume, due to both missing linker and cluster defects. Benzoic acid is a special case where due to its large molecule, may instead result in a loss of available pore space.
- High concentrations of acids can induce mesoporosity through large-scale defect generation. These conditions also make the material susceptible to complete structural breakdown through attack at the crystal surface.
- The resulting defective structures may have different bulk properties such as thermal and mechanical resistance due to the influence of the defect capping agents.
- The coordinated acids can also have an impact on the adsorption properties through changes to the pore environment.

These results also show the vast influence that defects have on the adsorption properties of MOFs. From different interactions with the material surface to vastly different capacities and, in some cases, even changing the sizes of pores or introducing new porosity. When attempting to determine the adsorption performance and behaviour of a compound it is important to consider whether the material in question is representative of its stoichiometric composition or, as is more often the case, a complex interplay of ideal and non-ideal.

Bibliography

- [1] Robert E. Reed-Hill and R. Abbaschian. *Physical Metallurgy Principles*. The PWS-Kent series in engineering. PWS-Kent Pub, Boston, 3rd ed edition, 1992. ISBN 978-0-534-92173-6.
- [2] Roland A. Levy and North Atlantic Treaty Organization, editors. *Microelectronic Materials and Processes: Proceedings of the NATO Advanced Study Institute on Microelectronic Materials and Processes, Il Ciocco, Castelvecchio Pascoli, Italy, June 30-July 11, 1986*. Number vol. 164 in NATO ASI series. Series E, Applied sciences. Kluwer Academic, Dordrecht ; Boston, 1989. ISBN 978-0-7923-0147-9 978-0-7923-0154-7.
- [3] Anthony J. Leggett. What DO we know about high T c? *Nature Physics*, 2(3): 134–136, March 2006. ISSN 1745-2473, 1745-2481. doi: 10.1038/nphys254.
- [4] Yanzhong Pei, Heng Wang, and G. J. Snyder. Band Engineering of Thermoelectric Materials. *Advanced Materials*, 24(46):6125–6135, December 2012. ISSN 09359648. doi: 10.1002/adma.201202919.
- [5] David S. Sholl and Ryan P. Lively. Defects in Metal–Organic Frameworks: Challenge or Opportunity? *The Journal of Physical Chemistry Letters*, 6(17):3437–3444, September 2015. ISSN 1948-7185. doi: 10.1021/acs.jpclett.5b01135.
- [6] Jongwon Choi, Li-Chiang Lin, and Jeffrey C. Grossman. Role of Structural Defects in the Water Adsorption Properties of MOF-801. *The Journal of Physical Chemistry C*, 122(10):5545–5552, March 2018. ISSN 1932-7447, 1932-7455. doi: 10.1021/acs.jpcc.8b00014.
- [7] Pritha Ghosh, Yamil J. Colón, and Randall Q. Snurr. Water adsorption in UiO-66: The importance of defects. *Chem. Commun.*, 50(77):11329–11331, 2014. ISSN 1359-7345, 1364-548X. doi: 10.1039/C4CC04945D.
- [8] Jian-Rong Li, Ryan J Kuppler, and Hong-Cai Zhou. Selective gas adsorption and separation in metal–organic frameworks. *Chemical Society Reviews*, 38(5):1477, 2009. ISSN 0306-0012. doi: 10.1039/b802426j.
- [9] Matthew J. Cliffe, Elizabeth Castillo-Martínez, Yue Wu, Jeongjae Lee, Alexander C. Forse, Francesca C. N. Firth, Peyman Z. Moghadam, David Fairén-Jiménez, Michael W. Gaulois, Joshua A. Hill, Oxana V. Magdysyuk, Ben Slater, Andrew L. Goodwin, and Clare P. Grey. Metal–Organic Nanosheets Formed via Defect-Mediated Transformation of a Hafnium Metal–Organic Framework. *Journal of the American Chemical Society*, 139(15):5397–5404, April 2017. ISSN 0002-7863, 1520-5126. doi: 10.1021/jacs.7b00106.

BIBLIOGRAPHY

- [10] Matthew J Cliffe, Wei Wan, Xiaodong Zou, Philip a Chater, Annette K Kleppe, Matthew G Tucker, Heribert Wilhelm, Nicholas P Funnell, François-Xavier Coudert, and Andrew L Goodwin. Correlated defect nanoregions in a metal-organic framework. *Nature communications*, 5(May):4176, 2014. ISSN 2041-1723. doi: 10.1038/ncomms5176.
- [11] Thomas D. Bennett, Anthony K. Cheetham, Alain H. Fuchs, and François-Xavier Coudert. Interplay between defects, disorder and flexibility in metal-organic frameworks. *Nature Chemistry*, 9(1):11–16, December 2016. ISSN 1755-4330. doi: 10.1038/nchem.2691.
- [12] Weibin Liang, Lin Li, Jingwei Hou, Nicholas D. Shepherd, Thomas D. Bennett, Deanna M. D’Alessandro, and Vicki Chen. Linking defects, hierarchical porosity generation and desalination performance in metal-organic frameworks. *Chemical Science*, 9(14):3508–3516, 2018. ISSN 2041-6520, 2041-6539. doi: 10.1039/C7SC05175A.
- [13] Brandon J. Burnett, Paul M. Barron, and Wonyoung Choe. Recent advances in porphyrinic metal-organic frameworks: Materials design, synthetic strategies, and emerging applications. *CrystEngComm*, 14(11):3839, 2012. ISSN 1466-8033. doi: 10.1039/c2ce06692k.
- [14] Mian Li, Dan Li, Michael O’Keeffe, and Omar M. Yaghi. Topological Analysis of Metal–Organic Frameworks with Polytopic Linkers and/or Multiple Building Units and the Minimal Transitivity Principle. *Chemical Reviews*, 114(2):1343–1370, January 2014. ISSN 0009-2665, 1520-6890. doi: 10.1021/cr400392k.
- [15] Norbert Stock and Shyam Biswas. Synthesis of Metal-Organic Frameworks (MOFs): Routes to Various MOF Topologies, Morphologies, and Composites. *Chemical Reviews*, 112(2):933–969, February 2012. ISSN 0009-2665, 1520-6890. doi: 10.1021/cr200304e.
- [16] Bart Bueken, Niels Van Velthoven, Andraž Krajnc, Simon Smolders, Francis Taulelle, Caroline Mellot-Draznieks, Gregor Mali, Thomas D. Bennett, and Dirk De Vos. Tackling the Defect Conundrum in UiO-66: A Mixed-Linker Approach to Engineering Missing Linker Defects. *Chemistry of Materials*, 29(24):10478–10486, December 2017. ISSN 0897-4756, 1520-5002. doi: 10.1021/acs.chemmater.7b04128.
- [17] Amarajothi Dhakshinamoorthy, Abdullah M. Asiri, and Hermenegildo Garcia. Mixed-metal or mixed-linker metal organic frameworks as heterogeneous catalysts. *Catalysis Science & Technology*, 6(14):5238–5261, 2016. ISSN 2044-4753, 2044-4761. doi: 10.1039/C6CY00695G.
- [18] Ji Woong Yoon, You-Kyong Seo, Young Kyu Hwang, Jong-San Chang, Hervé Leclerc, Stefan Wuttke, Philippe Bazin, Alexandre Vimont, Marco Daturi, Emily Bloch, Philip L. Llewellyn, Christian Serre, Patricia Horcajada, Jean-Marc

BIBLIOGRAPHY

- Grenèche, Alirio E. Rodrigues, and Gérard Férey. Controlled Reducibility of a Metal–Organic Framework with Coordinatively Unsaturated Sites for Preferential Gas Sorption. *Angewandte Chemie International Edition*, 49(34):5949–5952, August 2010. ISSN 14337851. doi: 10.1002/anie.201001230.
- [19] Kai Müller, Karin Fink, Ludger Schöttner, Meike Koenig, Lars Heinke, and Christof Wöll. Defects as Color Centers: The Apparent Color of Metal–Organic Frameworks Containing Cu²⁺-Based Paddle-Wheel Units. *ACS Applied Materials & Interfaces*, 9(42):37463–37467, October 2017. ISSN 1944-8244, 1944-8252. doi: 10.1021/acsami.7b12045.
- [20] Paolo Falcaro, Raffaele Ricco, Amiral Yazdi, Inhar Imaz, Shuhei Furukawa, Daniel Maspoch, Rob Ameloot, Jack D. Evans, and Christian J. Doonan. Application of metal and metal oxide nanoparticles@MOFs. *Coordination Chemistry Reviews*, 307: 237–254, January 2016. ISSN 00108545. doi: 10.1016/j.ccr.2015.08.002.
- [21] Felicitas Schröder, Daniel Esken, Mirza Cokoja, Maurits W. E. van den Berg, Oleg I. Lebedev, Gustaaf Van Tendeloo, Bernadeta Walaszek, Gerd Buntkowsky, Hans-Heinrich Limbach, Bruno Chaudret, and Roland A. Fischer. Ruthenium Nanoparticles inside Porous [Zn₄O(bdc)₃] by Hydrogenolysis of Adsorbed [Ru(cod)(cot)]: A Solid-State Reference System for Surfactant-Stabilized Ruthenium Colloids. *Journal of the American Chemical Society*, 130(19):6119–6130, May 2008. ISSN 0002-7863, 1520-5126. doi: 10.1021/ja078231u.
- [22] Gia-Thanh Vuong, Minh-Hao Pham, and Trong-On Do. Synthesis and engineering porosity of a mixed metal Fe₂Ni MIL-88B metal–organic framework. *Dalton Trans.*, 42(2):550–557, 2013. ISSN 1477-9226, 1477-9234. doi: 10.1039/C2DT32073H.
- [23] Qingxia Yao, Jie Su, Ocean Cheung, Qingling Liu, Niklas Hedin, and Xiaodong Zou. Interpenetrated metal–organic frameworks and their uptake of CO₂ at relatively low pressures. *Journal of Materials Chemistry*, 22(20):10345, 2012. ISSN 0959-9428, 1364-5501. doi: 10.1039/c2jm15933c.
- [24] Ritesh Haldar, Nivedita Sikdar, and Tapas Kumar Maji. Interpenetration in coordination polymers: Structural diversities toward porous functional materials. *Materials Today*, 18(2):97–116, March 2015. ISSN 13697021. doi: 10.1016/j.mattod.2014.10.038.
- [25] Rocio Semino, Naseem A. Ramsahye, Aziz Ghoufi, and Guillaume Maurin. Microscopic Model of the Metal–Organic Framework/Polymer Interface: A First Step toward Understanding the Compatibility in Mixed Matrix Membranes. *ACS Applied Materials & Interfaces*, 8(1):809–819, January 2016. ISSN 1944-8244, 1944-8252. doi: 10.1021/acsami.5b10150.
- [26] Hartmut Gliemann and Christof Wöll. Epitaxially grown metal-organic frameworks. *Materials Today*, 15(3):110–116, March 2012. ISSN 13697021. doi: 10.1016/S1369-7021(12)70046-9.

BIBLIOGRAPHY

- [27] Ivo Stassen, Nicholas Burtch, Alec Talin, Paolo Falcaro, Mark Allendorf, and Rob Ameloot. An updated roadmap for the integration of metal-organic frameworks with electronic devices and chemical sensors. *Chemical Society Reviews*, 46(11):3185–3241, 2017. ISSN 0306-0012. doi: 10.1039/C7CS00122C.
- [28] Simon Krause, Volodymyr Bon, Irena Senkovska, Daniel M. Többens, Dirk Wallacher, Renjith S. Pillai, Guillaume Maurin, and Stefan Kaskel. The effect of crystallite size on pressure amplification in switchable porous solids. *Nature Communications*, 9(1), December 2018. ISSN 2041-1723. doi: 10.1038/s41467-018-03979-2.
- [29] L. Vanduyfhuys, S. M. J. Rogge, J. Wieme, S. Vandenbrande, G. Maurin, M. Waroquier, and V. Van Speybroeck. Thermodynamic insight into stimuli-responsive behaviour of soft porous crystals. *Nature Communications*, 9(1), December 2018. ISSN 2041-1723. doi: 10.1038/s41467-017-02666-y.
- [30] Stefano Dissegna, Rifan Hardian, Konstantin Epp, Gregor Kieslich, Marie-Vanessa Coulet, Philip Llewellyn, and Roland A. Fischer. Using water adsorption measurements to access the chemistry of defects in the metal-organic framework UiO-66. *CrystEngComm*, pages 1–8, 2017. ISSN 1466-8033. doi: 10.1039/C7CE00224F.
- [31] Chiara Caratelli, Julianna Hajek, Francisco G. Cirujano, Michel Waroquier, Francesc X. Llabrés i Xamena, and Veronique Van Speybroeck. Nature of active sites on UiO-66 and beneficial influence of water in the catalysis of Fischer esterification. *Journal of Catalysis*, 352:401–414, August 2017. ISSN 00219517. doi: 10.1016/j.jcat.2017.06.014.
- [32] Thomas M. McDonald, Jarad A. Mason, Xueqian Kong, Eric D. Bloch, David Gygi, Alessandro Dani, Valentina Crocellà, Filippo Giordanino, Samuel O. Odoh, Walter S. Drisdell, Bess Vlaisavljevich, Allison L. Dzubak, Roberta Poloni, Sondre K. Schnell, Nora Planas, Kyuho Lee, Tod Pascal, Liwen F. Wan, David Prendergast, Jeffrey B. Neaton, Berend Smit, Jeffrey B. Kortright, Laura Gagliardi, Silvia Bordiga, Jeffrey A. Reimer, and Jeffrey R. Long. Cooperative insertion of CO₂ in diamine-appended metal-organic frameworks. *Nature*, 519:303, March 2015.
- [33] Douglas A. Reed, Benjamin K. Keitz, Julia Oktawiec, Jarad A. Mason, Tomče Runčevski, Dianne J. Xiao, Lucy E. Darago, Valentina Crocellà, Silvia Bordiga, and Jeffrey R. Long. A spin transition mechanism for cooperative adsorption in metal-organic frameworks. *Nature*, September 2017. ISSN 0028-0836, 1476-4687. doi: 10.1038/nature23674.
- [34] Nicholas C. Burtch, Himanshu Jasuja, and Krista S. Walton. Water Stability and Adsorption in Metal–Organic Frameworks. *Chemical Reviews*, 114(20):10575–10612, October 2014. ISSN 0009-2665, 1520-6890. doi: 10.1021/cr5002589.
- [35] J. Raziel Álvarez, Elí Sánchez-González, Eric Pérez, Emilia Schneider-Revuelta, Ana Martínez, Adriana Tejeda-Cruz, Alejandro Islas-Jácome, Eduardo González-Zamora, and Ilich A. Ibarra. Structure stability of HKUST-1 towards water and

BIBLIOGRAPHY

- ethanol and their effect on its CO₂ capture properties. *Dalton Transactions*, 46(28):9192–9200, 2017. ISSN 1477-9226, 1477-9234. doi: 10.1039/C7DT01845B.
- [36] Lei Shen, Shuo-Wang Yang, Shengchang Xiang, Tao Liu, Bangchuan Zhao, Man-Fai Ng, Jörg Göettlicher, Jiabao Yi, Sean Li, Lan Wang, Jun Ding, Banglin Chen, Su-Huai Wei, and Yuan Ping Feng. Origin of Long-Range Ferromagnetic Ordering in Metal–Organic Frameworks with Antiferromagnetic Dimeric-Cu(II) Building Units. *Journal of the American Chemical Society*, 134(41):17286–17290, October 2012. ISSN 0002-7863, 1520-5126. doi: 10.1021/ja3077654.
 - [37] Zhenlan Fang, Bart Bueken, Dirk E. De Vos, and Roland A. Fischer. Defect-Engineered Metal-Organic Frameworks. *Angewandte Chemie International Edition*, 54(25):7234–7254, June 2015. ISSN 14337851. doi: 10.1002/anie.201411540.
 - [38] Wenhua Zhang, Max Kauer, Olesia Halbherr, Konstantin Epp, Penghu Guo, Miguel I. Gonzalez, Dianne J. Xiao, Christian Wiktor, Francesc X. Llabrés i Xamena, Christof Wöll, Yuemin Wang, Martin Muhler, and Roland A. Fischer. Ruthenium Metal-Organic Frameworks with Different Defect Types: Influence on Porosity, Sorption, and Catalytic Properties. *Chemistry - A European Journal*, 22(40):14297–14307, September 2016. ISSN 09476539. doi: 10.1002/chem.201602641.
 - [39] Andreas Schaate, Pascal Roy, Adelheid Godt, Jann Lippke, Florian Waltz, Michael Wiebcke, and Peter Behrens. Modulated Synthesis of Zr-Based Metal-Organic Frameworks: From Nano to Single Crystals. *Chemistry - A European Journal*, 17(24):6643–6651, June 2011. ISSN 09476539. doi: 10.1002/chem.201003211.
 - [40] Greig C. Shearer, Sachin Chavan, Silvia Bordiga, Stian Svelle, Unni Olsbye, and Karl Petter Lillerud. Defect Engineering: Tuning the Porosity and Composition of the Metal-Organic Framework UiO-66 via Modulated Synthesis. *Chemistry of Materials*, 28(11):3749–3761, 2016. ISSN 15205002. doi: 10.1021/acs.chemmater.6b00602.
 - [41] Frederik Vermoortele, Rob Ameloot, Luc Alaerts, Roman Matthessen, Bert Carlier, Enrique V. Ramos Fernandez, Jorge Gascon, Freek Kapteijn, and Dirk E. De Vos. Tuning the catalytic performance of metal–organic frameworks in fine chemistry by active site engineering. *Journal of Materials Chemistry*, 22(20):10313, 2012. ISSN 0959-9428, 1364-5501. doi: 10.1039/c2jm16030g.
 - [42] Srinivas Gadipelli and Zhengxiao Guo. Postsynthesis Annealing of MOF-5 Remarkably Enhances the Framework Structural Stability and CO₂ Uptake. *Chemistry of Materials*, 26(22):6333–6338, November 2014. ISSN 0897-4756, 1520-5002. doi: 10.1021/cm502399q.
 - [43] Greig C. Shearer, Jenny G. Vitillo, Silvia Bordiga, Stian Svelle, Unni Olsbye, and Karl Petter Lillerud. Functionalizing the Defects: Postsynthetic Ligand Exchange in the Metal Organic Framework UiO-66. *Chemistry of Materials*, 28(20):7190–7193, October 2016. ISSN 0897-4756. doi: 10.1021/acs.chemmater.6b02749.

BIBLIOGRAPHY

- [44] Stephan Bernt, Vincent Guillerm, Christian Serre, and Norbert Stock. Direct covalent post-synthetic chemical modification of Cr-MIL-101 using nitrating acid. *Chemical Communications*, 47(10):2838, 2011. ISSN 1359-7345, 1364-548X. doi: 10.1039/c0cc04526h.
- [45] Jasmina Hafizovic Cavka, Søren Jakobsen, Unni Olsbye, Nathalie Guillou, Carlo Lamberti, Silvia Bordiga, and Karl Petter Lillerud. A New Zirconium Inorganic Building Brick Forming Metal Organic Frameworks with Exceptional Stability. *Journal of the American Chemical Society*, 130(42):13850–13851, October 2008. ISSN 0002-7863. doi: 10.1021/ja8057953.
- [46] Andrew D. Wiersum, Estelle Soubeyrand-Lenoir, Qingyuan Yang, Beatrice Moulin, Vincent Guillerm, Mouna Ben Yahia, Sandrine Bourrelly, Alexandre Vimont, Stuart Miller, Christelle Vagner, Marco Daturi, Guillaume Clet, Christian Serre, Guillaume Maurin, and Philip L. Llewellyn. An Evaluation of UiO-66 for Gas-Based Applications. *Chemistry - An Asian Journal*, 6(12):3270–3280, December 2011. ISSN 18614728. doi: 10.1002/asia.201100201.
- [47] Min Kim, John F Cahill, Yongxuan Su, Kimberly A. Prather, and Seth M Cohen. Postsynthetic ligand exchange as a route to functionalization of ‘inert’ metal–organic frameworks. *Chem. Sci.*, 3(1):126–130, 2012. ISSN 2041-6520. doi: 10.1039/c1sc00394a.
- [48] Lijuan Shen, Weiming Wu, Ruowen Liang, Rui Lin, and Ling Wu. Highly dispersed palladium nanoparticles anchored on UiO-66(NH₂) metal-organic framework as a reusable and dual functional visible-light-driven photocatalyst. *Nanoscale*, 5(19): 9374, 2013. ISSN 2040-3364, 2040-3372. doi: 10.1039/c3nr03153e.
- [49] Sigurd Øien, Giovanni Agostini, Stian Svelle, Elisa Borfecchia, Kirill A. Lomachenko, Lorenzo Mino, Erik Gallo, Silvia Bordiga, Unni Olsbye, Karl Petter Lillerud, and Carlo Lamberti. Probing Reactive Platinum Sites in UiO-67 Zirconium Metal–Organic Frameworks. *Chemistry of Materials*, 27(3):1042–1056, February 2015. ISSN 0897-4756, 1520-5002. doi: 10.1021/cm504362j.
- [50] Hui Wu, Yong Shen Chua, Vaiva Krungleviciute, Madhusudan Tyagi, Ping Chen, Taner Yildirim, and Wei Zhou. Unusual and highly tunable missing-linker defects in zirconium metal-organic framework UiO-66 and their important effects on gas adsorption. *Journal of the American Chemical Society*, 135(28):10525–10532, July 2013. ISSN 00027863. doi: 10.1021/ja404514r.
- [51] Vincent Guillerm, Silvia Gross, Christian Serre, Thomas Devic, Matthias Bauer, and Gérard Férey. A zirconium methacrylate oxocluster as precursor for the low-temperature synthesis of porous zirconium(IV) dicarboxylates. *Chem. Commun.*, 46(5):767–769, 2010. ISSN 1359-7345, 1364-548X. doi: 10.1039/B914919H.

BIBLIOGRAPHY

- [52] Loredana Valenzano, Bartolomeo Civalleri, Sachin Chavan, Silvia Bordiga, Merete H. Nilsen, Søren Jakobsen, Karl Petter Lillerud, and Carlo Lamberti. Disclosing the Complex Structure of UiO-66 Metal Organic Framework: A Synergic Combination of Experiment and Theory. *Chemistry of Materials*, 23(7):1700–1718, April 2011. ISSN 0897-4756. doi: 10.1021/cm1022882.
- [53] Marco Taddei, Russell Jon Wakeham, Athanasios Koutsianos, Enrico Andreoli, and Andrew Ross Barron. Post-synthetic ligand exchange in zirconium-based metal-organic frameworks: Beware of the defects! *Angewandte Chemie International Edition*, July 2018. ISSN 14337851. doi: 10.1002/anie.201806910.
- [54] A. W. Thornton, R. Babarao, A. Jain, F. Trousselet, and F.-X. Coudert. Defects in metal-organic frameworks: A compromise between adsorption and stability? *Dalton Trans.*, 45(10):4352–4359, 2016. ISSN 1477-9226, 1477-9234. doi: 10.1039/C5DT04330A.
- [55] Frederik Vermoortele, Bart Bueken, Gaëlle Le Bars, Ben Van de Voorde, Matthias Vandichel, Kristof Houthoofd, Alexandre Vimont, Marco Daturi, Michel Waroquier, Veronique Van Speybroeck, Christine Kirschhock, and Dirk E. De Vos. Synthesis Modulation as a Tool To Increase the Catalytic Activity of Metal-Organic Frameworks: The Unique Case of UiO-66(Zr). *Journal of the American Chemical Society*, 135(31):11465–11468, August 2013. ISSN 0002-7863, 1520-5126. doi: 10.1021/ja405078u.
- [56] Binbin Tu, Qingqing Pang, Doufeng Wu, Yuna Song, Linhong Weng, and Qiaowei Li. Ordered Vacancies and Their Chemistry in Metal-Organic Frameworks. *Journal of the American Chemical Society*, 136(41):14465–14471, October 2014. ISSN 0002-7863, 1520-5126. doi: 10.1021/ja5063423.
- [57] Greig C. Shearer, Sachin Chavan, Jayashree Ethiraj, Jenny G. Vitillo, Stian Svelle, Unni Olsbye, Carlo Lamberti, Silvia Bordiga, and Karl Petter Lillerud. Tuned to Perfection: Ironing Out the Defects in Metal-Organic Framework UiO-66. *Chemistry of Materials*, 26(14):4068–4071, July 2014. ISSN 0897-4756, 1520-5002. doi: 10.1021/cm501859p.
- [58] Yang Jiao, Yang Liu, Guanghui Zhu, Julian T. Hungerford, Souryaadeep Bhattacharyya, Ryan P. Lively, David S. Sholl, and Krista S. Walton. Heat-Treatment of Defective UiO-66 from Modulated Synthesis: Adsorption and Stability Studies. *The Journal of Physical Chemistry C*, 121(42):23471–23479, October 2017. ISSN 1932-7447, 1932-7455. doi: 10.1021/acs.jpcc.7b07772.
- [59] Ben Van de Voorde, Ivo Stassen, Bart Bueken, Frederik Vermoortele, Dirk De Vos, Rob Ameloot, Jin-Chong Tan, and Thomas D. Bennett. Improving the mechanical stability of zirconium-based metal-organic frameworks by incorporation of acidic modulators. *Journal of Materials Chemistry A*, 3(4):1737–1742, 2015. ISSN 2050-7488, 2050-7496. doi: 10.1039/C4TA06396A.

BIBLIOGRAPHY

- [60] Cesare Atzori, Greig C. Shearer, Lorenzo Maschio, Bartolomeo Civalleri, Francesca Bonino, Carlo Lamberti, Stian Svelle, Karl Petter Lillerud, and Silvia Bordiga. Effect of Benzoic Acid as a Modulator in the Structure of UiO-66: An Experimental and Computational Study. *The Journal of Physical Chemistry C*, 121(17):9312–9324, May 2017. ISSN 1932-7447, 1932-7455. doi: 10.1021/acs.jpcc.7b00483.

4. Exploring the impact of material form on adsorption measurements

4.1. Introduction

An adsorbent cannot be used in an industrial process in its raw powder form. The small crystals which are normally obtained during synthesis are not suited for direct use. Therefore, in order to use a material in a setting such as the beds and columns common in catalysis, PSA (pressure swing adsorption) and TSA (temperature swing adsorption), a structuring into a hierarchically porous structure form is needed.⁽¹⁾

To this end adsorbents are usually shaped into pellets, a process which introduces a range of benefits, such as improved flow regimes, better thermal management and material containment. The shaping process is needed not just for stabilising the small particles, but also to impart the resulting pellet with a high enough mechanical resistance to withstand the stresses imposed by the high flow encountered in an industrial bed. Ideally, forming would have limited effects on the properties of the material. However, this is often not the case, as shaping can change adsorption performance dramatically.

Shaping is therefore a crucial step towards the large-scale use of an adsorbent material. Even for commonplace adsorbents such as carbons and zeolites, the optimum binding additives and the shaping process itself are the subject of extensive research. Often, the procedure is tailored for an individual material and application.

As metal organic frameworks with properties that make them suited for industrial applications emerge, a push towards obtaining shaped versions of the best-performing materials is seen, first for pilot studies and perhaps large scale use.

Due to the wide range of materials, potential shaping methods, binders and effects introduced through the process itself, a high-throughput methodology is often the kind of approach that is best suited to exhaustively explore the result space. The data processing methodologies discussed in chapter 1 combined with thermal methods presented in chapter 2 are put to use in a study on the shaping performance of MOFs.

Chapter summary

After a short introduction to shaping, this chapter explores the variability introduced by an ρ -alumina binder in three topical MOFs: UiO-66(Zr), MIL-100(Fe) and MIL-127(Fe). These MOFs have been selected for their known chemical and thermal stability and well-studied adsorption behaviour. The alumina shaped variant of these MOFs is compared to the original powder material with regard to the adsorption of a series of common

4. Exploring the impact of material form on adsorption measurements

gasses and vapours. Microcalorimetry in conjunction with 8 gas probes has been used to get an in-depth picture of the change in surface energetics. Finally, a previous study on the same materials shaped with a poly-vinyl alcohol (PVA) binder is extended to vapour adsorption and the entire dataset is processed to obtain an overview of the impact of a hydrophobic and a hydrophilic binder on adsorption performance.

Contributions

4.2. Shaping in context

In order to understand the requirement for material forming, we should first examine adsorption from a kinetic, thermal and mechanical standpoint. Until now, in this thesis the isotherms were measured in systems that achieved complete equilibrium between each step, without a mention of experimental duration. However, this parameter is crucial when working with time-dependent systems operating in a flow mode, as columns and beds rarely operate at equilibrium conditions.

The rate of adsorption on the surface of the pore is usually fast, with the controlling step being diffusion of guest molecules between particles (interparticle) and through the pore network (intraparticle).⁽²⁾ Diffusion is dominated by different phenomena depending on the lengthscale involved, from molecular diffusion or Knudsen diffusion in large pores, to concentration gradients and steric effects in micropores. Forced flow regimes dramatically improve interparticle and particle surface diffusion at the cost of the energy required to impose the pressure drop. A balance must be struck to obtain a high overall diffusion coefficient while maintaining a large surface area to volume ratio and a reasonable pressure drop across the column or bed.⁽³⁾

As mentioned in chapter 2, adsorption is an exothermic process, with high amounts of heat being released. Since rates and capacity are dictated by an Arrhenius model with lower adsorption at high temperature, an increase is rarely desired. As with diffusion, fast thermal transfer is therefore needed to prevent a loss in efficiency or, with some materials, a degradation of the adsorbent itself.

Finally, the mechanical resistance of the material used in a bed or column should be considered. The pressure drops used to improve diffusion and heat transfer through high flow regimes may lead to attrition and breakage of the adsorbent structure. Often in tall columns, the weight of the material itself can be a factor that leads to structural collapse.

The requirements discussed above, lead to the necessity of adsorbent forming or shaping. The process generates a hierarchical pore size distribution which helps with reducing pressure drop, as can be seen in Figure 4.1. The addition of binders or other additives improves the mechanical and thermal properties of the final shape. Depending on the application, many types of shaped materials exist, from simple granules and pellets, to extruded rods, monoliths and membranes. The process itself consists of extrusion of the particle-binder slurry and then hardening either through temperature, cross-linking or chemical treatment. Other methods, such as spray-drying or granulation can similarly

4. Exploring the impact of material form on adsorption measurements

be used.⁽⁴⁾ While the basic steps are the same: the mixing of the powder with any additives, the shaping in their required form and curing of the final structure, many variations are possible in each step.

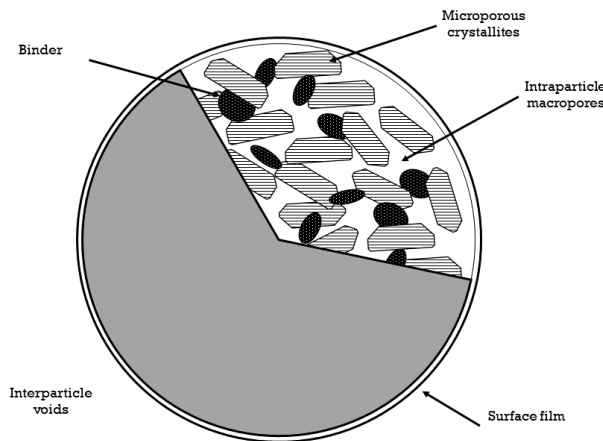


Figure 4.1.: An schematic representation of the possible structure of a shaped sphere.

The binders, as their name imply, serve to hold crystals together during and after the shaping process. For carbons, binders such as pitch, polymers (CMC, PVA) or even non-porous carbon black are commonly used.⁽⁵⁾ For zeolites, inorganic binders are more prevalent, with silica, alumina and clay binders common in industry. Often, a combination of additives is used, each with a different task during the pelletization process⁽⁶⁾ such as improving rheological behaviour. It has been shown^(7,8) that the choice of binder can introduce large property variations, ranging from loss of porosity and structure to the enhancement of the desired reactivity and selectivity through changes in the acid site density or ion migration.

Overall, during shaping the capacity per mass of pellet is expected to decrease due to the addition of a non-porous component, but the difference should be small and should not arise due to effects such as pore blocking or pore filling with the binder material. Furthermore, a densification effect is expected, leading to better performance on a volume basis. Finally, binder addition should not influence the chemical properties of the adsorbent, and preserve the original interactions with the adsorbate. With a judicious choice of binding material, the resulting pellet may even outperform the powder.

When it comes to MOFs, shaping has been attempted with a wide range of binders and methods. Methods such as granulation, spray-drying or extrusion have all been successfully employed to create MOF pellets.⁽⁹⁾ Monoliths have also been shown to be an effective way for shaping purposes, either through impregnation⁽¹⁰⁾ or through support on alumina.⁽¹¹⁾ Surprisingly, compression⁽¹²⁾ or even simple air drying of MOF slurries⁽¹³⁾ have also shown good results. Note that the monolith prepared through the latter method had a three times larger volumetric specific surface area than the conventional powder.

4. Exploring the impact of material form on adsorption measurements

The connection between MOF and binder is also of crucial importance. The MOF-polymer interface has been shown⁽¹⁴⁾ to be subject to a complex interplay of interactions between the organic chains and the crystal surfaces. These effects can be striking enough to warrant further research into MOF-polymer hybrids⁽¹⁵⁾, with the aim of combining the unique attributes of both materials.

Previous work from MADIREL⁽¹⁶⁾ has analysed the impact of polyvinyl alcohol (PVA) shaping on a series of MOFs. It was shown that the binder did introduce some specific effects, such as a protection effect on the reduction of Fe^{3+} to Fe^{2+} in MIL-127(Fe), as well as a curious gating effect seen on butane adsorption on MIL-100(Fe), likely due to polymer chains covering pore entrances. Otherwise, the shaping imparted good performance to the shaped samples, with almost no capacity loss on a mass basis. Unfortunately, the use of a polymer limited the activation temperature of the samples to a maximum of 150 °C.

4.3. Materials, shaping and characterisation methods

4.3.1. Materials

In this chapter we have selected the same series of “topical” MOFs and have investigated the influence of a different shaping method, namely the use of alumina binder, on their adsorption properties.

The UiO-66(Zr) MOF and its derivatives are well known due to their stability, both in regards to temperature and chemical compounds⁽¹⁷⁾ and has been discussed in detail in chapter 3. It is composed of Zr6-oxo clusters which are connected with benzene dicarboxilate (BDC) linkers to form a face-centered cubic framework. It has shown promise⁽¹⁸⁾ in use for gas adsorption applications. It contains a three-dimensional arrangement of micropores with each centric octahedral cage surrounded by eight corner tetrahedral cages (diameters of approximately 11 Å and 28 Å respectively) and connected through narrow triangular windows of approximately 6 Å.

MIL-100(Fe) is a MOF which uses the benzene tricarboxilate (BTC) linker in conjunction with trimeric iron (III) octahedral clusters.^(19,20) The framework assembles in hybrid supertetrahedra which leads to very large pores: a 25 Å cage and a larger, 29 Å cage. These pore cages are accessible through windows of 5.5 Å and 8.6 Å respectively. The iron trimers are coordinated with anions and have shown a propensity to partially reduce to a divalent Fe^{2+} state, exposing a naked metal site in the process.⁽²¹⁾

The last material, MIL-127(Fe), originally reported by Liu et al. is a MOF built from the same metal (III) octahedra trimers as MIL-100(Fe), but using the 3,3',5,5'-azobzenenetetracarboxylate (TazBz) linker, to produce a framework with the **soc** topology. This material has shown promise⁽²³⁾ for large scale synthesis. Furthermore, due to its alternating hydrophobic/hydrophilic microporous system, it has been shown to be of interest for multiple applications such as catalysis or CO_2 capture.⁽²⁴⁾

The UiO-66(Zr) and MIL-100(Fe) powders have been synthesised at the Korea Research Institute of Chemical Technology (KRICT). The MIL-127(Fe) MOF was made in

4. Exploring the impact of material form on adsorption measurements

the group of Christian Serre, in the Lavoisier Institute in Versailles. Complete details of the synthesis method can be found in the related publication⁽²⁵⁾ and in Appendix B. The structures of the three materials can be seen in Figure 4.2.

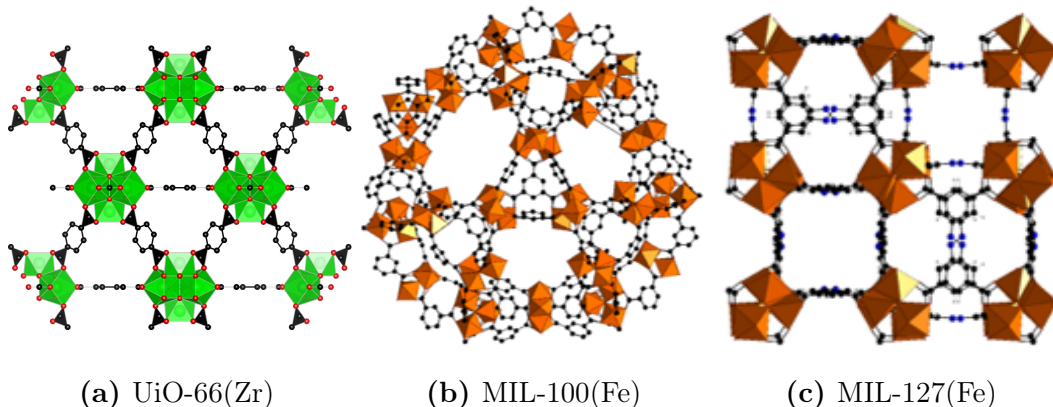


Figure 4.2.: The unit structures of the investigated MOFs. The colour coding is as follows: Zr polyhedra in green, Fe octahedra in brown, C in black, O in red, N in blue. Hydrogen atoms are omitted for clarity.

4.3.2. Shaping Procedure

The shaping of the samples also took place at KRICT and was done using a wet granulation method. In the case of the alumina binder, the MOF powder was mixed with the previously prepared mesoporous ρ -alumina with water added as the dispersing medium. For the PVA binder, the MOF powder was instead added to a solution of ethanol solution containing a polymer mixture of polyvinyl groups such as polyvinyl alcohol and polyvinyl butyral. The resulting mixture was shaped into beads using a hand-made pan granulator. During the process, the spheres were sprayed with the respective solvent in order to achieve desired size. The beads were then sieved and rolled using a roller machine to enhance their spherical shape. Finally, the prepared samples were dried at 303K for 12h to remove all residual solvent. The resulting beads were near spherical in shape, with a diameter between 2 mm to 2.5 mm.

4.3.3. Characterisation of powders and pellets

The primary interest of the study was observing differences in adsorption properties between the powder and the shaped materials.

Thermogravimetric analysis was used to verify that the binder did not change the thermal stability of the materials and, in the case of the PVA variant, to ensure that the activation temperature chosen did not induce polymer decomposition. The TGA method is described in detail in Appendix A.1.

The bulk and skeletal density of the powder and pellets were measured to allow isotherms to be presented on a volume basis, as well as to check the level of densification

4. Exploring the impact of material form on adsorption measurements

afforded through the shaping process. The procedure is described in Appendix A.2 and Appendix A.3.

Specific surface area and pore volume were determined through nitrogen adsorption at 77 K. These measurements were recorded according to the method in Appendix A.4. For inspecting changes in surface hydrophobicity, water and methanol adsorption isotherms were measured according to the method presented in Appendix A.5.

Finally, all calorimetry data was recorded using a high sensitivity Tian-Calvet calorimeter coupled with adsorption volumetry, as introduced in chapter 2.

4.3.4. Sample activation for adsorption

The materials were pre-treated before all adsorption experiments by activation at high temperature under secondary vacuum for 16 hours. The activation temperature was specific to each solid: 200 °C for UiO-66(Zr), 150 °C for MIL-100(Fe) and 150 °C for MIL-127(Fe).

4.4. Results and discussion

4.4.1. Thermal stability

In order to check if the shaped samples have not undergone bulk structural changes, as well as find a suitable activation temperature, the powder and shaped samples underwent thermogravimetric analysis under an argon atmosphere.

The process of shaping did not have any impact on the thermal stability of the investigated MOFs, as evidenced by the TGA curves in Figure 4.3. The primary mass loss occurs in a 10 °C range for all powder-pellet pairs. Shaped samples are also seen to have a smaller mass loss at high temperatures. This is expected, as after the addition of temperature inert alumina, the MOF makes up a lower percentage of the material.

4.4.2. Adsorption isotherms at 77K and room temperature

Nitrogen sorption isotherms measured at 77 K have been measured on both powder and ρ -alumina pellets, with the isotherms presented in Figure 4.4. Observation of the physisorption curves sheds light on the impact of the alumina binder on the materials chosen. The shapes of all isotherms are visually similar, with the pellet curves shifted downwards due to the aforementioned structure degradation. In both powders and pellets, the increased uptake after $0.9 p/p^0$ is a sign of condensation in very large pores or voids, which can be attributed to intra-pellet spaces and crystal agglomeration. In the MIL-127(Fe) pellets, a narrow hysteresis curve is seen, which closes at a p/p^0 of 0.5. This curve corresponds to capillary condensation in a pore size of around 4 nm. This pore width is too small to be a sign of inter-pellet voids and therefore must be a consequence of the shaping process.

4. Exploring the impact of material form on adsorption measurements

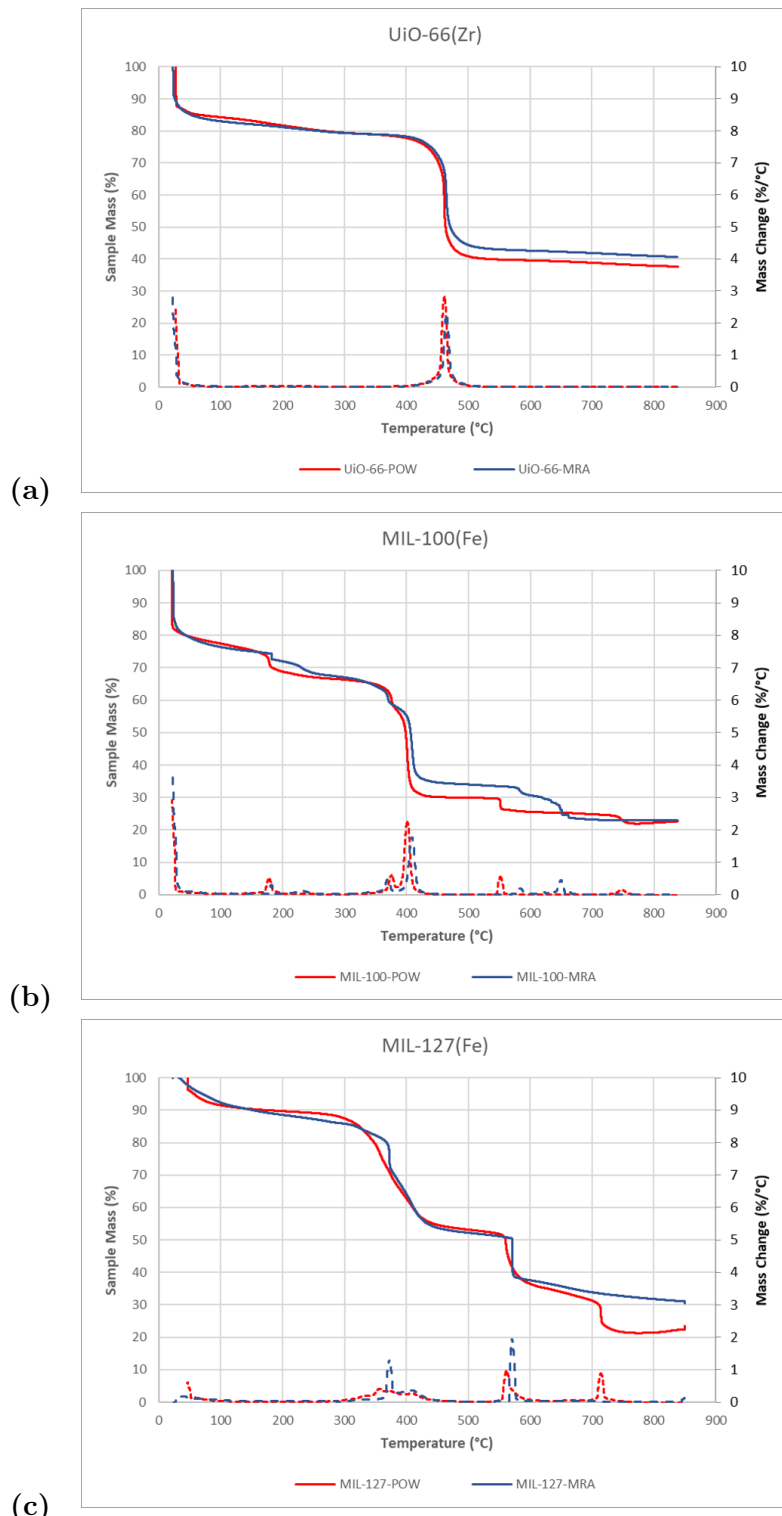


Figure 4.3.: High resolution TGA curves recorded under argon on (a) UiO-66(Zr), (b) MIL-100(Fe) and (c) MIL-127(Fe). The original powders are depicted in red and the shaped material in blue.

4. Exploring the impact of material form on adsorption measurements

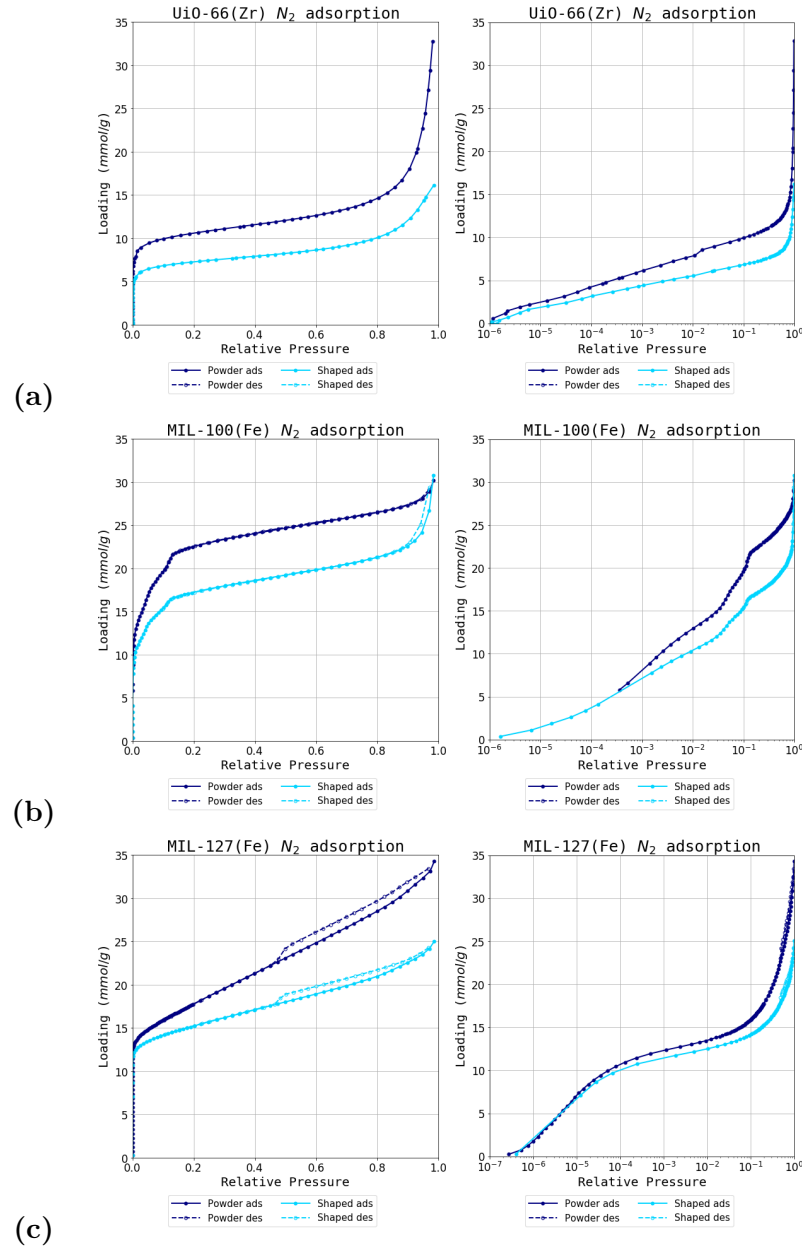


Figure 4.4.: Nitrogen isotherms at 77K for (a) UiO-66(Zr), (b) MIL-100(Fe) and (c) MIL-127(Fe). The powder sample is in light blue while the ρ -alumina sample in dark blue. Logarithmic graphs of the isotherms are on the right for clarity of the low pressure region.

4. Exploring the impact of material form on adsorption measurements

While no other significant features are visible on the isotherms themselves, we use pyGAPS to further process them and obtain properties such as specific surface area, calculated through the BET method and pore volume, calculated as the volume of nitrogen adsorbed at a p/p^0 of 0.2. As the surface area of the binder is lower than the one of the MOF, a drop in both these properties is expected. The calculated values are shown in Table 4.1.

Table 4.1.: Properties of the studied powders and pellets

MOF	form	BET surface area (m^2/g)	Pore volume (cm^3/g)	Bulk density (kg/m^3)
UiO-66(Zr)	powder	903	0.38	0.319
	ρ -alumina	619	0.24	0.472
MIL-100(Fe)	powder	1928	0.78	0.216
	ρ -alumina	1451	0.60	0.351
MIL-127(Fe)	powder	1413	0.76	0.412
	ρ -alumina	1266	0.56	0.526

As predicted, the specific surface area of the shaped samples is decreased compared to the corresponding powder. While in the case of MIL-127(Fe) the BET area is only 10% lower, for the MIL-100(Fe) and UiO-66(Zr) materials a larger drop is seen, of 25% and 31%, respectively. A similar decrease can be seen in pore volume, with a 36%, 23% and x% loss seen in UiO-66(Zr), MIL-100(Fe) and MIL-127(Fe) respectively. The decrease in both surface area and micropore volume is too large for it to be a consequence of the presence of non-porous binder. It is therefore theorised that some structure degradation must have occurred during the pelletisation process. Despite a loss in surface area, the bulk density of the material has increased, due to crystal aggregation.

4.4.3. Room temperature gas adsorption and microcalorimetry

As previously shown, combining microcalorimetry with adsorption manometry can give an insight into the energetics of the adsorption process by directly measuring differential heat. Even though the different contributions to the overall enthalpy curve cannot be decoupled from the individual sources, such as guest-host interactions or fluid-fluid interactions, it can be successfully applied to observing the effect of a process or treatment such as shaping on the properties of a MOF.

Eight probe gasses have been chosen for adsorption at 303 K: N₂, CO, CO₂, CH₄, C₂H₆, C₃H₆, C₃H₈ and C₄H₁₀. The range of adsorbates chosen allows different effects to be investigated. The adsorption of saturated hydrocarbons with an increasing carbon number (C1-C4) can be assumed to be driven strictly by Van-der-Waals forces, due to the shielding effects of the hydrogen atoms. Differences in the maximum uptakes of these gasses will point to loss of porosity or crystallinity. A capacity loss with an increasing carbon number will point to size exclusion effects induced by the binder, such as particle

4. Exploring the impact of material form on adsorption measurements

coating, pore filling or pore obstruction. The other probes have been chosen for their properties which can shine light on other specific interaction types present during the adsorption. Carbon monoxide is a slightly dipolar molecule which has the ability to act as an with other charges in the pores. It also can highlight CUS (coordinatively unsaturated sites) generated through defects, reduction or open metal sites due to its propensity for π backbonding coordination. This electron transfer process can also result in complexation with molecular orbitals in systems with π bonds such as alkenes and alkynes. Propylene is used as an unsaturated hydrocarbon probe gas for this purpose. Carbon dioxide is a highly quadrupolar molecule which will be strongly adsorbed in polar pore environments. Changes in the adsorption behaviour of CO₂ will shed light on such surface changes and can even be used as a predictor of hydrophobicity.⁽²⁴⁾ Finally, N₂ is a staple adsorbent for material characterisation when used at 77 K. The molecule is a slight quadrupole and has also been shown to chelate to some transitional metals in an analogue fashion to CO.

To eliminate the influence of kinetic and diffusion effects on the experiments, care has been taken to allow time for complete equilibration of both pressure and calorimeter signal. The complete dataset of adsorption isotherms, in the basis of both mass and volume can be found in Appendix C.

After collecting the combined isotherm and enthalpy data, three indicators have been chosen to best represent the effects of shaping: initial enthalpy of adsorption, initial Henry constant and maximum capacity. These numeric performance indicators have been calculated using the available functionality in pyGAPS.

The initial enthalpy of adsorption extrapolated at zero coverage is a measure of the interaction with highest energetic sites on the MOF surface. Conversely, the initial Henry constant (K_{Hi}), here obtained through fitting the virial adsorption model through the method in section 1.3.1, is also an indication of adsorption in the pores before any layering or adsorbate-adsorbate interaction comes into effect. The last indicator, maximum capacity, was taken as the loading attained when the isotherm reached a plateau. In the case of probes where the plateau was outside the range of pressure of the instrumentation (>50 bar), the loading at the highest available pressure was considered as a suitable approximation. The three key performance indicators (KPIs) have then been compared side by side on both the powder and shaped samples.

UiO-66(Zr)

A visual inspection of the enthalpy curves on as-synthesised UiO-66(Zr) show it to be relatively homogenous, with flat profiles being common. This is typical of this MOF, which has a pore environment without high energy adsorption sites.⁽¹⁸⁾ Both CO₂ and CO show a higher enthalpy of adsorption at low loadings, as seen in Figure 4.6, which is likely due to their quadrupole and dipole interaction, respectively.

The KPI graphs in Figure 4.5 show very similar values for both Henry's constant and initial enthalpy of adsorption. It is therefore apparent that the shaping process did not change the interaction of the adsorbate with the MOF surface.

The maximum capacity graphs show a more interesting trend. When using small

4. Exploring the impact of material form on adsorption measurements

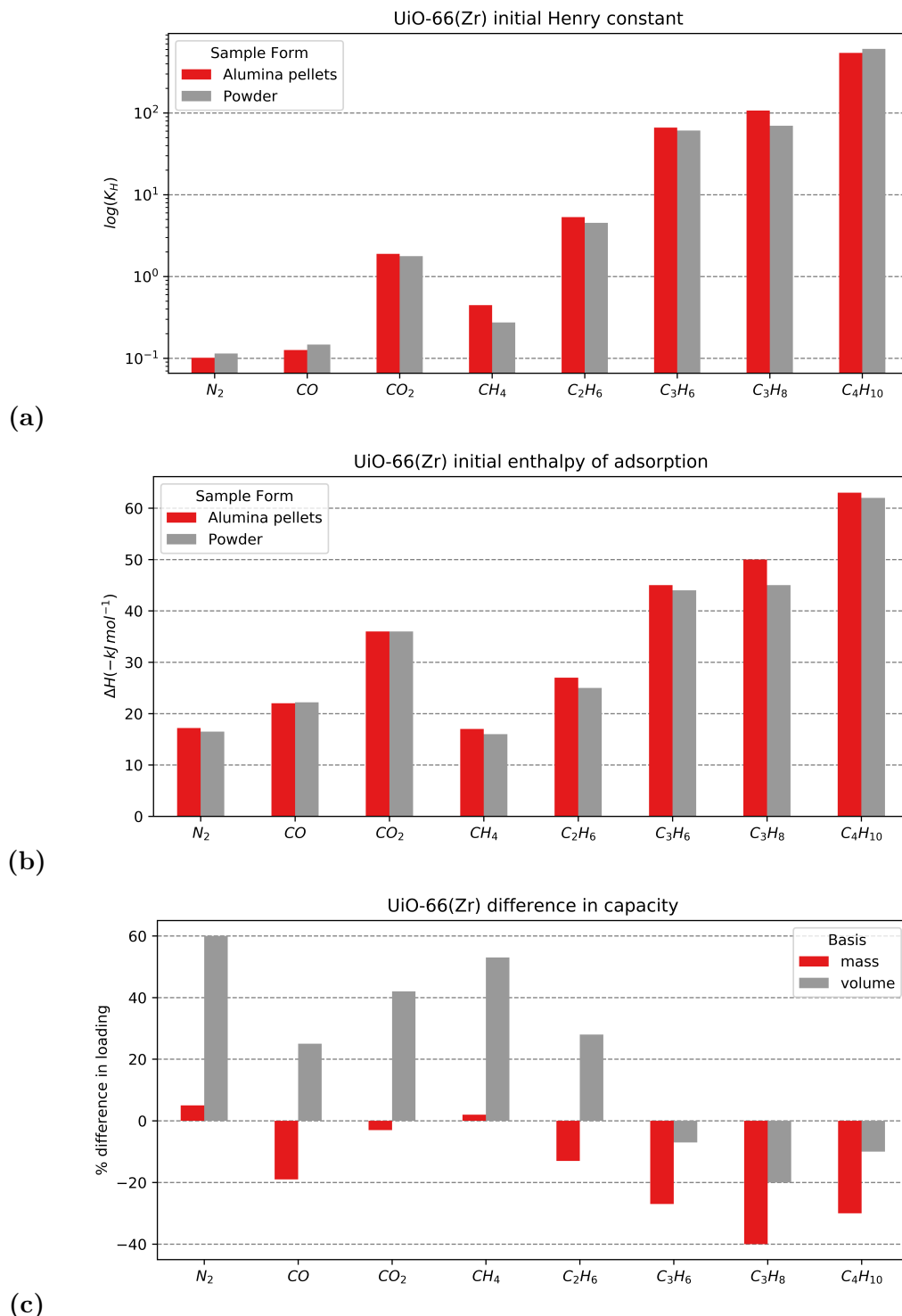


Figure 4.5.: KPIs extracted from the UiO-66(Zr) adsorption dataset with (a) logarithmic initial Henry constant (b) initial enthalpy of adsorption and (c) change in adsorption maximum capacity from the powder to the alumina shaped version on a mass and volume basis in red and grey respectively

4. Exploring the impact of material form on adsorption measurements

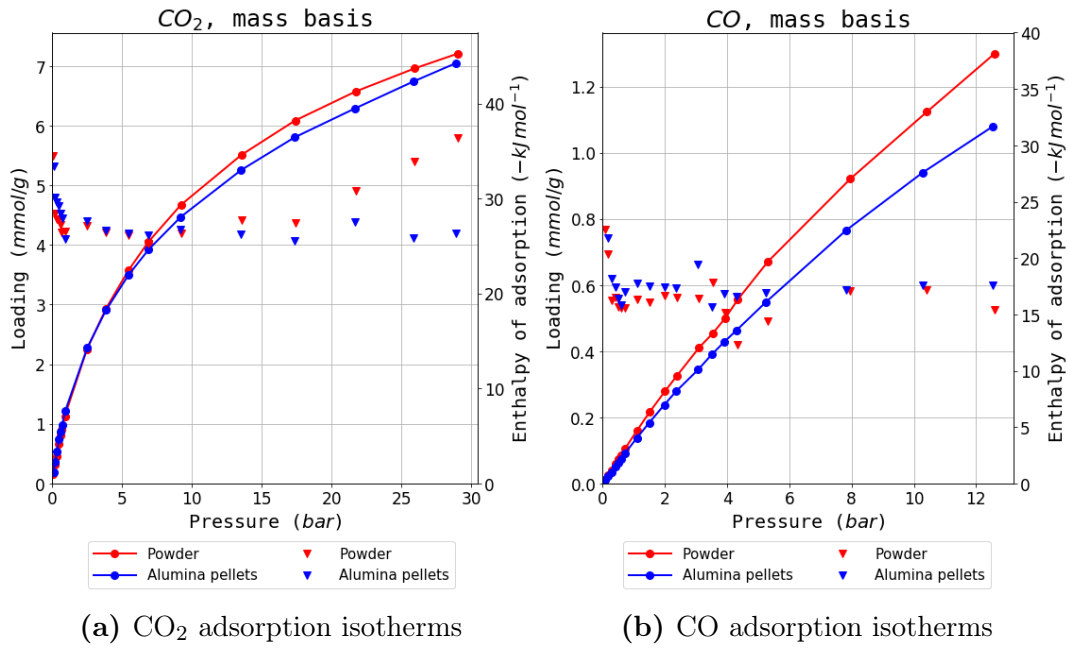


Figure 4.6.: Selected isotherms from the UiO-66(Zr) dataset

adsorbates such as N₂, CO₂ and CH₄, the shaped samples have a similar performance on a mass basis and, due to the densification process, better capacities on a volume basis. Starting with ethane, the maximum capacity difference starts to increase, with lower performance as molecule size increases. On hydrocarbons with a carbon number of 3 and 4, both mass basis and volume basis capacity is decreased compared to the original powder. This size exclusion effect could be explained by the coating of crystal surfaces with the alumina binder.

It could also be argued that instead of size exclusion, the effect is due to an overall decrease in pore volume, and that the isotherms of the low molecular weight gasses will diverge at higher pressures as the pores are filled. A counterargument for this hypothesis is that in the case of CO₂, the plateau is reached with no differences between the powder and the pellet as seen in Figure 4.6a.

Carbon monoxide is an apparent outlier to this trend, with a decreased maximum capacity and a small molecular size. However, when looking at the isotherms directly (Figure 4.6b) it is obvious that the effect is likely to be due to experimental errors, considering the low amount adsorbed and the good overlap in the enthalpy curves.

Overall, the shaping performance of UiO-66(Zr) is reasonable, as long as only small adsorbates are used.

MIL-100(Fe)

The enthalpy profiles on the MIL-100(Fe) powder are less homogenous than the ones on UiO-66(Zr). Some effects can be seen with probes which can interact with the partially reduced Fe(II) atom, such as carbon monoxide and propylene (Figure 4.7). Indeed, when

4. Exploring the impact of material form on adsorption measurements

comparing both the initial Henry constants and enthalpy of adsorption, for CO and C₃H₆, these are higher than the values obtained on UiO-66(Zr). With initial enthalpy of adsorption for CO of around 45 kJ mol⁻¹, the value falls into the range of previous⁽²¹⁾ results for interactions with such Fe(II) CUS.

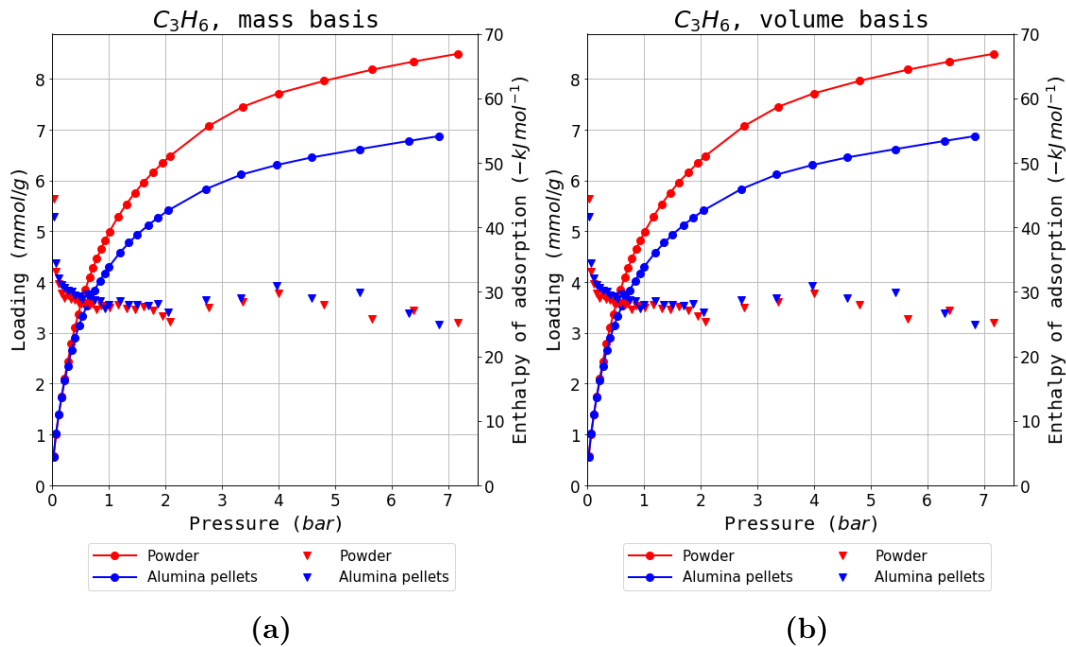


Figure 4.7.: Propylene isotherms on MIL-100(Fe) on a (a) mass and (b) volume adsorbent basis.

Comparing the powder and shaped variants, there are no apparent differences between the two. The only discrepancy, which can be seen on the nitrogen initial K_H follows as a result of an ill-fitting virial parameter, and can be assumed an error after observing the isotherm overlap directly. It could be theorised that by activation at a higher temperature (250 °C), the percentage of iron trimers which would undergo reduction will increase and a further interaction could be observed. However, the activation temperature was chosen to allow comparisons with the PVA study⁽¹⁶⁾, where temperatures over 180 °C would lead to the burn-off of the polymer binder.

The maximum loading differences (Figure 4.8c) of MIL-100(Fe) show a very similar behaviour. On all probes tested, a fixed capacity loss of between 10-20% can be seen on a mass basis. However, the increase in density afforded by the compression during pelletisation leads to a compensation in performance as can be seen directly when looking at isotherms on mass and volume material basis in Figure 4.7a and Figure 4.7b respectively.

We can conclude that MIL-100(Fe) is almost unaffected by alumina shaping. A slight loss in maximum capacity on a mass basis is compensated by a pronounced densification, which is desirable in an industrial setting.

4. Exploring the impact of material form on adsorption measurements

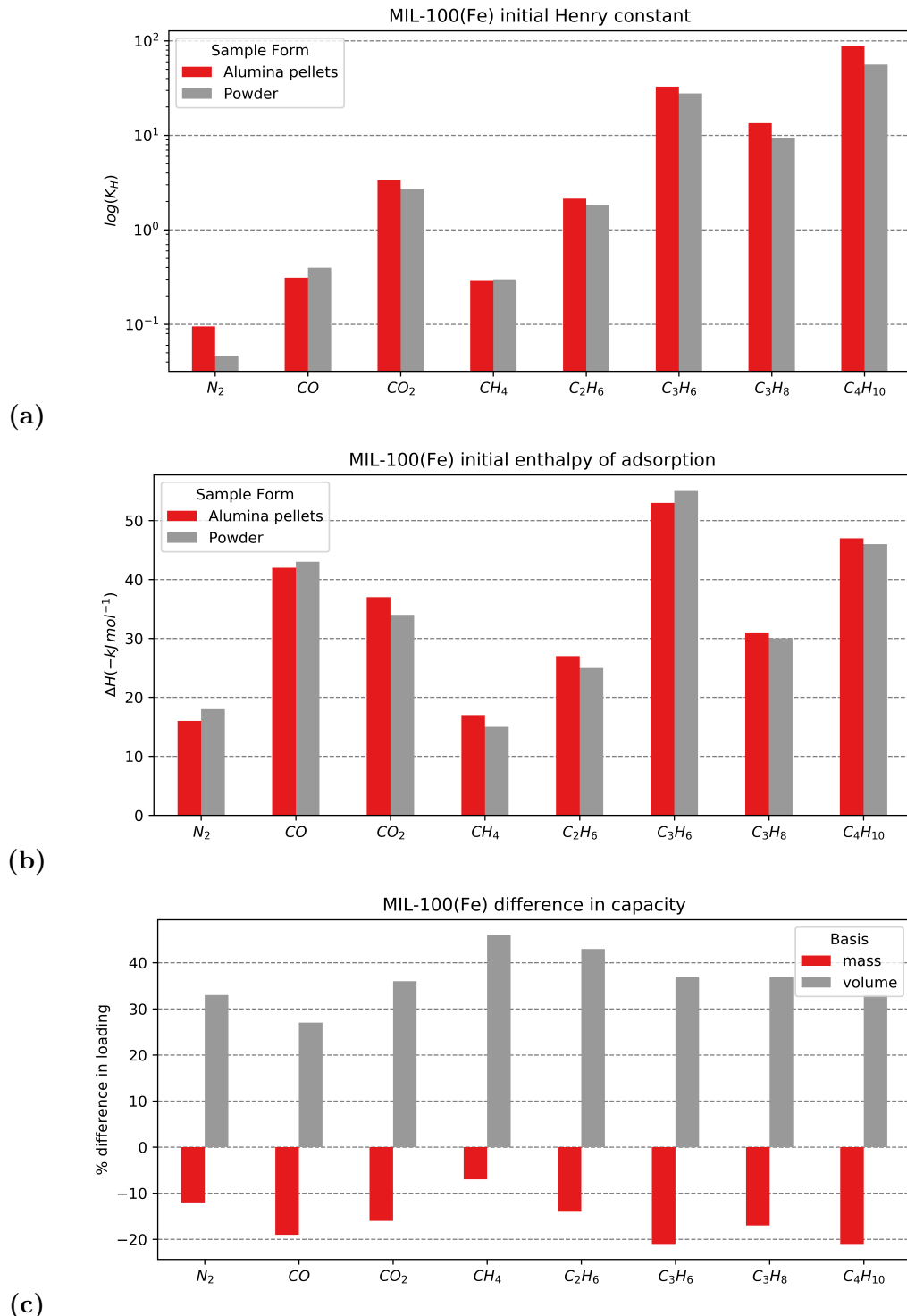


Figure 4.8.: KPIs extracted from the MIL-100(Fe) adsorption dataset with (a) logarithmic initial Henry constant (b) initial enthalpy of adsorption and (c) change in adsorption maximum capacity from the powder to the alumina shaped version on a mass and volume basis in red and grey respectively

MIL-127(Fe)

The isotherms on the original powder form of MIL-127(Fe) should show similar behaviour as on MIL-100(Fe), due to the presence of the same iron trimesate moieties, although with a sharper uptake as a result of the smaller pores. Enthalpy profiles are also influenced by the similar interactions with the iron CUS leading to higher initial heats of adsorption on CO and C₃H₆. An overall increase in the heat of adsorption at higher loadings is seen throughout the probe series, as seen for example on butane in Figure 4.10a. Due to the bimodal pore distribution in the MIL-127(Fe) structure, it is likely that adsorption first commences in the small ($\sim 6 \text{ \AA}$) channels and then, at higher pressures, intrusion into the larger cage-type pores is possible through the $\sim 3 \text{ \AA}$ narrow apertures. The confined cages have an increased interaction with the molecule which leads to the higher enthalpy values.

When comparing the powder and the pellet variant with respect to initial Henry's constant, a large difference in K_H on CO stands out. The value of the initial enthalpy of adsorption does not follow the same pattern. However, visual inspection of the enthalpy curve in Figure 4.10b shows that the energy of adsorption corresponding to interactions with the more active sites is maintained for a larger percentage of the total coverage. This points to the higher preponderance of such sites in the powder variant. A similar offset can be seen in the propylene enthalpy at very low pressures, but this is not reflected in the shape of the isotherm. The weaker complexation strength and the larger size of the molecule likely limits the effect seen in the carbon monoxide isotherm. As for the underlying reason behind the isotherm divergence, it could be that the alumina binder acts as protection against the generation of iron (II) during thermal activation. No other differences are seen between the two forms on either Henry constant and initial enthalpy of adsorption.

The capacity comparison in Figure 4.9c paints an interesting picture. For most probes there is no change in maximum loading showing that there is no structure degradation or pore filling. Two outliers are apparent: carbon monoxide and butane. The decrease in capacity on CO can be explained through the aforementioned changes in active site prevalence. The drop in butane cannot be a consequence of the same effect as there is a perfect overlap in the enthalpy curves as seen in Figure 4.10a. Therefore it likely better explained through a size exclusion effect as seen on UiO-66(Zr).

Overall, MIL-127(Fe) shows excellent performance when undergoing alumina shaping, with almost no capacity loss, as long as carbon monoxide or butane adsorption are required, where specific effects come into play.

4.4.4. Vapour adsorption

The effects of shaping with ρ -alumina are so far more subtle than the changes encountered when using PVA, as shown in the corresponding study.⁽¹⁶⁾ As such we extended the characterisation using adsorption of vapours at room temperature. The influence of the binder on hydrophobic character of the material may be of interest for tuning the properties of the beads. Here, water and methanol can serve as probes for small

4. Exploring the impact of material form on adsorption measurements

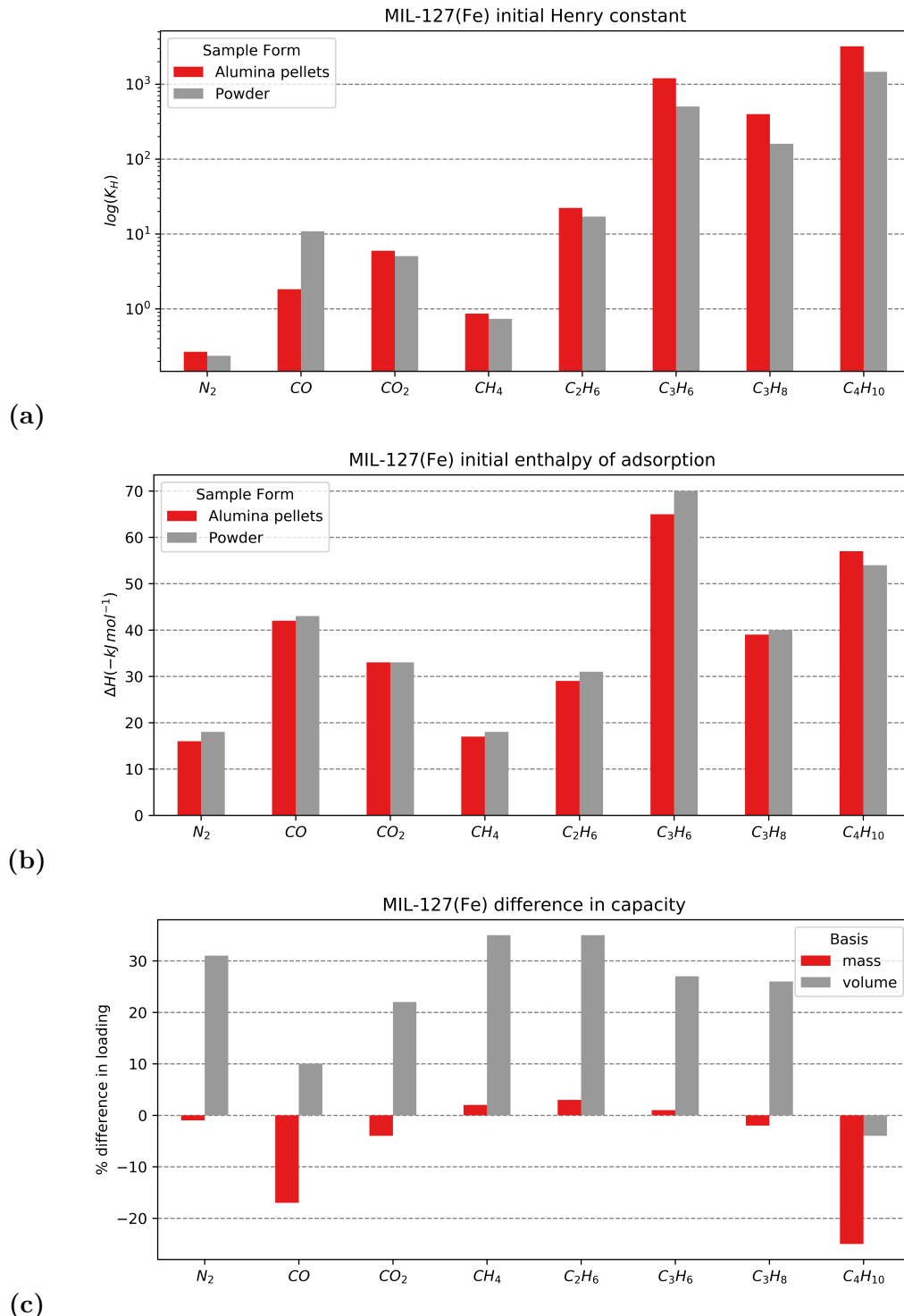


Figure 4.9.: KPIs extracted from the MIL-127(Fe) adsorption dataset with (a) logarithmic initial Henry constant (b) initial enthalpy of adsorption and (c) change in adsorption maximum capacity from the powder to the alumina shaped version on a mass and volume basis in red and grey respectively

4. Exploring the impact of material form on adsorption measurements

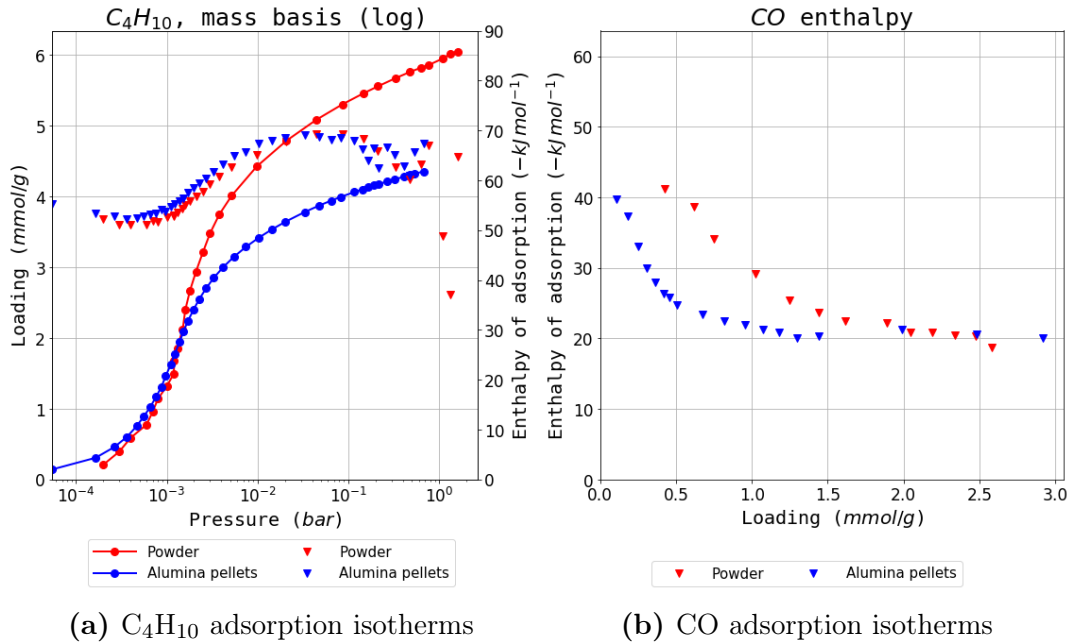


Figure 4.10.: Selected isotherms from the MIL-127(Fe) dataset

changes in surface properties. To this end, the same PVA samples which were used in the previous study were investigated alongside the MRA-shaped MOF.

Due to its surface charges, alumina is a hydrophilic substance, with a contact angle of 10° . It is expected that its addition may therefore increase the affinity of the resulting pellet towards water. On the other hand, the PVA binder is more hydrophobic, with a water contact angle of 51° . The medium affinity for water is due to the surface hydroxyl functionalizations, which can lead to hydrogen bonding.

Two indicators may highlight changes in material hydrophilicity: the slope of the isotherm in the low relative pressure region ($p/p^0 < 0.3$) and condensation steps in the isotherm. Adsorption at low pressures is representative of the initial interactions with the surface, as discussed in the previous section. The pressure at which condensation occurs in the pores of the material, underlined by a sharp increase in the isotherm, depends on the size of the pore but also on pore environment and guest-guest interactions. Finally, hysteresis in the adsorption isotherm may also be an indication of the nature of pores.

The measured isotherms on water and methanol can be found in Figure 4.12 and Figure 4.13 respectively. Initial Henry constants have been calculated for the isotherms using the initial point method, and are displayed in Figure 4.11.

UiO-66(Zr)

On the parent UiO-66(Zr), the water isotherm shows a slow uptake at the start, indicating a hydrophobic surface, and then shows a small step at $p/p^0 = 0.3$. While little is adsorbed on the MOF before this step, its presence at a low relative humidity is indicative of intrinsic defects in the framework.⁽²⁶⁾ Complete saturation takes place

4. Exploring the impact of material form on adsorption measurements

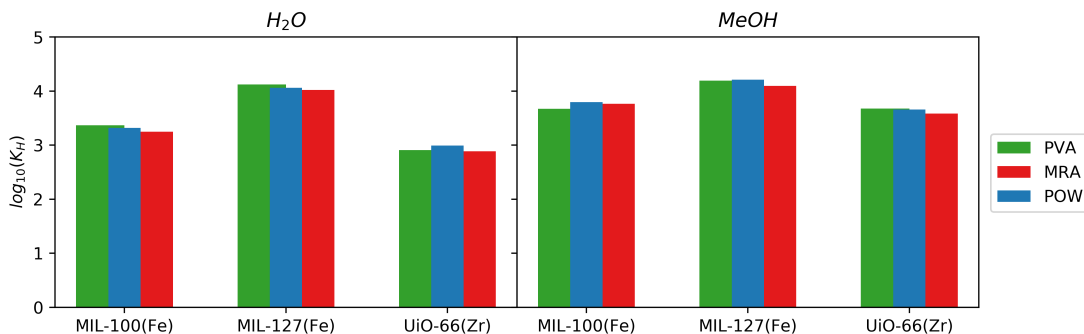


Figure 4.11.: Calculated initial Henry constant for the vapour adsorption isotherms in Figure 4.12 and Figure 4.13

around $p/p^0 = 0.9$. A wide hysteresis curve can be seen, which does not fully close, even at low pressures. Both the saturation step and the condensation may be attributed to agglomeration of crystals and interparticle voids.

The methanol isotherm has the same features as the water one, with the condensation step shifted at a much lower partial pressure ($10^{-1}p/p^0$). It is likely that the organic component of methanol interacts with the hydrophobic surface, thus permitting pore filling at lower pressures. This is also evidenced through the higher Henry constant when compared to water.

When comparing the powder and the pellet variants, the general shape of the isotherm remains the same with both water and methanol. Initial interactions with the surface are also identical, as evidenced by the overlap in the low pressure region and through the calculated Henry constants. The isotherms begin to diverge after the condensation step, where the maximum loading evolves in the order MRA < powder < PVA for both vapours. This is a surprising trend, as both pellets have been shown to have lower capacities than the powder, stemming from material amorphization during granulation. The addition of hydrophilic alumina conforms to this hypothesis, and appears to have no impact on the initial interaction with the surface. On the other hand, polymer-shaped particles seem to have a higher maximum capacity than both powder and alumina pellets. It is unclear if this effect is due to a cooperative effect of hydrogen bonding with hydroxyl groups on the polymer chains or has another underlying cause.

MIL-100(Fe)

The water isotherm on the powder MIL-100(Fe) material show a more hydrophilic environment, with a higher initial uptake, and two condensation steps at $p/p^0 = 0.3$ and $p/p^0 = 0.5$. At low pressures, adsorption takes place on metal sites in the large cages, with clusters formed around these hydrophilic sites. The two steps correspond to the successive filling of the 25 Å and the 29 Å pores. The adsorption and desorption branches show a hysteresis loop formation, associated with the condensation in the largest mesoporous spherical pore.

technically it is not an apples to apples comparison as the alumina and pva pellets had different starting materials...

4. Exploring the impact of material form on adsorption measurements

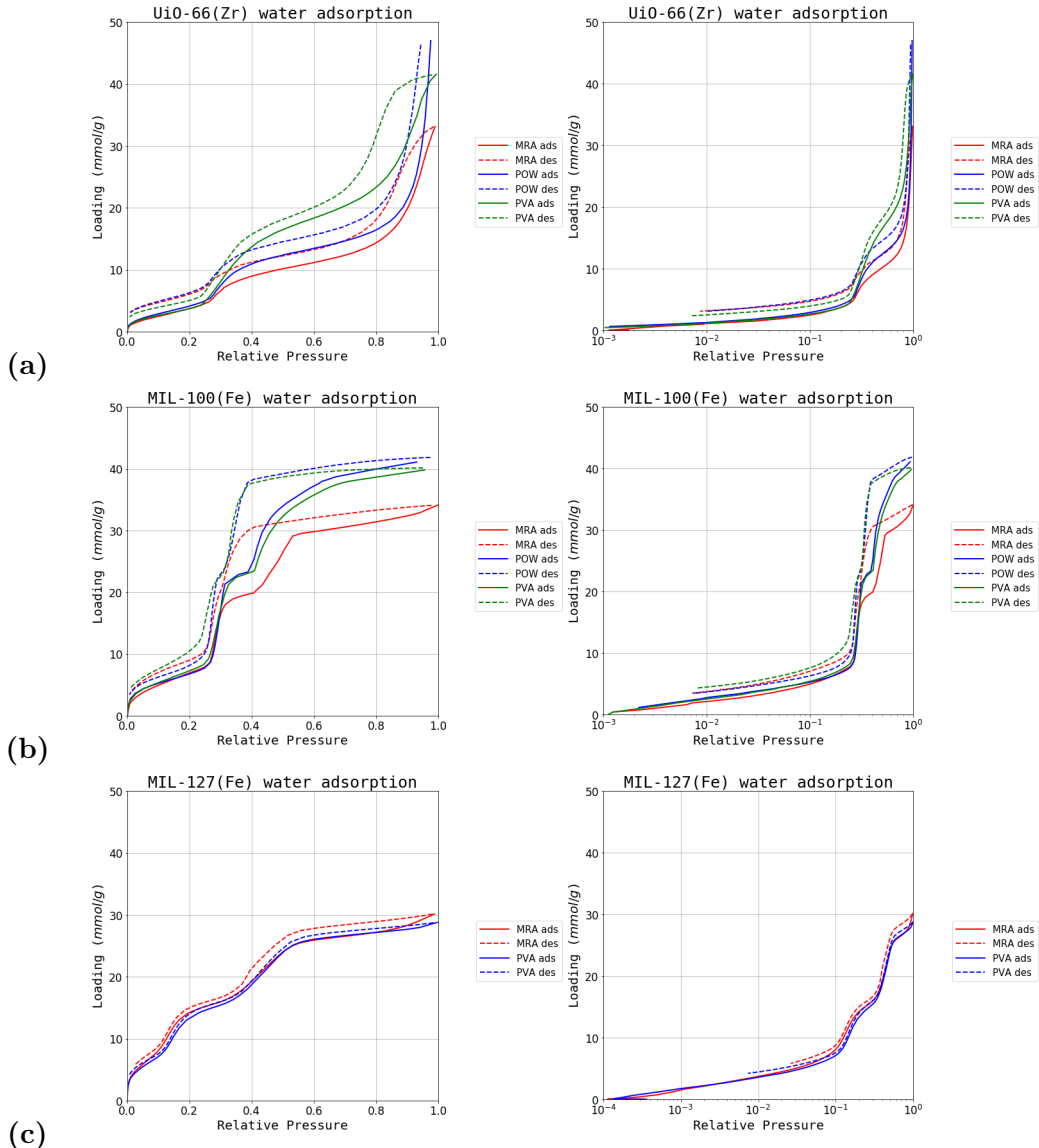


Figure 4.12.: Water adsorption isotherms (a) UiO-66(Zr), (b) MIL-100(Fe) and (c) MIL-127(Fe). The powder samples are in light blue, while the ρ -alumina and poly-vinyl alcohol samples are in red and dark blue respectively. Logarithmic graphs of the isotherms are on the right for clarity of the low pressure region.

4. Exploring the impact of material form on adsorption measurements

The methanol isotherm on the same parent MOF still presents two condensation steps, which have been shifted at to lower pressure. There is no longer any hysteresis present, an indication that the critical pore radius for its formation is not attained when using methanol.

If comparing the powder isotherms with their shaped counterparts, no differences in features are visible. Initial Henry's constant is similar with all

MIL-127(Fe)

On the last MOF powder, the water isotherm shows a hydrophilic surface, with a highest initial slope out of the three materials studied. The isotherm has two condensation steps, a low relative humidity one at 0.15 p/p^0 , which corresponds to the filling of the hydrophilic pore, and a condensation step situated at 0.5 p/p^0 inside the hydrophobic micropore. No hysteresis is observed.

As a striking difference from water behaviour, methanol adsorption leads to completely filled pores at below 0.15 relative pressure. By examining the logarithmic isotherms in Figure 4.13c a steep slope at low pressures is evident. It is likely that the larger size of the methanol molecule is much more affected by confinement in the hydrophilic pore, and leads to sudden micropore filling. The same effect, combined with the increased affinity for the organic part of the probe is likely responsible for shifting the secondary condensation step at lower pressures.

The similarities between the both variants of shaped pellets and the original powder confirms the previously observed suitability of this MOF towards the shaping process. The isotherms overlap almost fully, with a slight difference in maximum uptake in the order of powder > PVA > alumina.

4. Exploring the impact of material form on adsorption measurements

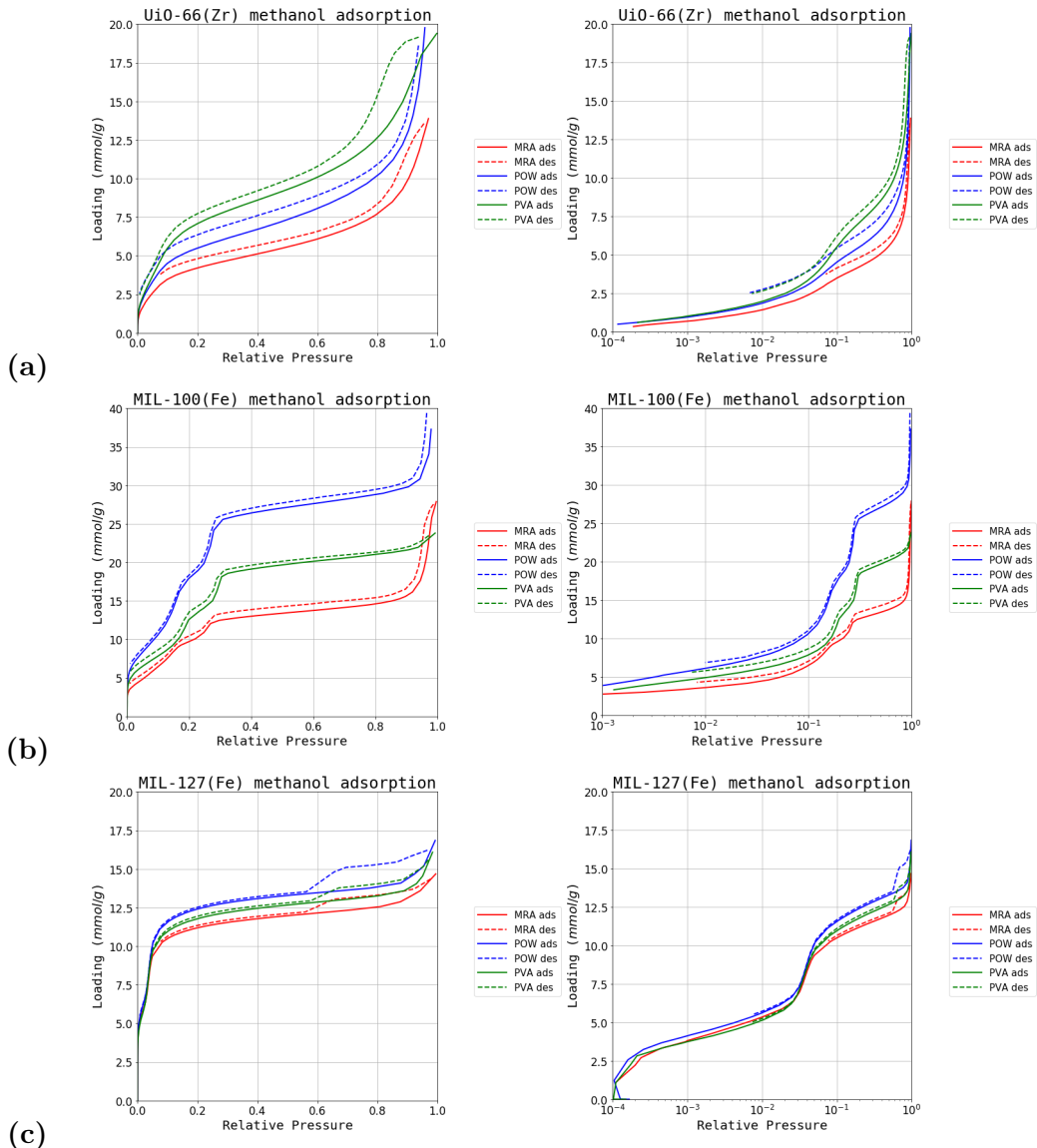


Figure 4.13.: Methanol adsorption isotherms (a) *UiO-66(Zr)*, (b) *MIL-100(Fe)* and (c) *MIL-127(Fe)*. The powder samples are in light blue, while the ρ -alumina (MRA) and poly-vinyl alcohol (PVA) samples are in red and dark blue respectively. Logarithmic graphs of the isotherms are on the right for clarity of the low pressure region.

4.5. Conclusion

It can be concluded that the process of alumina shaping does not, in general, have an impact on the surface chemistry of the three MOF materials. Interestingly, in regards to the changes in maximum capacity, each material has its own particular behaviour: UiO-66(Zr) has a higher loss in capacity with larger molecular probes, MIL-100(Fe) has a decrease of 10–20% across all gasses and MIL-127(Fe) matches loading on a mass basis except on CO and C₄H₁₀.

Water and methanol adsorption also further the hypothesis that the granulation process resulted in different effects on the MOF samples studied. The surface characteristics of neither pellet type appear changed from the powder variant, judging by the overlapping low pressure areas of all isotherms. When compared to the parent material, the alumina shaping method reduces the crystallinity of the samples studied, leading to lower uptakes. On the other hand, the polymer shaped version is less prone to amorphization, with the total adsorbed volume actually increasing in the case of UiO-66(Zr).

The shaping also induces a densification which, in almost all cases, leads to a better performance on a volumetric basis. However, the influence on the mass transport effects of the alumina binder is not known and should be investigated further.

Overall, the process of alumina shaping is a promising method of preparing MOFs for gas-related applications in separation and storage, but care should be taken to not generalise the effects present on one material to another.

Bibliography

- [1] Farid Akhtar, Linnéa Andersson, Steven Ogunwumi, Niklas Hedin, and Lennart Bergström. Structuring adsorbents and catalysts by processing of porous powders. *Journal of the European Ceramic Society*, 34(7):1643–1666, July 2014. ISSN 09552219. doi: 10.1016/j.jeurceramsoc.2014.01.008.
- [2] Douglas M. Ruthven, Shamsuzzaman Farooq, and Kent S. Knaebel. *Pressure Swing Adsorption*. VCH Publishers, New York, N.Y, 1994. ISBN 978-1-56081-517-4 978-3-527-89517-5.
- [3] Sharon Mitchell, Nina-Luisa Michels, Gerardo Majano, and Javier Pérez-Ramírez. Advanced visualization strategies bridge the multidimensional complexity of technical catalysts. *Current Opinion in Chemical Engineering*, 2(3):304–311, August 2013. ISSN 22113398. doi: 10.1016/j.coche.2013.04.005.
- [4] Douglas M. Ruthven. *Principles of Adsorption and Adsorption Processes*. Wiley, New York, 1984. ISBN 978-0-471-86606-0.
- [5] T. Ohji, M. Singh, J. A. Salem, Dongming Zhu, and American Ceramic Society, editors. *Advanced Processing and Manufacturing Technologies for Structural and Multifunctional Materials: A Collection of Papers Presented at the 31st International Conference on Advanced Ceramics and Composites, January 21-26, 2007, Daytona Beach, Florida*. Number v. 28, issue 7 in Ceramic engineering and science proceedings. Wiley-Interscience, Hoboken, N.J, 2008. ISBN 978-0-470-19638-0. OCLC: ocn154800301.
- [6] Teresa J. Bandosz, editor. *Activated Carbon Surfaces in Environmental Remediation*. Number 7 in Interface science and technology. Elsevier/AP, Amsterdam, 2006. ISBN 978-0-12-370536-5. OCLC: 255269962.
- [7] Gareth T. Whiting, Abhishek Dutta Chowdhury, Ramon Oord, Pasi Paalanen, and Bert M. Weckhuysen. The curious case of zeolite–clay/binder interactions and their consequences for catalyst preparation. *Faraday Discuss.*, 188:369–386, 2016. ISSN 1359-6640, 1364-5498. doi: 10.1039/C5FD00200A.
- [8] Nina-Luisa Michels, Sharon Mitchell, and Javier Pérez-Ramírez. Effects of Binders on the Performance of Shaped Hierarchical MFI Zeolites in Methanol-to-Hydrocarbons. *ACS Catalysis*, 4(8):2409–2417, August 2014. ISSN 2155-5435, 2155-5435. doi: 10.1021/cs500353b.
- [9] Stefan Kaskel, editor. *The Chemistry of Metal-Organic Frameworks: Synthesis, Characterization, and Applications*. Wiley-VCH Verlag GmbH & Co. KGaA, Weinheim, 2016. ISBN 978-3-527-33874-0 978-3-527-69305-4 978-3-527-69308-5 978-3-527-69306-1 978-3-527-69307-8.

BIBLIOGRAPHY

- [10] Enrique V. Ramos-Fernandez, Mariana Garcia-Domingos, Jana Juan-Alcañiz, Jorge Gascon, and Freek Kapteijn. MOFs meet monoliths: Hierarchical structuring metal organic framework catalysts. *Applied Catalysis A: General*, 391(1-2):261–267, January 2011. ISSN 0926860X. doi: 10.1016/j.apcata.2010.05.019.
- [11] Sonia Aguado, Jerome Canivet, and David Farrusseng. Facile shaping of an imidazolate-based MOF on ceramic beads for adsorption and catalytic applications. *Chemical Communications*, 46(42):7999, 2010. ISSN 1359-7345, 1364-548X. doi: 10.1039/c0cc02045a.
- [12] D. Bazer-Bachi, L. Assié, V. Lecocq, B. Harbuzaru, and V. Falk. Towards industrial use of metal-organic framework: Impact of shaping on the MOF properties. *Powder Technology*, 255:52–59, March 2014. ISSN 00325910. doi: 10.1016/j.powtec.2013.09.013.
- [13] Tian Tian, Jose Velazquez-Garcia, Thomas D. Bennett, and David Fairen-Jimenez. Mechanically and chemically robust ZIF-8 monoliths with high volumetric adsorption capacity. *Journal of Materials Chemistry A*, 3(6):2999–3005, 2015. ISSN 2050-7488, 2050-7496. doi: 10.1039/C4TA05116E.
- [14] Rocio Semino, Naseem A. Ramsahye, Aziz Ghoufi, and Guillaume Maurin. Microscopic Model of the Metal–Organic Framework/Polymer Interface: A First Step toward Understanding the Compatibility in Mixed Matrix Membranes. *ACS Applied Materials & Interfaces*, 8(1):809–819, January 2016. ISSN 1944-8244, 1944-8252. doi: 10.1021/acsami.5b10150.
- [15] Takashi Kitao, Yuanyuan Zhang, Susumu Kitagawa, Bo Wang, and Takashi Uemura. Hybridization of MOFs and polymers. *Chemical Society Reviews*, 46(11):3108–3133, 2017. ISSN 0306-0012. doi: 10.1039/C7CS00041C.
- [16] Nicolas Chanut, Andrew D. Wiersum, U-Hwang Lee, Young Kyu Hwang, Florence Ragon, Hubert Chevreau, Sandrine Bourrelly, Bogdan Kuchta, Jong-San Chang, Christian Serre, and Philip L. Llewellyn. Observing the Effects of Shaping on Gas Adsorption in Metal-Organic Frameworks. *European Journal of Inorganic Chemistry*, 2016(27):4416–4423, September 2016. ISSN 14341948. doi: 10.1002/ejic.201600410.
- [17] Jasmina Hafizovic Cavka, Søren Jakobsen, Unni Olsbye, Nathalie Guillou, Carlo Lamberti, Silvia Bordiga, and Karl Petter Lillerud. A New Zirconium Inorganic Building Brick Forming Metal Organic Frameworks with Exceptional Stability. *Journal of the American Chemical Society*, 130(42):13850–13851, October 2008. ISSN 0002-7863. doi: 10.1021/ja8057953.
- [18] Andrew D. Wiersum, Estelle Soubeyrand-Lenoir, Qingyuan Yang, Beatrice Moulin, Vincent Guillerm, Mouna Ben Yahia, Sandrine Bourrelly, Alexandre Vimont, Stuart Miller, Christelle Vagner, Marco Daturi, Guillaume Clet, Christian Serre, Guillaume

BIBLIOGRAPHY

- Maurin, and Philip L. Llewellyn. An Evaluation of UiO-66 for Gas-Based Applications. *Chemistry - An Asian Journal*, 6(12):3270–3280, December 2011. ISSN 18614728. doi: 10.1002/asia.201100201.
- [19] Patricia Horcajada, Suzy Surblé, Christian Serre, Do-Young Hong, You-Kyong Seo, Jong-San Chang, Jean-Marc Grenèche, Irene Margiolaki, and Gérard Férey. Synthesis and catalytic properties of MIL-100(Fe), an iron(III) carboxylate with large pores. *Chem. Commun.*, (27):2820–2822, 2007. ISSN 1359-7345, 1364-548X. doi: 10.1039/B704325B.
- [20] Qingyuan Yang, Sébastien Vaesen, Florence Ragon, Andrew D. Wiersum, Dong Wu, Ana Lago, Thomas Devic, Charlotte Martineau, Francis Taulelle, Philip L. Llewellyn, Hervé Jobic, Chongli Zhong, Christian Serre, Guy De Weireld, and Guillaume Maurin. A Water Stable Metal-Organic Framework with Optimal Features for CO₂ Capture. *Angewandte Chemie*, 125(39):10506–10510, September 2013. ISSN 00448249. doi: 10.1002/ange.201302682.
- [21] Ji Woong Yoon, You-Kyong Seo, Young Kyu Hwang, Jong-San Chang, Hervé Leclerc, Stefan Wuttke, Philippe Bazin, Alexandre Vimont, Marco Daturi, Emily Bloch, Philip L. Llewellyn, Christian Serre, Patricia Horcajada, Jean-Marc Grenèche, Alirio E. Rodrigues, and Gérard Férey. Controlled Reducibility of a Metal-Organic Framework with Coordinatively Unsaturated Sites for Preferential Gas Sorption. *Angewandte Chemie International Edition*, 49(34):5949–5952, August 2010. ISSN 14337851. doi: 10.1002/anie.201001230.
- [22] Yunling Liu, Jarrod F. Eubank, Amy J. Cairns, Juergen Eckert, Victor Ch. Kravtsov, Ryan Luebke, and Mohamed Eddaoudi. Assembly of Metal-Organic Frameworks (MOFs) Based on Indium-Trimer Building Blocks: A Porous MOF with soc Topology and High Hydrogen Storage. *Angewandte Chemie International Edition*, 46(18):3278–3283, April 2007. ISSN 14337851, 15213773. doi: 10.1002/anie.200604306.
- [23] Hubert Chevreau, Anastasia Permyakova, Farid Nouar, Paul Fabry, Carine Livage, Florence Ragon, Alfonso Garcia-Marquez, Thomas Devic, Nathalie Steunou, Christian Serre, and Patricia Horcajada. Synthesis of the biocompatible and highly stable MIL-127(Fe): From large scale synthesis to particle size control. *CrystEngComm*, 18(22):4094–4101, 2016. ISSN 1466-8033. doi: 10.1039/C5CE01864A.
- [24] Nicolas Chanut, Sandrine Bourrelly, Bogdan Kuchta, Christian Serre, Jong-San Chang, Paul A. Wright, and Philip L. Llewellyn. Screening the Effect of Water Vapour on Gas Adsorption Performance: Application to CO₂ Capture from Flue Gas in Metal-Organic Frameworks. *ChemSusChem*, 10(7):1543–1553, April 2017. ISSN 18645631. doi: 10.1002/cssc.201601816.
- [25] Anil H. Valekar, Kyung-Ho Cho, U-Hwang Lee, Ji Sun Lee, Ji Woong Yoon, Young Kyu Hwang, Seung Gwan Lee, Sung June Cho, and Jong-San Chang.

BIBLIOGRAPHY

- Shaping of porous metal–organic framework granules using mesoporous ρ -alumina as a binder. *RSC Advances*, 7(88):55767–55777, 2017. ISSN 2046-2069. doi: 10.1039/C7RA11764G.
- [26] Pritha Ghosh, Yamil J. Colón, and Randall Q. Snurr. Water adsorption in UiO-66: The importance of defects. *Chem. Commun.*, 50(77):11329–11331, 2014. ISSN 1359-7345, 1364-548X. doi: 10.1039/C4CC04945D.

5. Exploring novel behaviours

5.1. Introduction

5.2. Literature

5.3. Method

5.4. Results and discussion

5.5. Conclusion

BIBLIOGRAPHY

Bibliography

A. Common characterisation techniques

pictures?

A.1. Thermogravimetry

Thermogravimetry (TGA) is a standard laboratory technique where the weight of a sample is monitored while ambient temperature is controlled. Changes in sample mass can be correlated to physical events, such as adsorption, desorption, sample decomposition or oxidation, depending on temperature and its rate of change.

TGA experiments are carried out on approximately 15 mg of sample with a TA Instruments Q500 up to 800 °C. The sample is placed on a platinum crucible and sealed in a temperature controlled oven, under gas flow of $40 \text{ cm}^3 \text{ min}^{-1}$. Experiments can use a blanket of either air or argon. The temperature ramp can be specified directly and should be chosen to ensure that the sample is in equilibrium with the oven temperature and no thermal conductivity effects come into play. Alternatively, a dynamic “Hi-Res” mode can be used which allows for automatic cessation of heating rate while the sample undergoes mass loss.

The main purpose of thermogravimetry as used in this thesis is the determination of sample decomposition temperature, to ensure that thermal activation prior to adsorption is complete and that all guest molecules have been removed without loss of structure. To this end, experiments are performed under an inert atmosphere (argon), and the sample activation temperature is chosen as 50 °C to 100 °C lower than the sample decomposition temperature.

A.2. Bulk density determination

Bulk density is a useful metric for the industrial use of adsorbent materials, as their volume plays a critical role in equipment sizing.

Bulk density is determined by weighing 1.5 ml empty glass vessels and settling the MOFs inside. Powder materials are then added in small increments and settled through vibration between each addition. The full vessel is finally weighed, which allowed the bulk density to be determined. The same cell is used in all experiments, with cleaning through sonication between each experiment.

A. Common characterisation techniques

A.3. Skeletal density determination

True density or skeletal density is determined through gas pycnometry in a Microtrac-BEL BELSORP-max apparatus. Helium is chosen as the fluid of choice as it is assumed to be non-adsorbing.

The volume of a glass sample cell (V_c) is precisely measured through dosing of the reference volume with helium up to (p_1), then opening the valve connecting the two and allowing the gas to expand up to (p_2). Afterwards approximately 50 mg of sample are weighed and inserted in a glass sample cell. After sample activation using the supplied electric heater to ensure no solvent residue is left in the pores, the same procedure is repeated to determine the volume of the cell and the adsorbent. With the volume of the sample determined, the density can be calculated by.

$$V_s = V_c + \frac{V_r}{1 - \frac{p_1}{p_2}} \quad (\text{A.1})$$

A.4. Nitrogen physisorption at 77 K

Nitrogen adsorption experiments are carried out on a Micromeritics Triflex apparatus. Approximately 60 mg of sample are used for each measurement. Empty glass cells are weighed and filled with the samples, which are then activated in a Micromeritics Smart VacPrep up to their respective activation temperature under vacuum and then back-filled with an inert atmosphere. After sample activation, the cells are re-weighed to determine the precise sample mass. The cells are covered with a porous mantle which allows for a constant temperature gradient during measurement by wicking liquid nitrogen around the cell. Finally, the cells are immersed in a liquid nitrogen bath and the adsorption isotherm is recorded using the volumetric method. A separate cell is used to condense the adsorptive throughout the measurement for accurate determination of its saturation pressure.

A.5. Vapour physisorption at 298 K

Vapour adsorption isotherms throughout this work are measured using a MicrotracBEL BELSORP-max apparatus in vapour mode. Glass cells are first weighed and then filled with about 50 mg of sample. The vials are then heated under vacuum up to the activation temperature of the material and re-weighed in order to measure the exact sample mass without adsorbed guests. The cells are then immersed in a mineral oil bath kept at 298 K. To ensure that the cold point of the system occurs in the material and to prevent condensation on cell walls, the reference volume, dead space and vapour source are temperature controlled through an insulated enclosure.

BIBLIOGRAPHY

A.6. Gravimetric isotherms

The gravimetric isotherms in this thesis are obtained using a commercial Rubotherm GmbH balance. Approximately 1 g of dried sample is used for these experiments. Samples are activated *in situ* by heating under vacuum. The gas is introduced using a step-by-step method, and equilibrium is assumed to have been reached when the variation of weight remained below 30 µg over a 15 min interval. The volume of the sample is determined from a blank experiment with helium as the non-adsorbing gas and used in combination with the gas density measured by the Rubotherm balance to compensate for buoyancy.

A.7. High throughput isotherm measurement

A high-throughput gas adsorption apparatus is presented for the evaluation of adsorbents of interest in gas storage and separation applications. This instrument is capable of measuring complete adsorption isotherms up to 50 bar on six samples in parallel using as little as 60 mg of material. Multiple adsorption cycles can be carried out and four gases can be used sequentially, giving as many as 24 adsorption isotherms in 24 h.⁽¹⁾

A.8. Powder X-ray diffraction

A.9. Nuclear magnetic resonance

Bibliography

- [1] Andrew D. Wiersum, Christophe Giovannangeli, Dominique Vincent, Emily Bloch, Helge Reinsch, Norbert Stock, Ji Sun Lee, Jong-San Chang, and Philip L. Llewellyn. Experimental Screening of Porous Materials for High Pressure Gas Adsorption and Evaluation in Gas Separations: Application to MOFs (MIL-100 and CAU-10). *ACS Combinatorial Science*, 15(2):111–119, February 2013. ISSN 2156-8952. doi: 10.1021/co300128w.

B. Synthesis method of referenced materials

B.1. Takeda 5A reference carbon

The Takeda 5A carbon was purchased directly from the Takeda corporation. The sample was activated at 250 °C under secondary vacuum (5 mbar) before any measurements.

full characterization

B.2. MCM-41 controlled pore glass

MCM-41 (Mobil Composition of Matter No. 41) is a mesoporous silica (SiO_2) material with a narrow pore distribution. First synthesised by the Mobil Oil Corporation, it is produced through templated synthesis using mycelle-forming surfactants. The material referenced in this thesis was purchased from Sigma-Aldrich. The activation procedure consists of heating at 250 °C under secondary vacuum (5 mbar).

B.3. Zr fumarate MOF

The synthesis of the Zr fumarate was performed in Peter Behren's group in Hannover, through modulated synthesis. This MOF can only be synthesised through the addition of a modulator, in this case fumaric acid, to the ongoing reactor, as detailed in the original publication.⁽¹⁾

The procedure goes as follows: ZrCl_4 (0.517 mmol, 1 eq) and fumaric acid (1.550 mmol, 3 eq) are dissolved in 20 mL N,N-dimethylformamide (DMF) and placed in a 100 mL glass flask at room temperature. 20 equivalents of formic acid were added. The glass flasks were Teflon-capped and heated in an oven at 120 °C for 24 h. After cooling, the white precipitate was washed with 10 mL DMF and 10 mL ethanol, respectively. The washing process was carried out by centrifugation and redispersion of the white powder, which was then dried at room temperature over night

B.4. UiO-66(Zr) for defect study

The UiO-66(Zr) sample preparation was adapted from Shearer et al. ⁽²⁾ as follows: ZrCl_4 (1.55 g, 6.65 mmol), an excess of terephthalic acid (BDC) (1.68 g, 10.11 mmol), HCl 37 % solution (0.2 mL, 3.25 mmol) and N,N'-dimethylformamide (DMF) (200 mL,

B. Synthesis method of referenced materials

2.58 mol) were added to a 250 mL pressure resistant Schott bottle. The mixture was stirred for 10 min, followed by incubation in a convection oven at 130 °C for 24 h. The resulting white precipitate was washed with fresh DMF (3× 50 mL) followed by ethanol (3× 50 mL) over the course of 48 h and dried at 60 °C. After drying, the sample was activated on a vacuum oven by heating at 200 °C under vacuum for 12 h. The yield was 78 % white microcrystalline powder. Before the experiment, the sample was calcined at 200 °C under vacuum (5 mbar) to remove any residual solvents from the framework.

B.5. UiO-66(Zr) for shaping study

The scaled-up synthesis of UiO-66(Zr) was carried out in a 5 L glass reactor (Reactor Master, Syrris, equipped with a reflux condenser and a Teflon-lined mechanical stirrer) according to a previously reported method.⁽³⁾ In short, 462 g (2.8 mol) of H₂BDC (98%) was initially dissolved in 2.5 L of dimethyl formamide (DMF, 2.36 kg, 32.3 mol) at room temperature. Then, 896 g (2.8 mol) of ZrOCl₂ · 8H₂O (98%) and 465 mL of 37% HCl (548 g, 15 mol) were added to the mixture. The molar ratio of the final ZrOCl₂ · 8H₂O/H₂BDC/DMF/HCl mixture was 1 : 1 : 11.6 : 5.4. The reaction mixture was vigorously stirred to obtain a homogeneous gel. The mixture was then heated to 423 K at a rate of 1 K min⁻¹ and maintained at this temperature for 6 h in the reactor without stirring, leading to a crystalline UiO-66(Zr) solid. The resulting product (510 g) was recovered from the slurry by filtration, redispersed in 7 L of DMF at 333 K for 6 h under stirring, and recovered by filtration. The same procedure was repeated twice, using methanol (MeOH) instead of DMF. The solid product was finally dried at 373 K overnight.

B.6. MIL-100(Fe) for shaping study

The synthesis of the MOF for the shaping study was done at the KRICT institute using a previously published method.⁽⁴⁾ To synthesise the MIL-100(Fe) material Fe(NO₃)₃ was completely dissolved in water. Then, trimesic acid (BTC) was added to the solution; the resulting mixture was stirred at room temperature for 1h. The final composition was Fe(NO₃)₃ · 9 H₂O:0.67 BTC:*n* H₂O (*x*= 55–280). The reactant mixture was heated at 433 K for 12 h using a Teflon-lined pressure vessel. The synthesized solid was filtered and washed with deionized (DI) water. Further washing was carried out with DI water and ethanol at 343 K for 3 h and purified with a 38 mM NH₄F solution at 343 K for 3 h. The solid was finally dried overnight at less than 373 K in air.

B.7. MIL-127(Fe) for shaping study

MIL-127(Fe) was synthesized by reaction of Fe(ClO₄)₃ · 6 H₂O (3.27 g, 9.2 mmol) and C₁₆N₂O₈H₆ (3.3 g) in DMF (415 mL) and hydrofluoric acid (5 M, 2.7 mL) at 423 K in a Teflon flask. The obtained orange crystals were placed in DMF (100 mL) and

BIBLIOGRAPHY

stirred at ambient temperature for 5 h. The final product was kept at 375 K overnight. MIL-127(Fe) was synthesized by reaction of $\text{Fe}(\text{ClO}_4)_3 \cdot 6 \text{H}_2\text{O}$ (3.27 g, 9.2 mmol) and $\text{C}_{16}\text{N}_2\text{O}_8\text{H}_6$ (3.3 g) in DMF (415 mL) and hydrofluoric acid (5 M, 2.7 mL) at 423 K in a Teflon flask. The obtained orange crystals were placed in DMF (100 mL) and stirred at ambient temperature for 5 h. The final product was kept at 375 K overnight.

Bibliography

- [1] Gesa Wißmann, Andreas Schaate, Sebastian Lilienthal, Imke Bremer, Andreas M. Schneider, and Peter Behrens. Modulated synthesis of Zr-fumarate MOF. *Micro-porous and Mesoporous Materials*, 152:64–70, April 2012. ISSN 13871811. doi: 10.1016/j.micromeso.2011.12.010.
- [2] Greig C. Shearer, Sachin Chavan, Jayashree Ethiraj, Jenny G. Vitillo, Stian Svelle, Unni Olsbye, Carlo Lamberti, Silvia Bordiga, and Karl Petter Lillerud. Tuned to Perfection: Ironing Out the Defects in Metal–Organic Framework UiO-66. *Chemistry of Materials*, 26(14):4068–4071, July 2014. ISSN 0897-4756, 1520-5002. doi: 10.1021/cm501859p.
- [3] Florence Ragon, Patricia Horcajada, Hubert Chevreau, Young Kyu Hwang, U-Hwang Lee, Stuart R. Miller, Thomas Devic, Jong-San Chang, and Christian Serre. In Situ Energy-Dispersive X-ray Diffraction for the Synthesis Optimization and Scale-up of the Porous Zirconium Terephthalate UiO-66. *Inorganic Chemistry*, 53(5):2491–2500, March 2014. ISSN 0020-1669, 1520-510X. doi: 10.1021/ic402514n.
- [4] Felix Jeremias, Stefan K. Henninger, and Christoph Janiak. Ambient pressure synthesis of MIL-100(Fe) MOF from homogeneous solution using a redox pathway. *Dalton Transactions*, 45(20):8637–8644, 2016. ISSN 1477-9226, 1477-9234. doi: 10.1039/C6DT01179A.

C. Appendix for chapter 4

C.1. Calorimetry dataset UiO-66(Zr)

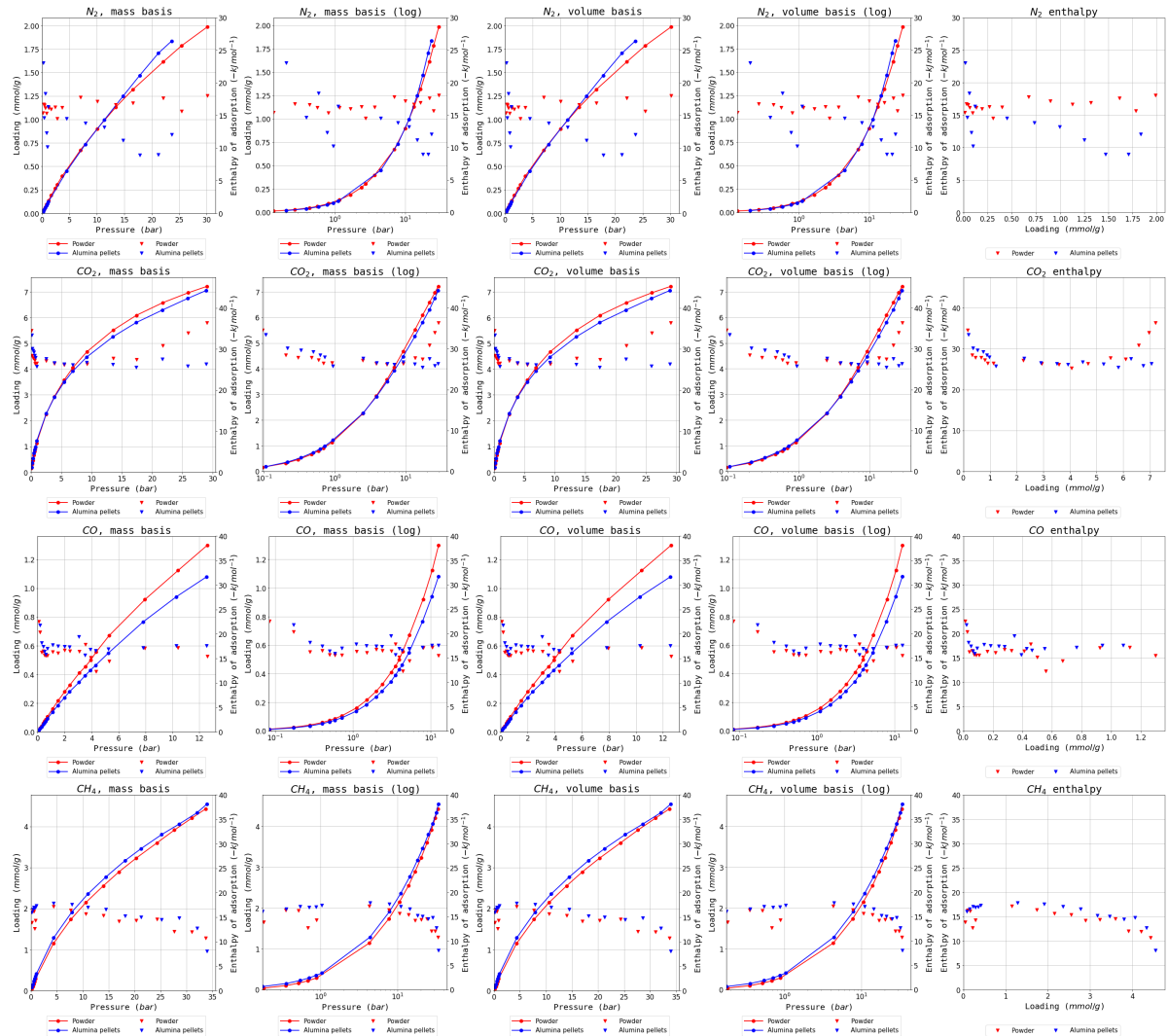


Figure C.1.: Complete isotherm and enthalpy dataset for UiO-66(Zr)

C. Appendix for chapter 4

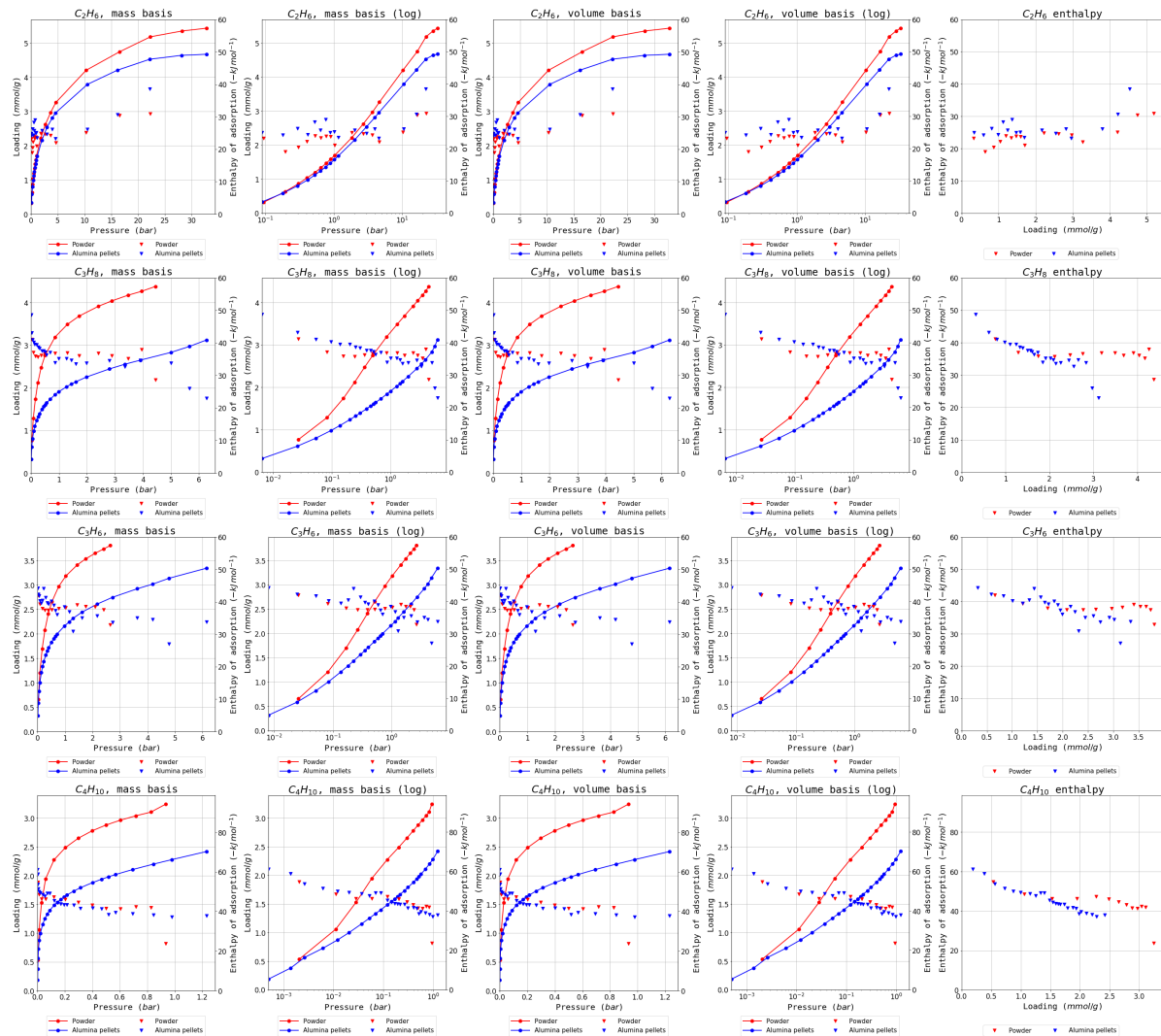


Figure C.1.: Complete isotherm and enthalpy dataset for $\text{UiO-66}(\text{Zr})$

C.2. Calorimetry MIL-100(Fe)

C. Appendix for chapter 4

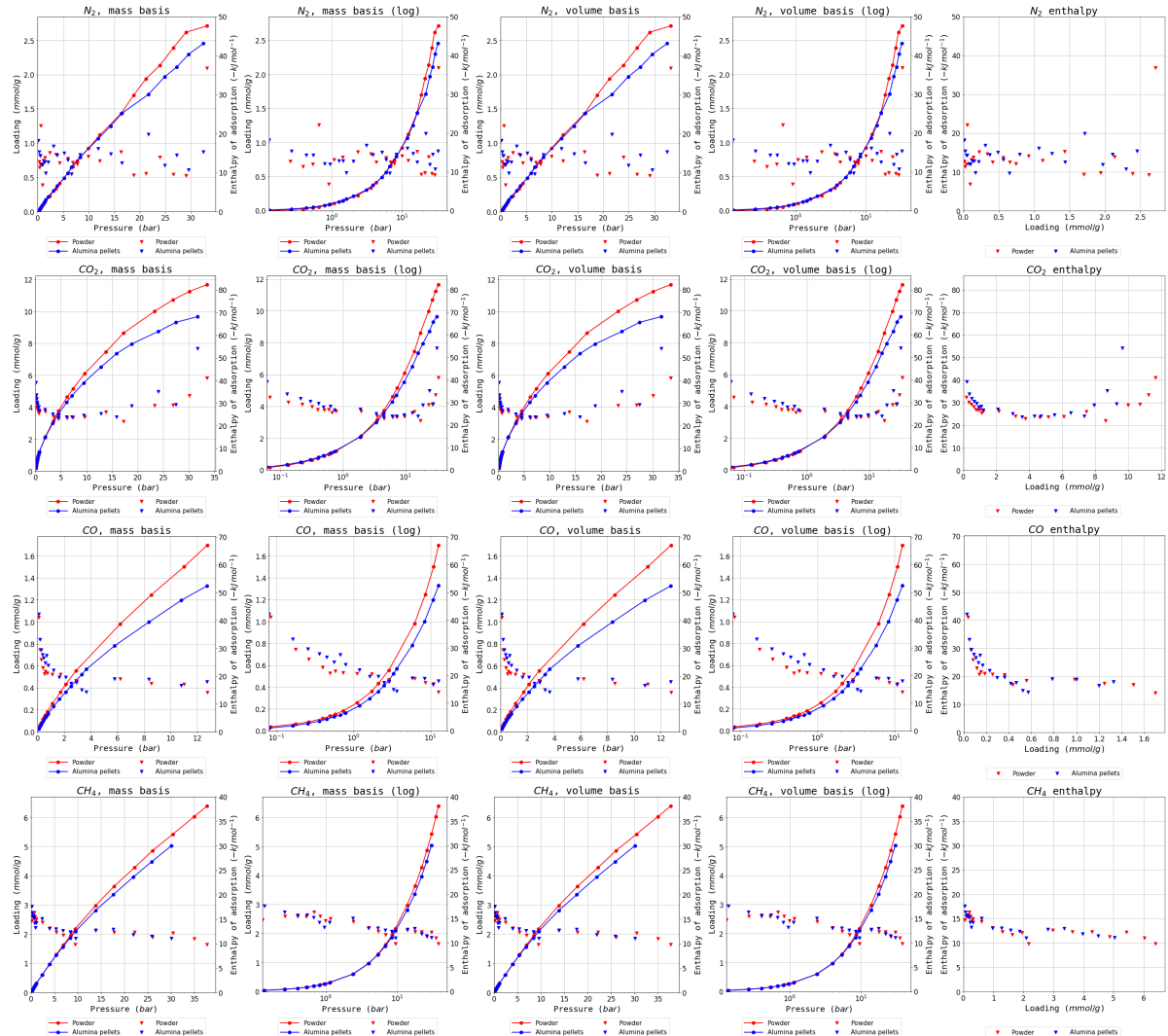


Figure C.2.: Complete isotherm and enthalpy dataset for MIL-100(Fe)

C. Appendix for chapter 4

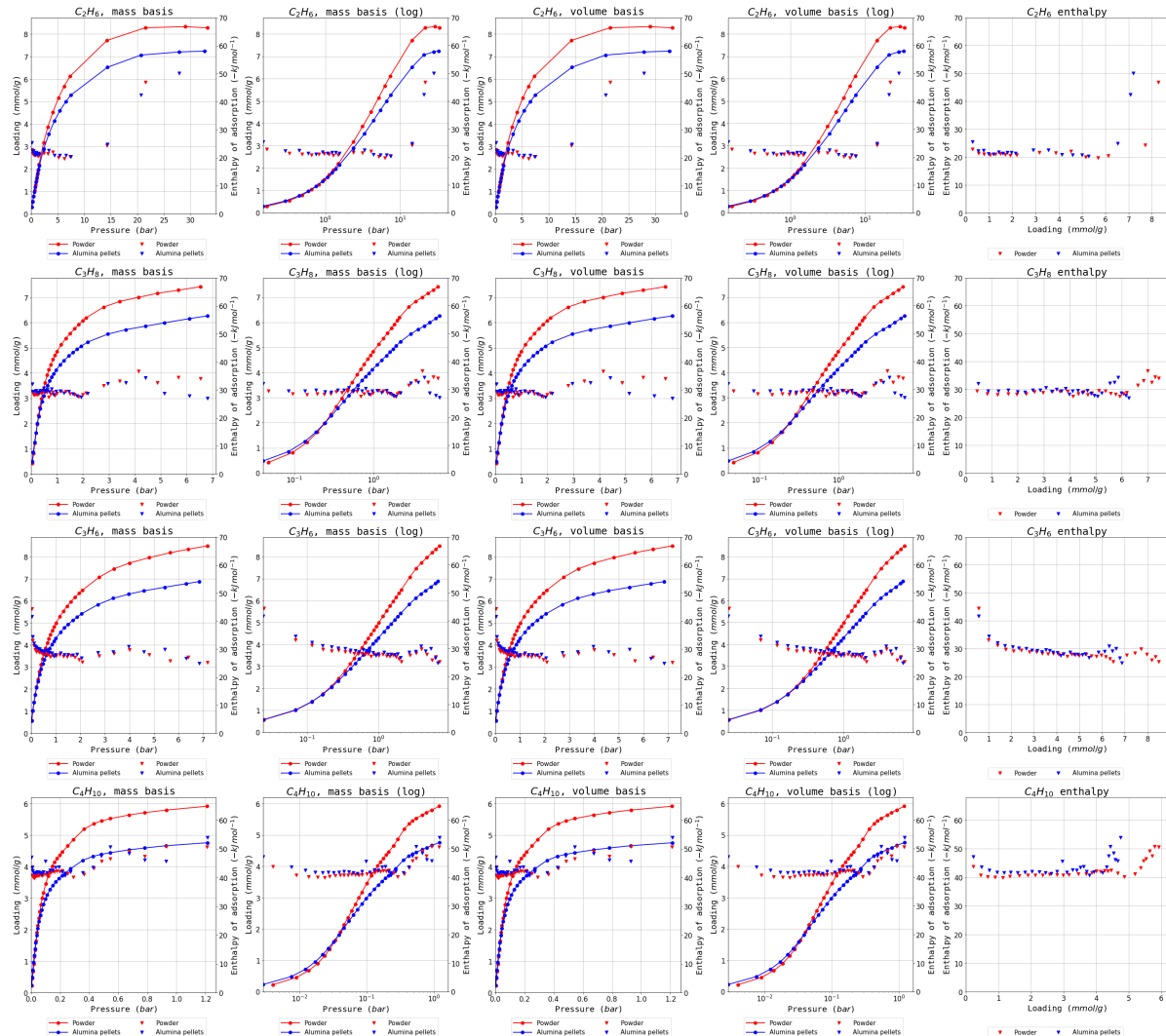


Figure C.2.: Complete isotherm and enthalpy dataset for MIL-100(Fe)

BIBLIOGRAPHY

C.3. Calorimetry MIL-127(Fe)

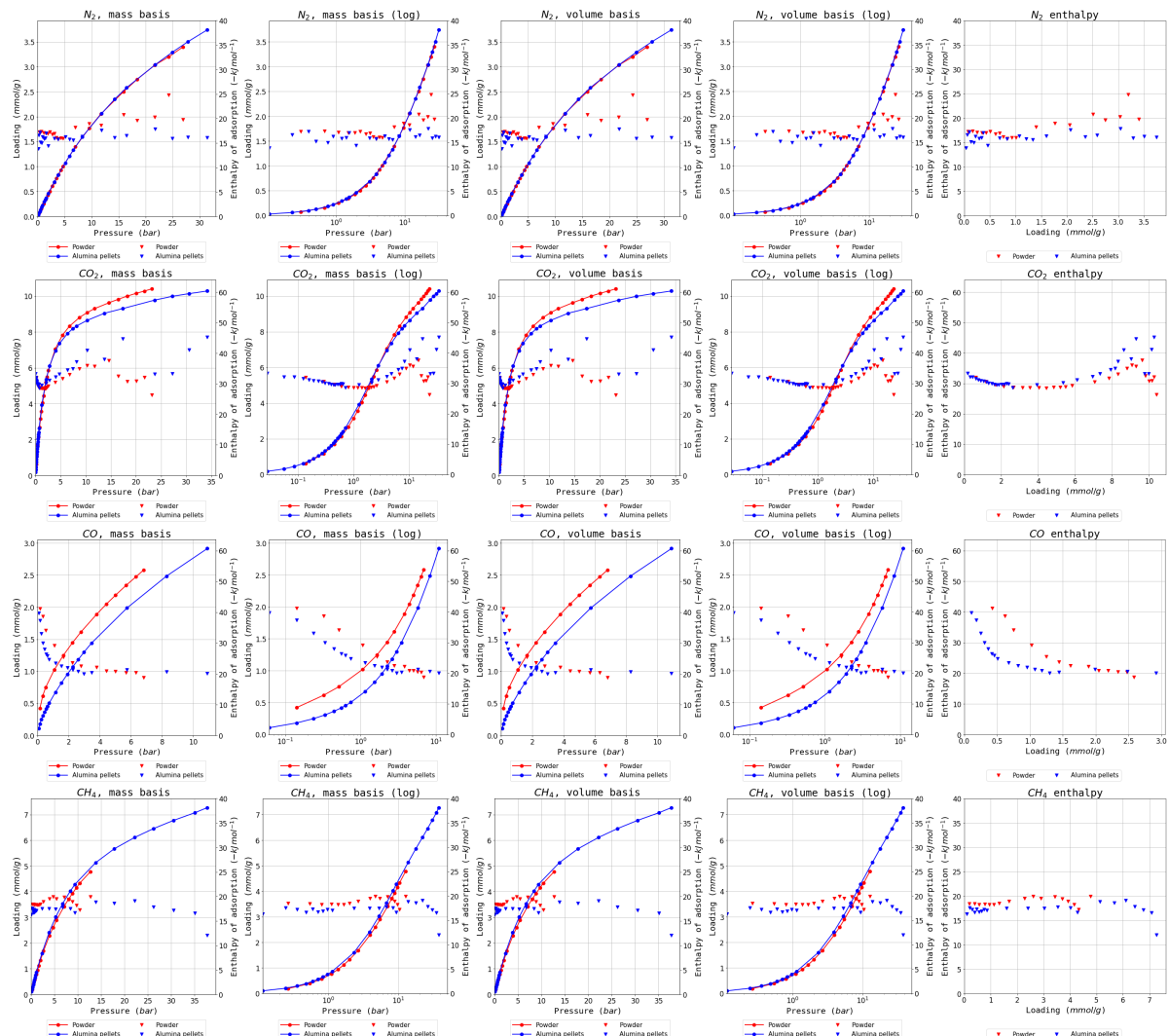


Figure C.3.: Complete isotherm and enthalpy dataset for MIL-127(Fe)

Bibliography

BIBLIOGRAPHY

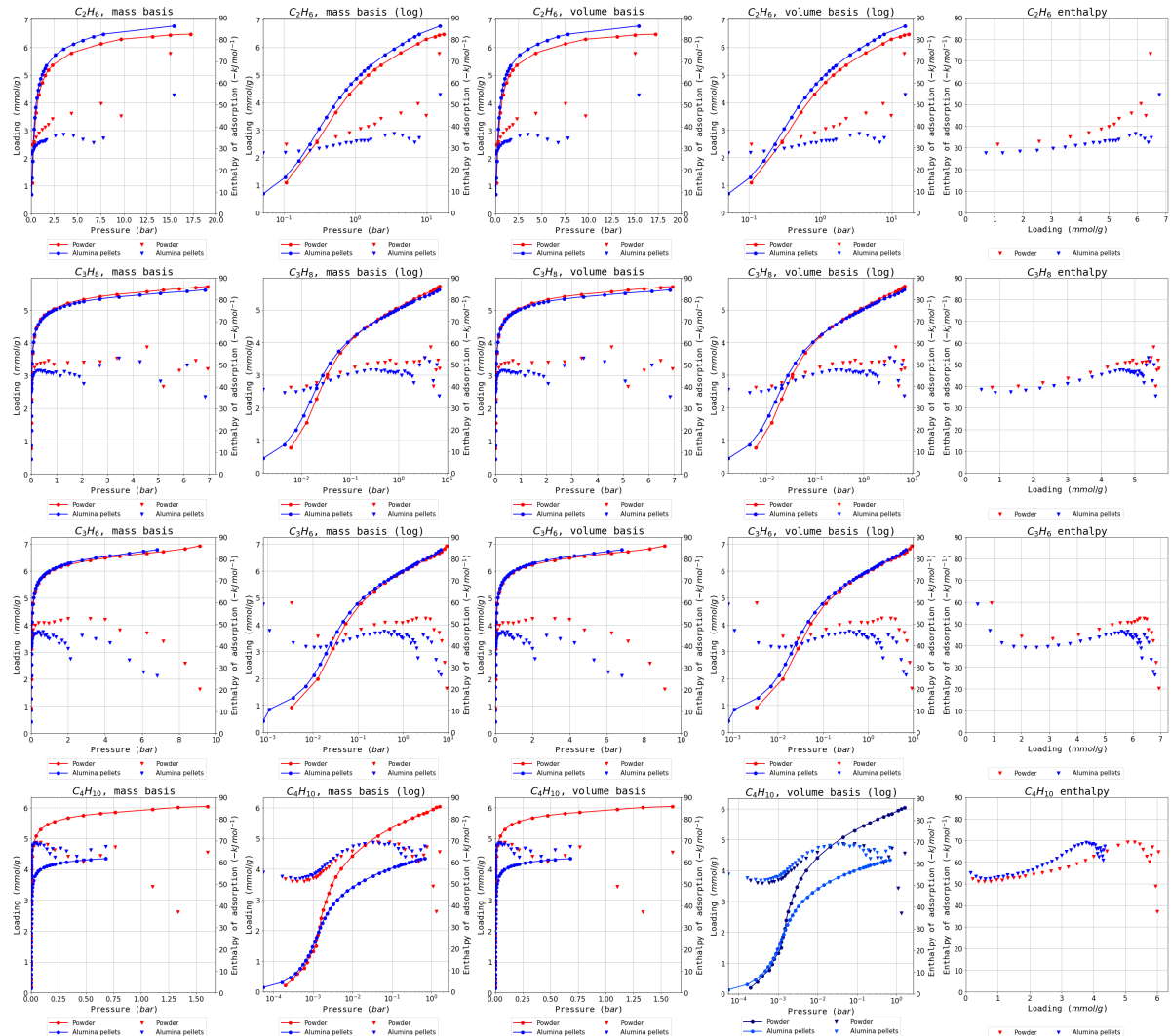


Figure C.3.: Complete isotherm and enthalpy dataset for MIL-127(Fe)

D. Appendix for chapter 3

D.1. Acid and solvent properties

Table D.1.: Solvent properties

Solvent	Polarity relative to water	Boiling point °C	Viscosity cP, at 20 °C	Acidity pKa
DMF	0.386	65	0.92	base of formic acid
DMSO	0.444	100	1.99	35
EtOH	0.762	153	0.54	15.5
H ₂ O	1.000	189	0.89	14

Table D.2.: Leaching acid properties

Acid	Acidity pKa	Solubility (g/100g) at 25 °C			
		H ₂ O	MeOH	DMF	DMSO
formic	3.75	miscible	miscible	miscible	miscible
acetic	4.45	miscible	miscible	miscible	miscible
trifluoroacetic	0.3	miscible	miscible	miscible	miscible
benzoic	4.19	0.24 ⁽¹⁾	77 ⁽¹⁾	149 ⁽¹⁾	162 ⁽¹⁾

D.2. Powder diffraction patterns

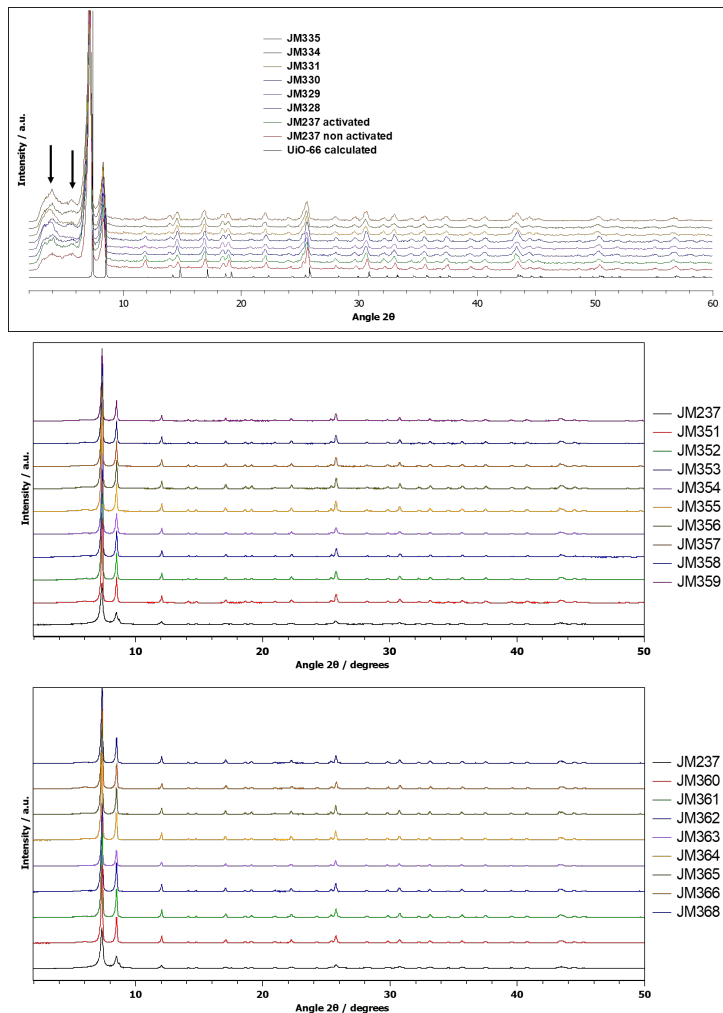


Figure D.1.: PXRD patterns for all samples

D.3. TGA curves

D.3.1. DMF leached samples

D. Appendix for chapter 3

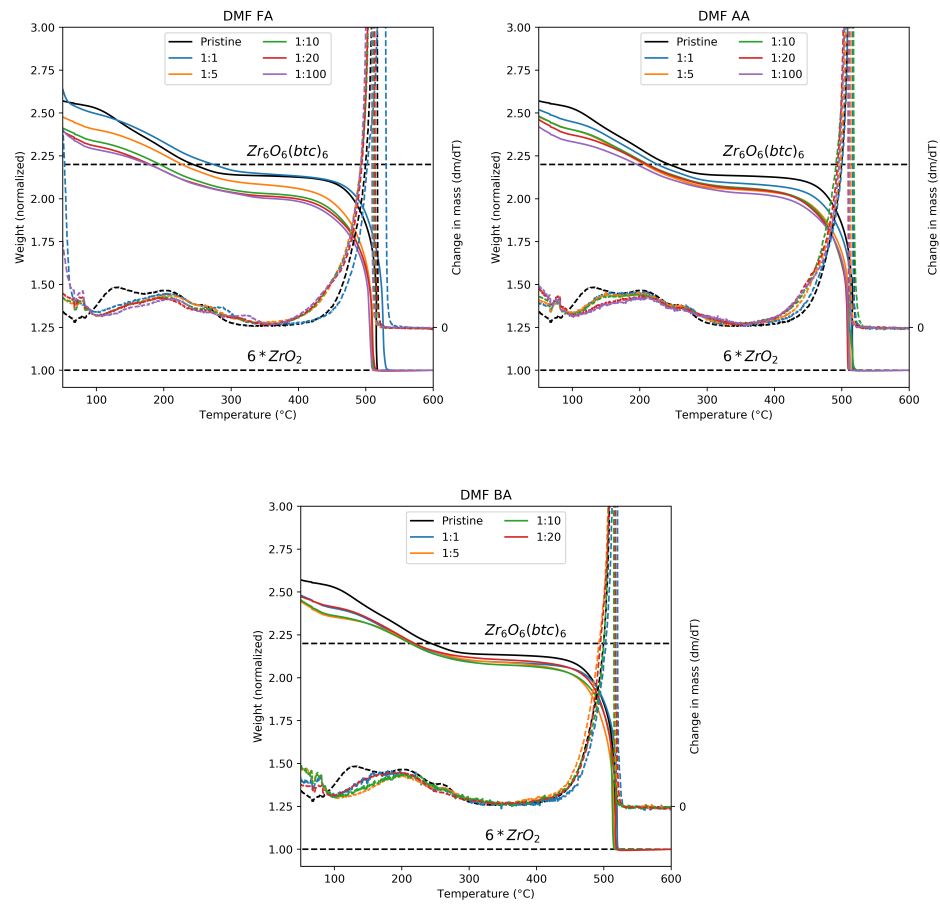


Figure D.2.: TGA curves for samples leached in DMF

D.3.2. Water leached samples

D. Appendix for chapter 3

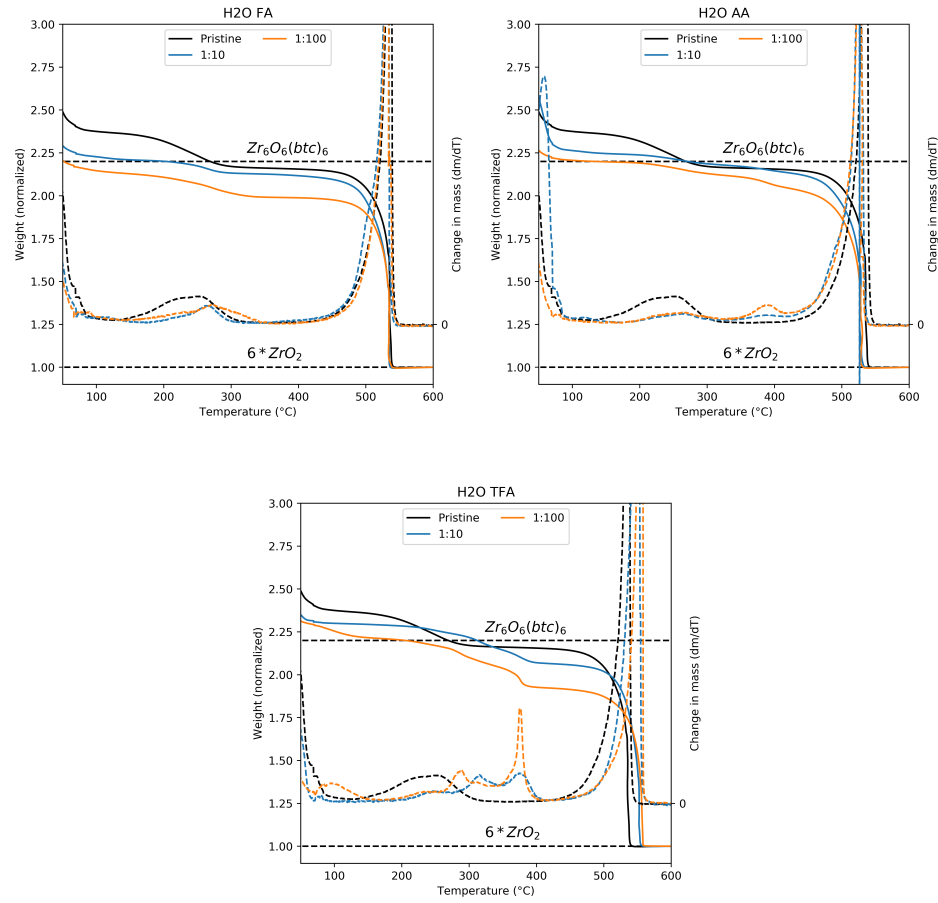


Figure D.3.: TGA curves for samples leached in H₂O

D.3.3. Methanol leached samples

D. Appendix for chapter 3

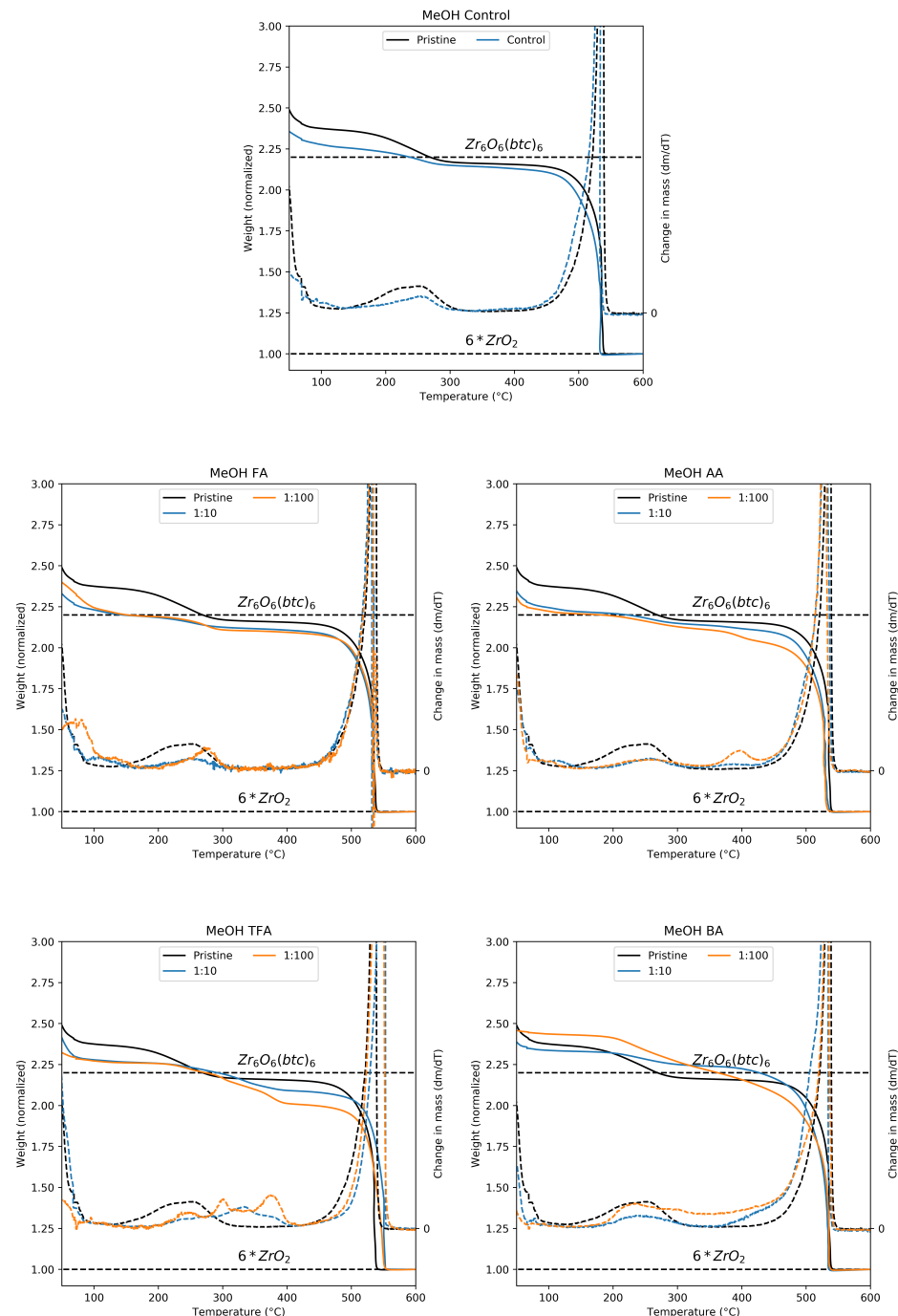


Figure D.4.: TGA curves for samples leached in MeOH

D.3.4. DMSO leached samples

D. Appendix for chapter 3

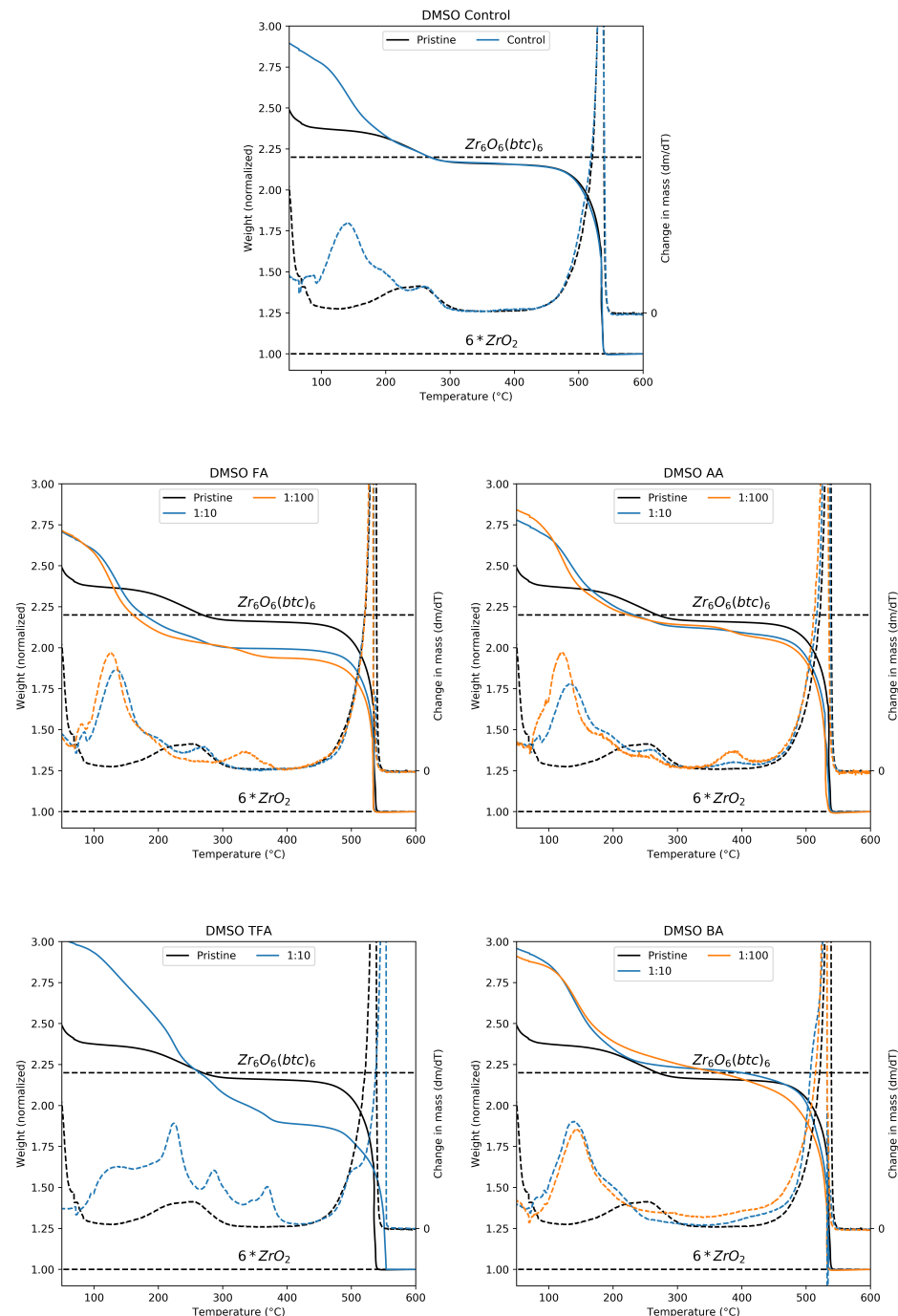


Figure D.5.: TGA curves for samples leached in DMSO

D.3.5. High resolution curves

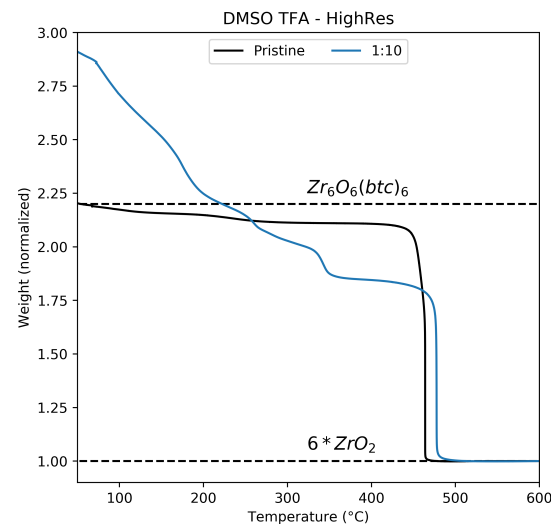


Figure D.6.: High resolution TGA curves for a DMSO/TFA leached sample

D.4. Nitrogen sorption isotherms

D.4.1. DMF leached samples

D. Appendix for chapter 3

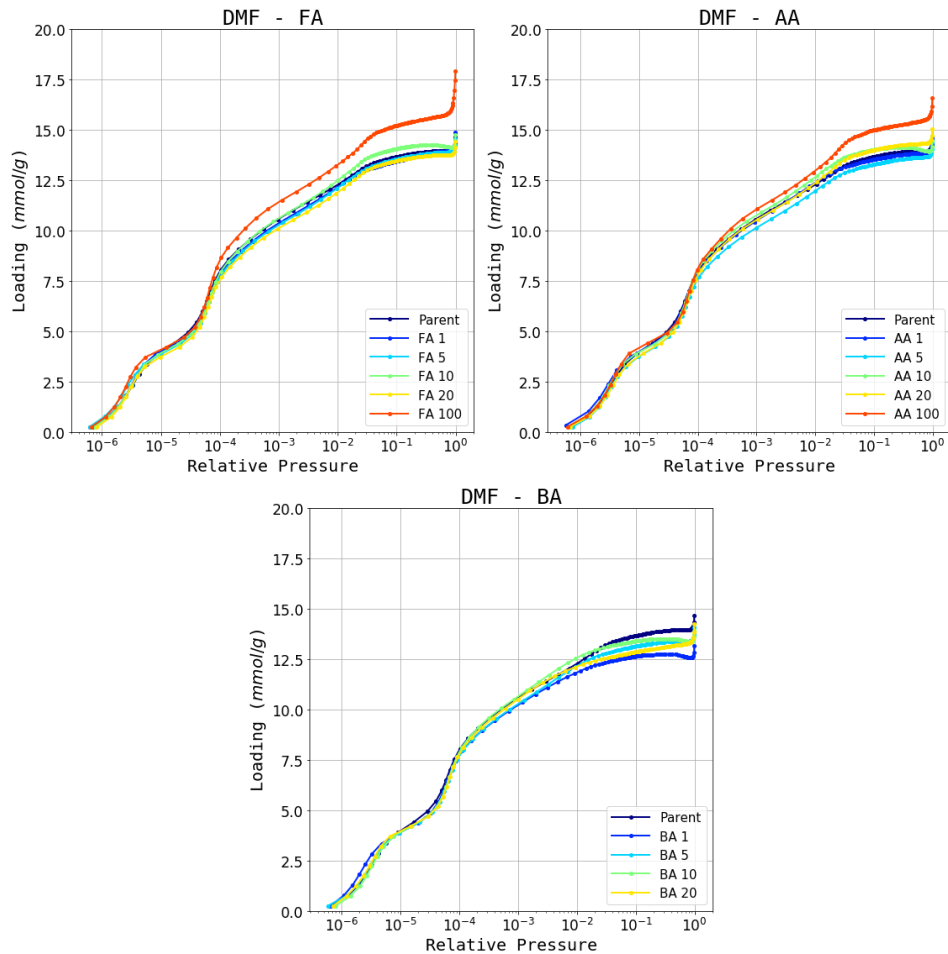


Figure D.7.: DMF isotherm dataset activated at 200 °C

D.4.2. H₂O leached samples

D. Appendix for chapter 3

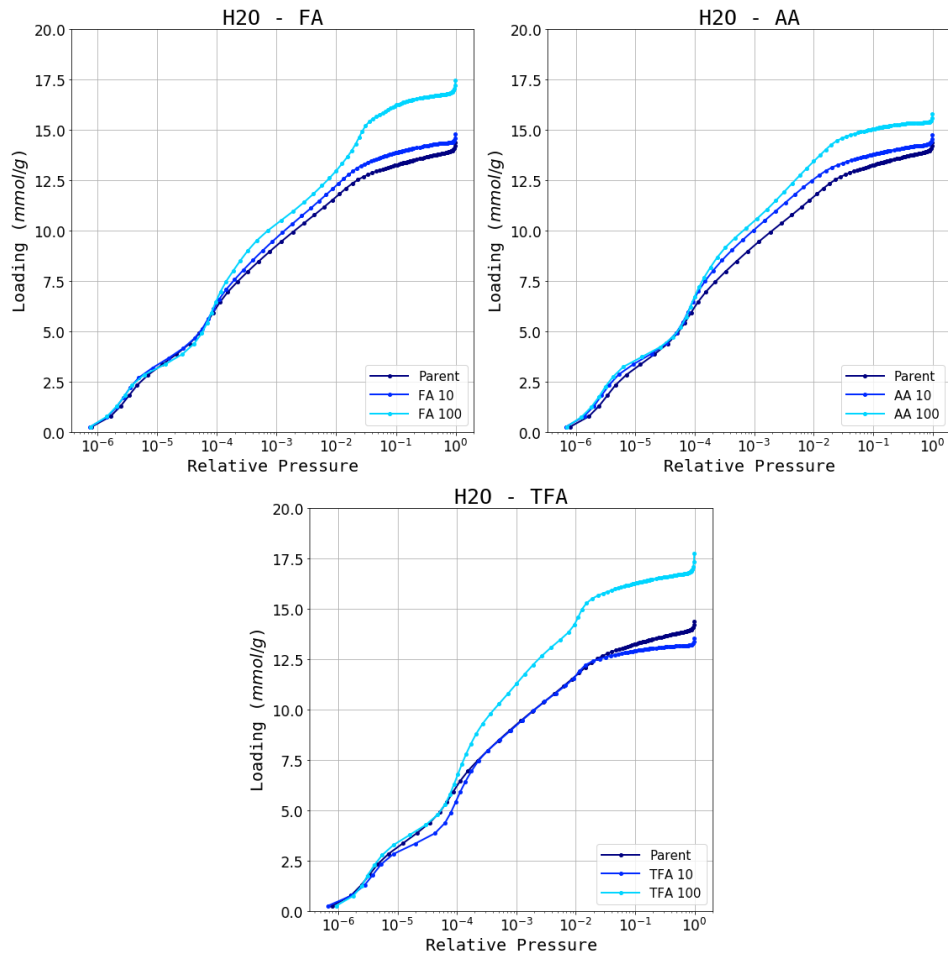


Figure D.7.: H₂O isotherm dataset activated at 200 °C

D.4.3. MeOH leached samples

D. Appendix for chapter 3

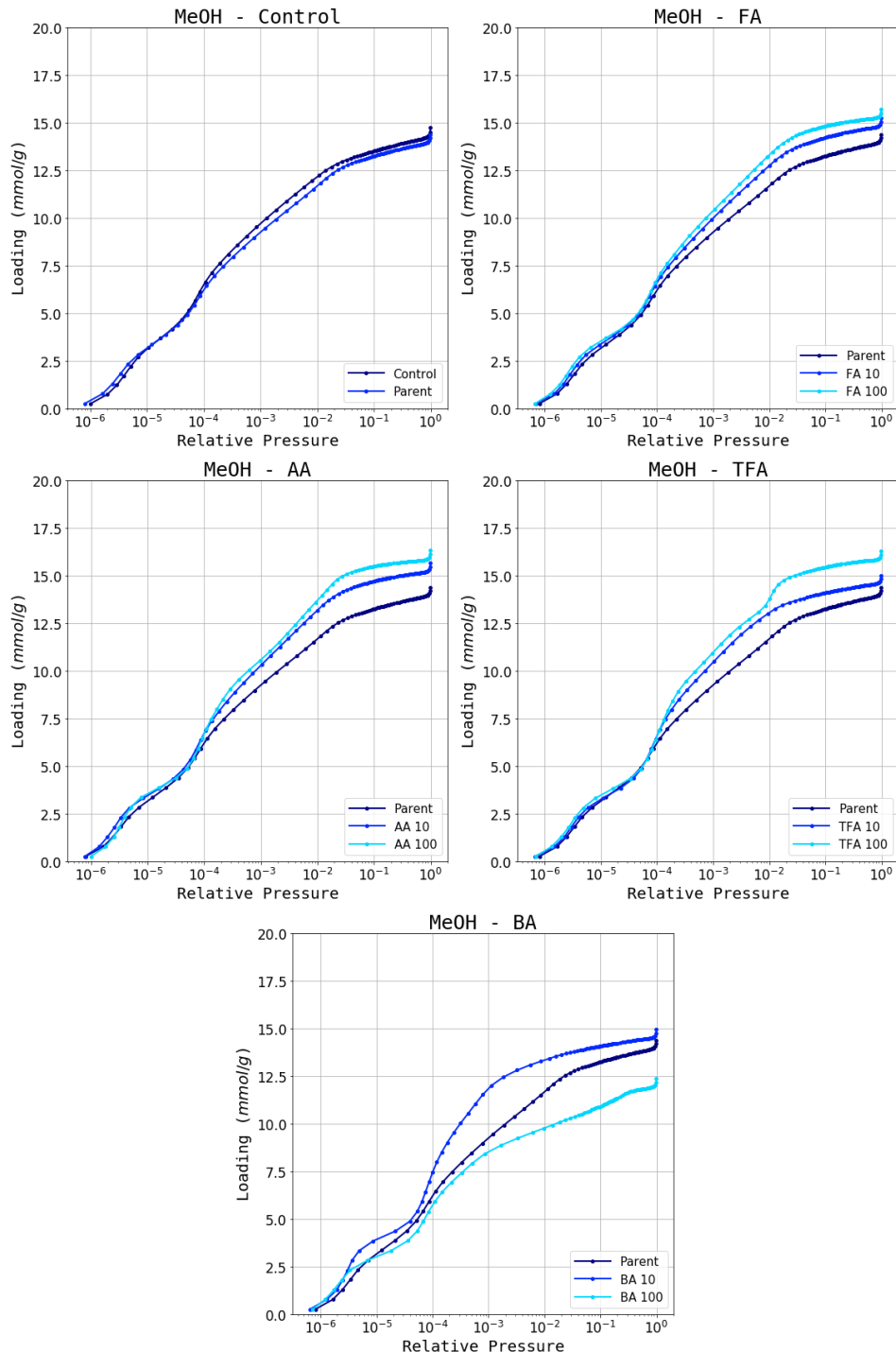


Figure D.8.: MeOH isotherm dataset activated at 200 °C

D.4.4. DMSO leached samples

D. Appendix for chapter 3

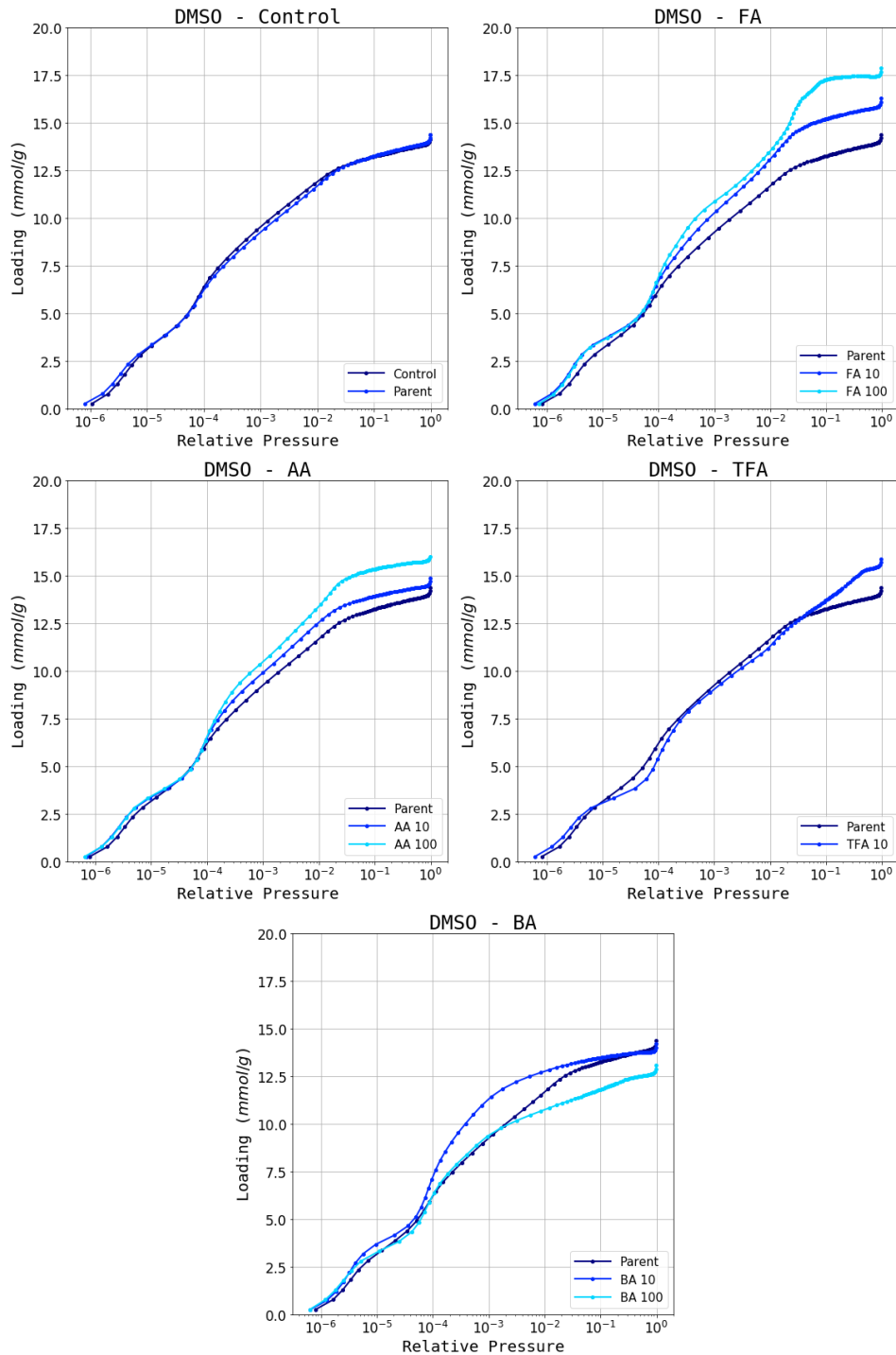
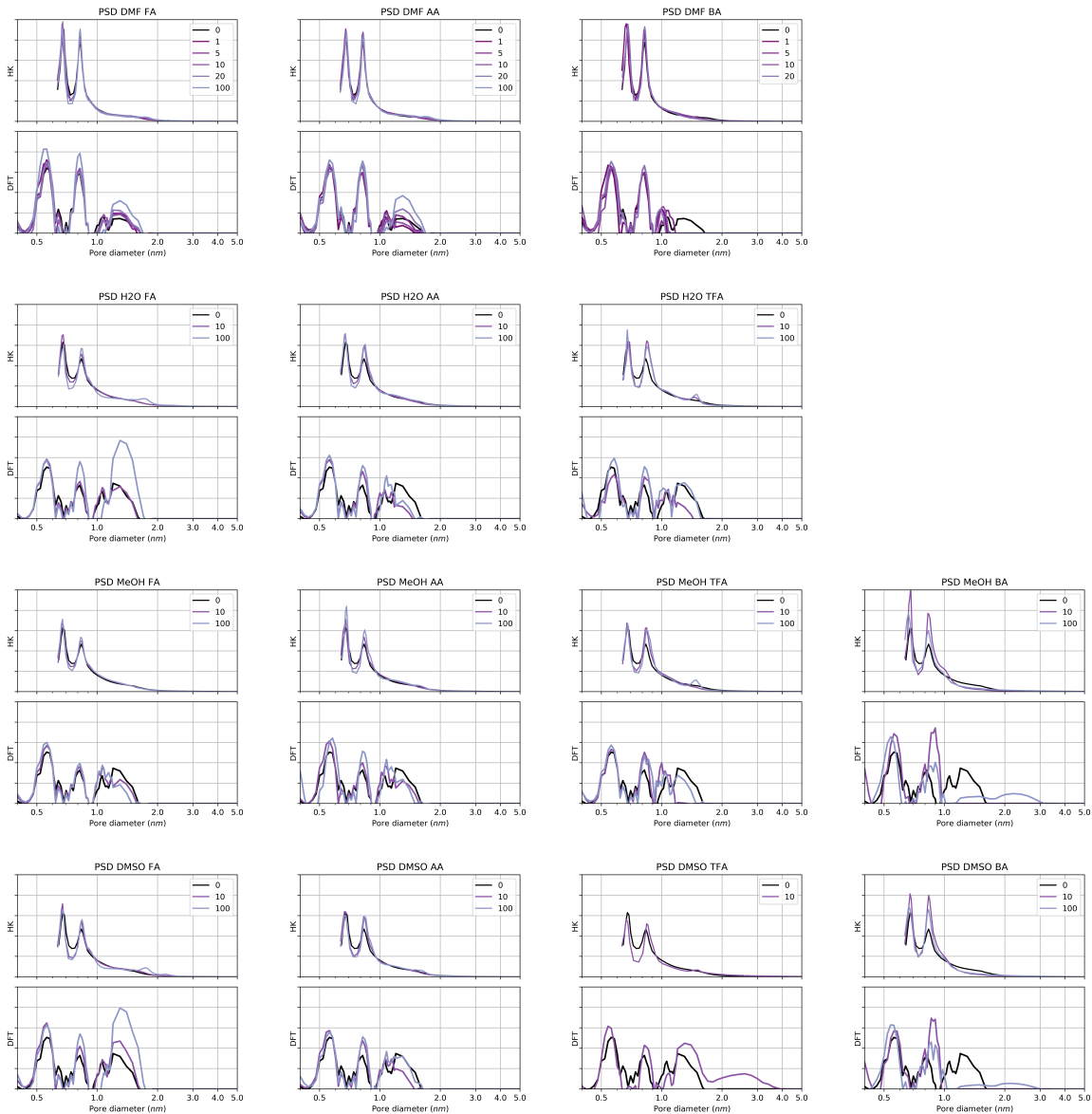


Figure D.9.: DMSO isotherm dataset activated at 200 °C

D.5. Characterisation

BIBLIOGRAPHY



Bibliography

- [1] William E. Acree. IUPAC-NIST Solubility Data Series. 99. Solubility of Benzoic Acid and Substituted Benzoic Acids in Both Neat Organic Solvents and Organic Solvent Mixtures. *Journal of Physical and Chemical Reference Data*, 42(3):033103, September 2013. ISSN 0047-2689, 1529-7845. doi: 10.1063/1.4816161.